Defense Nuclear Agency
Alexandria, VA 22310-3398

DNA-TR-91-86

Microstack Insulator for Flashover Inhibition Phase II

Juan M. Elizondo, PhD
William M. Moeny
Tetra Corporation
3701Hawkins Street, NE
Albuquerque, NM 87109

October 1992

Technical Report

CONTRACT No. DNA 001-89-C-0025

Approved for public release;
distribution is unlimited.

Destroy this report when it is no longer needed. Do not return to sender.

PLEASE NOTIFY THE DEFENSE NUCLEAR AGENCY, ATTN: CSTI, 6801 TELEGRAPH ROAD, ALEXANDRIA, VA 22310-3398, IF YOUR ADDRESS IS INCORRECT, IF YOU WISH IT DELETED FROM THE DISTRIBUTION LIST, OR IF THE ADDRESSEE IS NO LONGER EMPLOYED BY YOUR ORGANIZATION.

DISTRIBUTION LIST UPDATE

This mailer is provided to enable DNA to maintain current distribution lists for reports. (We would appreciate your providing the requested information.)

- ☐ Add the individual listed to your distribution list.
- ☐ Delete the cited organization/individual.
- ☐ Change of address.

NOTE:
Please return the mailing label from the document so that any additions, changes, corrections or deletions can be made easily.

NAME: ____________________

ORGANIZATION: ____________________

OLD ADDRESS	CURRENT ADDRESS

TELEPHONE NUMBER: (   ) ____________________

DNA PUBLICATION NUMBER/TITLE	CHANGES/DELETIONS/ADDITIONS, etc.) *(Attach Sheet if more Space is Required)*

DNA OR OTHER GOVERNMENT CONTRACT NUMBER: ____________________

CERTIFICATION OF NEED-TO-KNOW BY GOVERNMENT SPONSOR (if other than DNA):

SPONSORING ORGANIZATION: ____________________

CONTRACTING OFFICER OR REPRESENTATIVE: ____________________

SIGNATURE: ____________________

CUT HERE AND RETURN

DEFENSE NUCLEAR AGENCY
ATTN: TITL
6801 TELEGRAPH ROAD
ALEXANDRIA, VA 22310-3398

DEFENSE NUCLEAR AGENCY
ATTN: TITL
6801 TELEGRAPH ROAD
ALEXANDRIA, VA 22310-3398

REPORT DOCUMENTATION PAGE

Form Approved OMB No. 0704-0188

1. AGENCY USE ONLY (Leave blank)	2. REPORT DATE	3. REPORT TYPE AND DATES COVERED
	921001	Technical 890327 – 910331

4. TITLE AND SUBTITLE
Microstack Insulator for Flashover Inhibition
Phase II

5. FUNDING NUMBERS
C -DNA 001-89-C-0025
PE -62715H
PR -RL
TA -RW
WU-DH056840

6. AUTHOR(S)
Juan M. Elizondo, PhD and William M. Moeny

7. PERFORMING ORGANIZATION NAME(S) AND ADDRESS(ES)
Tetra Corporation
3701 Hawkins Street, NE
Albuquerque, NM 87109

8. PERFORMING ORGANIZATION REPORT NUMBER
TR-91-006

9. SPONSORING/MONITORING AGENCY NAME(S) AND ADDRESS(ES)
Defense Nuclear Agency
6801 Telegraph Road
Alexandria, VA 22310-3398
RAEV/Olinger

10. SPONSORING/MONITORING AGENCY REPORT NUMBER
DNA-TR-91-86

11. SUPPLEMENTARY NOTES
This work was sponsored by the Defense Nuclear Agency under RDT&E RMC Code B4662D RL RW 10602 PRAS 1940A 25904D.

12a. DISTRIBUTION/AVAILABILITY STATEMENT
Approved for public release; distribution is unlimited.

12b. DISTRIBUTION CODE

13. ABSTRACT *(Maximum 200 words)*

The program achieved results that represent a breakthrough in vacuum surface flashover insulation. The samples designed as the optimum configuration failed through the dielectric bulk before surface flashover was observed. In fact the ultimate limitation is the vacuum breakdown of the anode-cathode electrode system. As shown later we determine that for 100-nsec-long pulses the vacuum breakdown voltage of the electrode system was above 350 kV/cm, with some pulses as high as 450 kV/cm. Typical microstacks will sustain voltages above 280 kV/cm, with optimized samples failing typically at average fields above 400 kV/cm and not because of surface flashover but through the bulk of the sample. These numbers are excellent considering that the fitted data corresponds to 1 failure out of 15 pulses.

The scaling equation from J. C. Martin is used for a 50% probability of failure. The scaling equation produced by the microstack insulator comes from better than 10% (6.6%) probability of failure, or 94% reliability at the calculated voltage.

14. SUBJECT TERMS
Insulator, Vacuum, Flashover, Surface, Breakdown

15. NUMBER OF PAGES
148

16. PRICE CODE

17. SECURITY CLASSIFICATION OF REPORT	18. SECURITY CLASSIFICATION OF THIS PAGE	19. SECURITY CLASSIFICATION OF ABSTRACT	20. LIMITATION OF ABSTRACT
UNCLASSIFIED	UNCLASSIFIED	UNCLASSIFIED	SAR

NSN 7540-280-5500

Standard Form 298 (Rev.2-89)
Prescribed by ANSI Std. 239-18
298-102

CLASSIFIED BY:

N/A since Unclassified.

DECLASSIFY ON:

N/A since Unclassified.

CONVERSION TABLE

Conversion factors for U.S. customary to metric (SI) units of measurement

To Convert From	To	Multiply
angstrom	meters (m)	1.000 000 X E–10
atmosphere (normal)	kilo pascal (kPa)	1.013 25 X E+2
bar	kilo pascal (kPa)	1.000 000 X E+2
barn	meter^2 (m^2)	1.000 000 X E–28
British Thermal unit (thermochemical)	joule (J)	1.054 350 X E+3
calorie (thermochemical)	joule (J)	4.184 000
cal (thermochemical)/cm^2	mega joule/m^2(MJ/m^2)	4.184 000 X E–2
curie	giga becquerel (GBq)*	3.700 000 X E+1
degree (angle)	radian (rad)	1.745 329 X E–2
degree Fahrenheit	degree kelvin (K)	$t_K = (t^\circ f + 459.67)/1.8$
electron volt	joule (J)	1.602 19 X E–19
erg	joule (J)	1.000 000 X E–7
erg/second	watt (W)	1.000 000 X E–7
foot	meter (m)	3.048 000 X E–1
foot–pound–force	joule (J)	1.355 818
gallon (U.S. liquid)	meter^3 (m^3)	3.785 412 X E–3
inch	meter (m)	2.540 000 X E–2
jerk	joule (J)	1.000 000 X E+9
joule/kilogram (J/Kg) (radiation dose absorbed)	Gray (Gy)	1.000 000
kilotons	terajoules	4.183
kip (1000 lbf)	newton (N)	4.448 222 X E+3
kip/inch^2 (ksi)	kilo pascal (kPa)	6.894 757 X E+3
ktap	newton–second/m^2 (N–s/m^2)	1.000 000 X E+2
micron	meter (m)	1.000 000 X E–6
mil	meter (m)	2.540 000 X E–5
mile (international)	meter (m)	1.609 344 X E+3
ounce	kilogram (kg)	2.834 952 X E–2
pound–force (lbf avoirdupois)	newton (N)	4.448 222
pound–force inch	newton–meter (N·m)	1.129 848 X E–1
pound–force/inch	newton/meter (N/m)	1.751 268 X E+2
pound–force/foot^2	kilo pascal (kPa)	4.788 026 X E–2
pound–force/inch^2 (psi)	kilo pascal (kPa)	6.894 757
pound–mass (lbm avoirdupois)	kilogram (kg)	4.535 924 X E–1
pound–mass–foot^2 (moment of inertia)	kilogram–meter^2 (kg·m^2)	4.214 011 X E–2
pound–mass/foot^3	kilogram/meter^3 (kg/m^3)	1.601 846 X E+1
rad (radiation dose absorbed)	Gray (Gy)**	1.000 000 X E–2
roentgen	coulomb/kilogram (C/kg)	2.579 760 X E–4
shake	second (s)	1.000 000 X E–8
slug	kilogram (kg)	1.459 390 X E+1
torr (mm Hg, 0°C)	kilo pascal (kPa)	1.333 22 X E–1

*The becquerel (Bq) is the SI unit of radioactivity; Bp = 1 event/s.

**The Gray (Gy) is the SI unit of absorbed radiation.

TABLE OF CONTENTS

LIST OF ILLUSTRATIONS

LIST OF ILLUSTRATIONS (Continued)

LIST OF ILLUSTRATIONS (Continued)

LIST OF ILLUSTRATIONS (Continued)

LIST OF ILLUSTRATIONS (Continued)

LIST OF TABLES

SECTION 1
INTRODUCTION

Vacuum has been an attractive choice as insulation for high voltages due to the absence of free charge carriers. However, once a solid insulator is introduced to support the high voltage conductors the insulation ability is decreased compared to that of pure vacuum. Improvement of the insulation strength of insulators is required to increase the capabilities of pulsed power systems. It is also essential to keep the insulator dimensions small in order to minimize the system inductance (and the weight that must be carried into space.) Pulsed voltages over 1 megavolt (MV) are expected in many operations.

Electrically stressed insulators in vacuum often fail due to dielectric breakdown in the form of surface flashover which usually occurs at a lower field than bulk breakdown. Surface flashover also appears to be a time independent phenomenon in the range from dc to microsecond (μsec) pulse widths. From microsecond to nanosecond (nsec) pulse widths, the mechanism and surface damage change (Ref. 1). The microsecond pulse width regime appears to straddle both regimes.

For slower (dc to microsecond) pulses, insulator flashover in vacuum is considered by some authors, including Tetra's team to occur in the expanding cloud of gas desorbed from insulator surfaces (Ref. 2) when the applied potential is much less than the flashover voltage. The mechanism for desorption of these atoms and molecules is not fully understood (Ref. 3).

In the fast pulse regime (20 to 50 nsec) triple point enhancements and insulator relaxation time will play the dominant role in producing and controlling flashover voltages. To bring the value of the vacuum surface flashover electric field to levels comparable to the dielectric bulk strength of the insulator will be a major breakthrough in insulation technology. The achievement of this milestone is based on the understanding of the physics responsible for surface flashover. The physical mechanisms include (triple point enhancement, surface charging, ultraviolet initiated electron avalanche, insulator surface defects, etc.). Tetra's microstack approach resolves two of the basic physical mechanisms responsible for surface flashover. These are: surface charging and suppression of electron avalanching at intermediate points of the insulator.

The program plan for the microstack insulator consisted of a combination of theoretical analysis, to determine the physics involved in the microstack insulator's excellent performance in surface flashover, and an experimental testing program focused on providing empirical data. The experimental program provided the basis for understanding the microstack insulator behavior as a function of pulse voltage, insulator material characteristics and microstack dielectric wafer thicknesses and composition.

The theoretical analysis led to a good understanding of the physics involved in surface flashover, especially in those aspects that relate to the microstack technology. The program was initiated with a thorough analysis of the literature to identify the pre–existing established theories and hypothesis. From there the analysis looked at some of the issues related to the microstack technology, such as the formation of concentrated "pockets" of charge that eventually result in surface flashover. For single polarity pulses, the emission of secondary electrons and their hopping at the surface, provided a criterion for the initial design of the microstack dielectric wafer thickness. For bipolar stresses the oscillating displacement of ions and electrons forced by the field, is used to design the separation distance between metallic interlayers. An additional design criterion is given by the dimensions of the electrode or the electron emitting surfaces.

The experimental program provided the empirical data base, against which the analysis is compared. Measurements of pre–breakdown current and charge distribution before flashover were obtained using the microstack as a research tool. Low voltage measurements with different microstack insulator configurations are being performed to learn the characteristics of the electron cloud propagation properties. For the high voltage testing we fabricated the 1 Megavolt Marx pulser with the property of fast rise time (30–50 nsec) and controllable pulse width (100 to 3000 nsec). A technique was developed to produce samples in a very economical way so that an expanded test matrix produced more data. At the same time we developed a very sophisticated technique to fabricate samples with a very well controlled thickness and shape.

The program achieved results that represent a breakthrough in vacuum surface flashover insulation. The samples designed as the optimum configuration failed through the dielectric before surface flashover was observed. In fact the ultimate limitation is the vacuum breakdown of the anode–cathode electrode system. As shown later we determined that for 100 nsec long pulses the vacuum breakdown voltage of the electrode system was above 350 kV/cm, with some pulses as high as 450 kV/cm. Typical microstacks will sustain voltages above 280 kV/cm, with optimized samples failing typically at average fields above 400 kV/cm and not because of surface flashover but through the bulk of the sample.

The technology was developed to the point that practical uses such as dielectric walled linacs and microwave waveguides and windows are feasible. Linacs with gradients of 30 to 40 MV/m, which is about 20 to 30 times the gradient presently achieved, are now possible. Microwave windows and microwave cavities that can handle at least twice the present power level can be designed. Once the technology is fully disclosed it will become the vacuum insulator of choice. Future development must concentrate in its application for accelerator and microwave related technologies. As shown in Table 1 the microstack technology allows the practical development of dielectric walled accelerators and an improved power handling for microwave windows.

Table 1. Vacuum surface flashover insulator technology.

VACUUM SURFACE FLASHOVER INSULATOR TECHNOLOGY

STANDARD APPROACH (45°)

- $Ft^{1/8} A^{1/10} = KTE$
- 0.2 to 5μsec.
- 50 to 300 kV/cm
  @ 50% failure
- Dielectric is damaged after a few failures

NON–STANDARD APPROACH

Surface Coatings (45°)

- Good improvement (20%)
- Deteriorates after first failure
- One failure allowed

Electrode Coatings (45°)

- Controls e– emission
- 100% improvement
- Deteriorates after first failure
- One failure allowed

μ–Stack

- Controls secondary e– emission
- Controls desorpted species
- Controls UV effects
- No damage after failure

Dielectric Walled Linear Accelerators

Microwave Windows

SECTION 2
THEORETICAL ANALYSIS

2.1 SURFACE CHARGE DISTRIBUTION.

The relationship between surface physics and the sample geometry was initially analyzed following the experiments by Anderson (1978) (Ref. 4). In his experiments Anderson placed a needle as an enhancement point at both electrodes, with a 45° sample placed in between. Figure 1, from Reference 4, shows the results obtained for the needle on both the cathode and the anode for a 45° negative angled sample. The plot shown in the figure indicates the surface flashover voltage follows an inverse cosine law. By analyzing the characteristic solid angle of an electron cloud hitting the sample surface we find that the surface charge follows exactly an inverse cosine law.

The surface charge follows: (see Appendix A, page A3)

$$\sigma = \frac{q}{A}$$

with:

σ – surface charge
q – total charge
A – surface area.

Assuming that the area where the surface charge deposits itself corresponds to the electron cloud solid angle:

$$A = \iint r^2 d\phi \sin\theta d\theta$$
$$A = 2\pi r^2 \cos\theta$$

it follows that

$$\sigma \propto \cos^{-1}\theta$$

In the case of negative angle samples the dielectric surface shows a bound surface charge which is positive in nature. All the electrons emitted before surface flashover are attracted to the insulator surface. It is this pre–existing positive charge characteristic of the surface that dominates to make the $\cos^{-1}\theta$ behavior possible. Positive angle samples initially follow the $\cos^{-1}\theta$ function but in general the distribution looks more like a parabolic function. The data is more statistically dispersed, a fact that can be tied to the negative bound surface charge prior to the initial electron ejection. Figure 2 illustrates the conditions at the dielectric surface when the field is applied. The behavior is explained by two different mechanisms or a combination of both. First there is the anode initiated flashover in which it is assumed that ions are accelerated towards the cathode bombarding the dielectric surface and initiating the avalanche process that leads to failure. The second process still is electron initiated but now only electrons with the "right" energy will hit the surface, and once they do they generate secondaries which are deflected toward the anode with little or no hopping given the negative nature of the bound charge (Ref. 5).

All these patterns in the behavior of surface flashover with polarity and geometry are broken up by the microstack insulator. By assuming the same initiating behavior, the prediction of the theory is that a drastic reduction of net surface charge deposited in the dielectric surface will in turn enhance the maximum voltage prior to surface flashover.

Calculations done to analyze the surface charge deposited on the surface indicate that an inverse cosine law is followed. By following the Figure 3 geometry the plot in Figure 4 follows the inverse cosine law but in this case the vertical axis is surface charge on the dielectric and the horizontal axis is electron cloud solid angle. The electron cloud shell and the sample geometry interact in a 3 dimensional fashion. Preliminary results from this simple geometric interaction shows the correct behavior. It shows that if the integration is carried to the total height of the sample the surface receives the total charge or maximum charge possible. As the metal layers are introduced the electron cloud is now partitioned and so is the dielectric surface by the metal wafers. As can be observed in Figure 3, the introduction of metal layers changes the place where the electrons hit the sample. Since most of the electrons now hit the metal, instead of the dielectric, secondary emission is totally suppressed. The effect can be observed by comparing the total surface charge deposited in the dielectric, by integrating θ from 0 to 90°, shown in Figure 4a. Figure 4b is the equivalent charge deposited in the dielectric when microstack is used; this is integrating θ from 0 to about 20°, which corresponds to having the metal shields protruding the same distance as the dielectric thickness, and the electron ejection point being 3 times the dielectric thickness. The microstack insulator under a cloud of electrons following the same distribution as before, shields the surface charge on the dielectric surface by as much as 80%.

We assume that in each stack all the dielectrics (insulators) are of equal thickness and all the stainless steel (S.S.) strips are of equal thickness to each other. For the analysis we refer to Figure 3. As diagrammatically illustrated, the stack is in the Y–Z plane. The thickness of each dielectric layer, heretofore symbolized as ϵ, is identified by t. The bottom layer is tagged t_1 and subsequent layers are labelled t_2, t_3, etc. The SS strips, which are identified in the figure by the symbol d are of different thickness from the dielectric. For clarity, the SS strips are labeled d_1, d_2, d_3, etc. Thus the first strip, d_1 lies immediately above t_1 (or t).

Problem: Our analysis seeks to determine; the effect of moving the electron emission point away from the dielectric surface, at distances comparable to the metal protrusion length ℓ

1. The variation of the surface area S with Θ. For the definition and derivation of S see Appendix A.

$$S = \frac{\pi}{2} r^2 \cos \Theta \qquad \text{(Eq 1)}$$

2. The behavior of the total charge on S, Q_T on Θ where for simplicity we have neglected the thickness d of the metal, this is possible because we are interested in the charge deposited in the dielectric. The following treatment differs from the one in Appendix A, only that now we allow the origin to be at a variable distance (y) from the dielectric surface, and carried the analysis for a single dielectric stack. As more stacks are present, the shielding is found to greatly affect the charge deposited in the subsequent dielectric layers.

$$Q_T = \epsilon_0 E_0 \left[1 - (K-1)\frac{y}{[t^2+y^2]^{\frac{1}{2}}}\right] \frac{\pi}{2}\, y\, (t^2 + y^2)^{\frac{1}{2}} \qquad \text{(Eq 2)}$$

Again see Appendix A for derivation of Q_T.

3. The behavior of the capacitance C with Θ; see Appendix A for derivation of

$$C = \frac{Q_T}{V} = \frac{\epsilon_0 E_0}{V} \left[1-(K-1)\frac{y}{[t^2+y^2]^5}\right] \left[\frac{\pi}{2} y(t^2+y^2)\right] \quad \text{(Eq 3)}$$

Analysis: From Appendix A, we have shown that

$$S = \frac{\pi}{2} r^2 \cos \Theta.$$

From the microstack sketch in the Appendix A, we have

$$r^2 = (t^2+y^2) \text{ and } \cos \Theta = \frac{y}{[t^2+y^2]^{\frac{1}{2}}}$$

$$\Rightarrow S = \frac{\pi}{2} r^2 \mathrm{Cos}\ \Theta = \frac{\pi}{2}[t^2+y^2]\left[\frac{y}{(t^2+y^2)^{\frac{1}{2}}}\right] = \frac{\pi}{2} y[t^2+y^2]^{\frac{1}{2}} \quad \text{(Eq 4)}$$

$$\text{therefore } S = \frac{\pi}{2} y(t^2+y^2)^{\frac{1}{2}} \quad \text{(Eq 5)}$$

Also from the Appendix we have

$$Q_T = \sigma_T S = \epsilon_0 E_0 [1-(K-1)\cos\ \Theta]\ \frac{\pi}{2} t^2 \csc^2\Theta \cos\Theta$$

$$= \epsilon_0 E_0 [1-(K-1)\cos\Theta] \frac{\pi}{2} t^2 \frac{\csc\Theta}{\tan\Theta}$$

Therefore

$$Q_T = \epsilon_0 E_0 \left[1-(K-1)\frac{y}{(t^2+y^2)^{\frac{1}{2}}}\right] \frac{\pi}{2} y[t^2+y^2]^{\frac{1}{2}}$$

or

$$Q_T = \frac{\pi}{2} \epsilon_0 E_0 \left[1-(K-1)\frac{y}{(t^2+y^2)^{\frac{1}{2}}}\right] y[t^2+y^2]^{\frac{1}{2}} \quad \text{(Eq 6)}$$

Again for the capacitance of the stack C we have

$$C = \frac{Q_T}{V} = \frac{\epsilon_0 E_0}{1} \frac{\pi}{2V} \left[1-(K-1)\frac{y}{(t^2+y^2)^{\frac{1}{2}}}\right] y[t^2+y^2]^{\frac{1}{2}}$$

$$\Rightarrow \quad C = \frac{\pi \epsilon_0 E_0}{2V} \left[1-(K-1)\frac{y}{(t^2+y^2)^{\frac{1}{2}}}\right] y[t^2+y^2]^{\frac{1}{2}} \qquad \text{(Eq 7)}$$

At this point we note that after the single dielectric layer t in Equations 5, 6 and 7 changes to $h = t' = t_1+d_1$, that is, the sum of the subsequent dielectric thickness t_1 and the S.S. strip d_1. Thus with the known values of t' the only variable we have that controls S, Q_T, and C in the above boxed expressions is y. This means that our graphical plots of S, Q_T and C are 2–d plots – one variable case.

For our first set of plots for S, Q_T and C we note that in the case of the first dielectric layer with t_1, the angle cosine, cos Θ, is found with $0<y\leq\ell = 0.040"$ [given]. In the second set of plots we incorporate the effect of stacking, that is, we increase $t = t_1$ to $t = t_1+d_1$. We also increase y such that $\ell<y$.

The graphical illustrations of the expressions for S and Q_T are shown in Figures 5, 6, 7, and 8. The illustration for C is essentially the same as that for Q_T, so C–graphs are not actually shown. Note that in all the figures, Figure 5 to Figure 8, the plots are in the Cartesian coordinate system with the independent variable y plotted along the horizontal and the observables, which in these cases are S and Q, plotted along the vertical. Figure 5 and Figure 6 refer to S = the interaction surface area. We notice the almost linear increase with increasing Y values (or x value in the graph). Figure 5 refers to the case when $y\leq\ell \equiv$ the distance of the S.S. stripe protruding from the stack. Figure 6 is the case for $y>\ell$.

In Figure 7 we have graphed the Q_T, total charge and we note the increase in magnitude with y increase. This Figure refers to $y \geq \ell$ case and Figure 8 refers to $y \leq \ell$ case. For all figures, the dielectric was taken as 0.003" in thickness.

2.2 MICROSTACK INSULATOR DESIGN.

The analysis shows the drop in the effective charge deposited at the dielectric surface. If one assumes that all charge hitting the metal surfaces is accumulated in the capacitor formed by the wafers, a criteria can be established by the conditions at the layer surface. We analyzed three different criteria based on the previous analysis allowing us to consider each section of the shielded insulator as independent from the previous one.

At this point three criteria have been used to design microstack samples

a) Electron hopping distance which defines maximum dielectric thickness and metal wafer separation.

b) Electrode dimensions and maximum electron emission point distance which defines dielectric recess from the metal wafer edge and effective shielding distance. It uses the streamer propagation characteristics at the dielectric surface.

c) Maximum ion displacement distance which relates to item a) but accounts for polarity changes and bipolar stresses.

The first criterion used to design a microstack insulator sample consisted of the electron hopping distance. Figure 9 shows a plot of electron hopping distance vs. electron ejection angle. This follows from a simple ballistic model and assumes that the field normal to the insulator surface can be as high as 10% of the nominal (external) field. As can be observed, distances for 5° to 45° ejection angles are in the millimeter and submillimeter range. The criteria used is that the metal wafer separation should be equal or smaller than the given hopping distance. The first criterion assumes no collisions in between electron hopping distances, and low ion or molecular desorption from the dielectric surface; it yields an upper limit value, and it is based on a simple ballistic model. Assuming a parabolic electron (Ref. 6) path so that the time required to reach the maximum height, h, is the same time to return to the dielectric surface (see appendix B).

$$\text{Electron Range} = \frac{4V_1\ E_0\ \cos\theta}{qE_n^{\,2}} \tag{8}$$

where W_1: Electrons initial impact energy
E_0: External electric field
E_n: Field normal to the semiconductor surface
q: Electron charge

As can be observed the range of interest determines an upper limit of about 500 μm for the thickness. This is the maximum expected electron range. Through these calculations an upper limit in thickness was set.

The second criterion follows from the dimensions of the electrode and looks for the maximum distance from where electrons may hit the dielectric surface. At this point it is estimated that only electrons ejected from distances equal or smaller than the electrode gap will have an opportunity to hit the dielectric surface; points at or close to the triple point are considered more critical.

The second criterion uses the surface flashover theory based on a high pressure layer of desorbed material facilitating the electron avalanche through the surface. The two main competing flashover models are described well by A. A. Avdienko and M. D. Malev (Ref. 7): thermal flashover vs discharge in desorbed gas layer. Thermal flashover is limited primarily to the thermal conductivity of the material. Gas desorbed by electron bombardment creates a high-pressure environment for a gas streamer type of breakdown. The latter hypothesis, first introduced by S. P. Bugaev *et. al.* (Ref. 8) is supported by the similarity between observed luminescent spot speeds (10^7–10^8 cm/s) and atmospheric streamers ($\approx 10^8$ cm/s) (Ref. 9). The observed velocity away from the surface, about 10^6 cm/s, taken as a measure of the gas motion, is slow enough to insure high densities. In essence the desorbed gas is inertially confined for the 10's of ns it takes for breakdown to occur. Assuming the gas is mostly H_2 (other likely constituents are N_2, CO_2 and H_2O), Avdienko and Malev get an electron mean free path of 300–500 μm at 1 torr (which scales to about 1 μm at 1 atm).

One of the controversies in the literature is which energy to use as the correct avalanche stability criterion. The secondary electron yield typically shows above 1 atm a low energy threshold W_1 (energy of primary electrons) of about 100 eV; it peaks, and then decays again with a second threshold W_2 at about 3000 eV.

Contrary to Avdienko and Malev, R. A. Anderson and J. P. Brainard (Ref. 10) use W_1, leading to a computational model which succeeds well in matching many observables. J. P. Brainard and D. Jensen (Ref. 11) describe that model in detail. It appears to explain the dependencies on angle, surface charging, and the insensitivity to ambient gas.

Direct measurements of surface charges by C. H. de Tourreil *et. al.* (Ref. 6) show 10 to 60 $\mu C/cm^2$ for 20 to 80 kV/cm on cylindrical insulators. The high end implies about $4 \times 10^{21}/cm^3$ electron and neutrals density, which is equivalent to over 100 atm. The electron mean free path would become truly microscopic. If we merely consider the distance required for a collisionless electron to gain an energy comparable to typical ionization potentials, we get a very pessimistic bound. Using 20 eV, a 100 kV/cm goal would require one stack layer per 2 μm, which may be beyond feasible manufacturing techniques.

An empirical argument for the high–pressure flashover model is given by E. W. Gray (Ref. 12). He observed a "clear" zone from cathode to first damaged area in surface flashover measuring 62 μm for 99 kV/cm. That implies the electrons had no more than about 600 eV before causing an avalanche, which supports Anderson and Brainard's use of W_1. If we require the micro–stack to interrupt electrons as they reach W_1, we get a criterion of about 100 V / 100 kV/cm = 10 μm; not great, but better than the first estimate of 2 μm. For an optimistic criterion, we could use the observed damage range of about 60 μm.

Our models (Ref. 13) in air and SF_6 indicate the fast streamer ($\approx 10^8$ cm/s) merely creates a medium–ionization path ($\approx 10^{14}$ e/cm^3), which then draws enough current for ohmic heating to bring it to a temperature >10,000 K where thermal ionization takes over nonlinearly, causing voltage collapse due to arcing.

The importance of this is that the correct scale size to interrupt the surface breakdown is driven by subtle considerations of what it takes to disrupt the precursor streamer, not the heating phase. Once a streamer has created a moderately conducting path, it will be very difficult to prevent breakdown (except by somehow shunting the voltage—e.g. with a very high external circuit inductance).

Only the streamer mechanism, based on E–field enhancement at the tip of the streamer leading to fast but localized electron avalanching, can explain the filamentary nature of flashover tracks. Perhaps that also holds the key to our quest. The streamer propagation requires enhanced fields of about 100 kV/cm/atm (scales as P) over a thickness of about 0.1 cm–atm (scales as p^{-1}). If we assume that the microstack acts as a capacitive voltage divider, then the voltage between layers is a constant on the time scale of streamer propagation. Thus, the above criterion for streamer propagation requires at least 10 kV/atm per stage. If we believe the 100 atm estimate above, the theoretical limit for the micro–stack technique is about 10 MV/cm, but it would require stacks every 1 μm. However, 100 μm stacks may hold off 100 kV/cm.

The third criterion includes ionic produced effects such as oscillations and surface bombardment. This is done mostly to account for changes in field polarity, microwave environments and bipolar stresses. Resonance frequency (in this example) is established at the plasma frequency for a single CO^{2+} ion/cc:

$$\omega_p = \frac{n_i q^2}{\epsilon_0 m_i} = 200 \text{ kHz}$$

where: n_i = 1 (ion concentration)
q_i = ionic charge
m_i = ion mass
$\epsilon_o = 8.85 \times 10^{-12}$ F/m.

It is very important to observe that under this criteria the microstack insulator can be designed for a specific pulse period and most importantly for a known residue gas in the system.

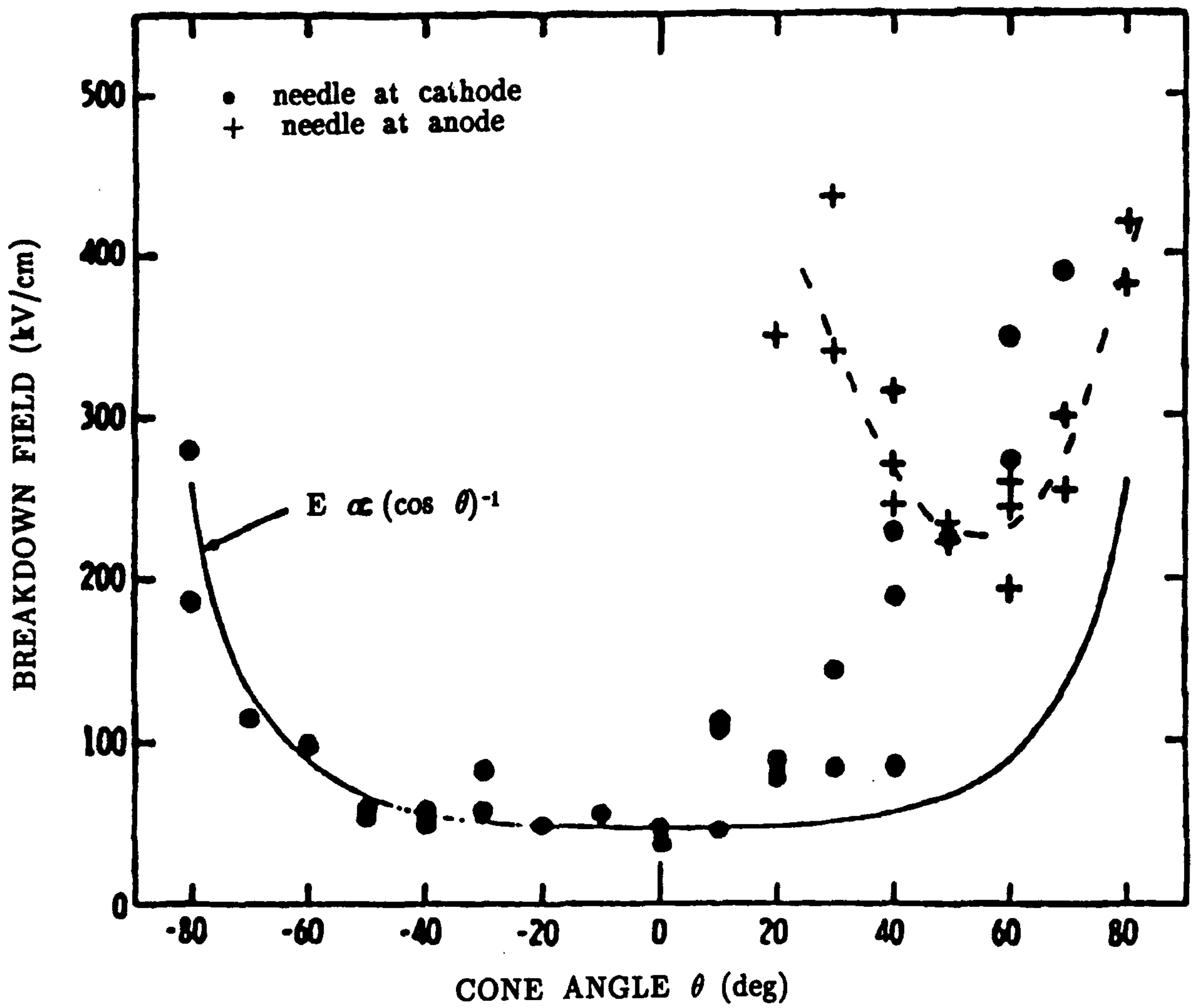

Figure 1. Angular dependence of breakdown field when a needle is attached to the cathode or anode electrode.

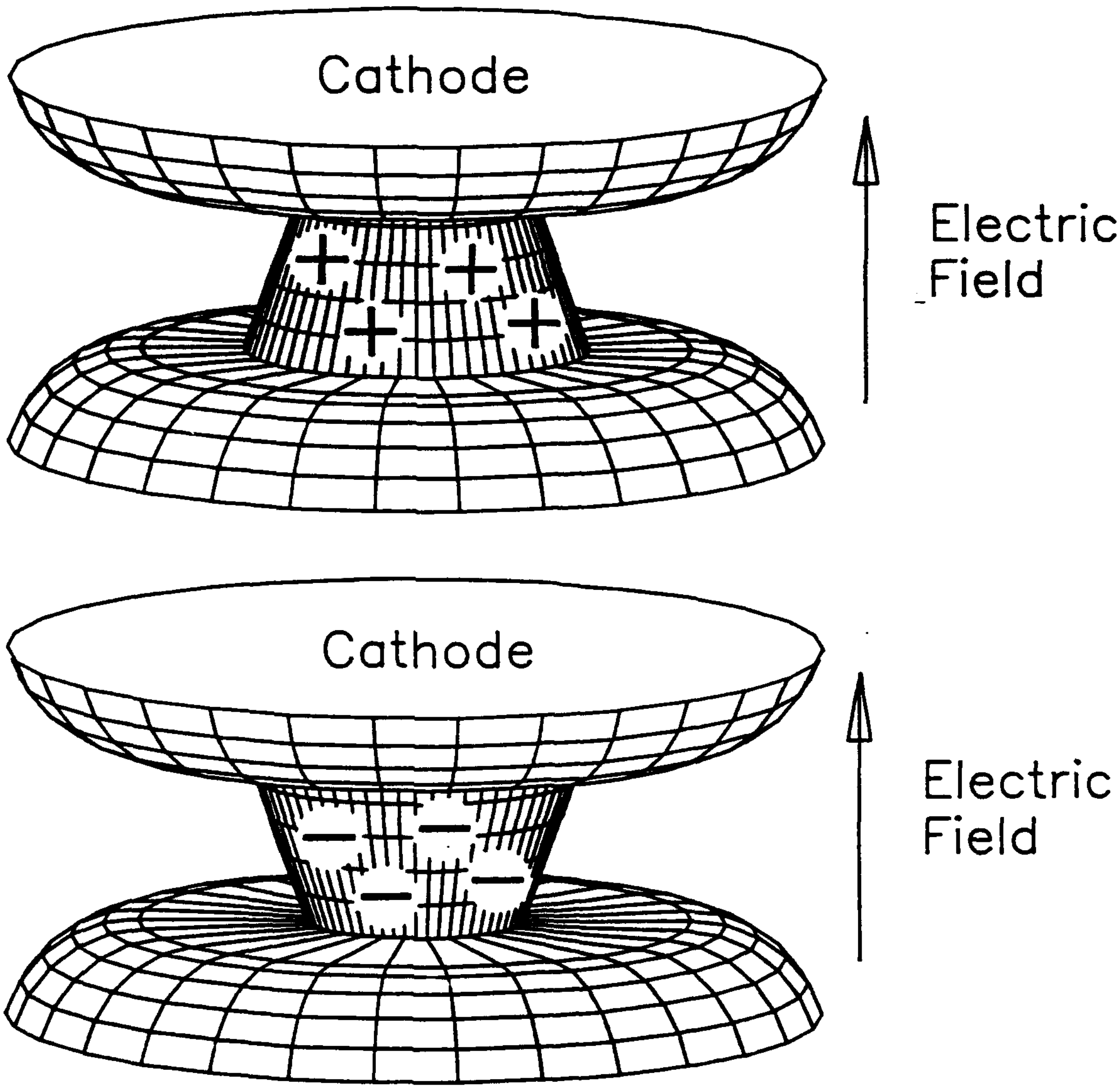

Figure 2. **Positive and negative bound charges in positive and negative angle samples.**

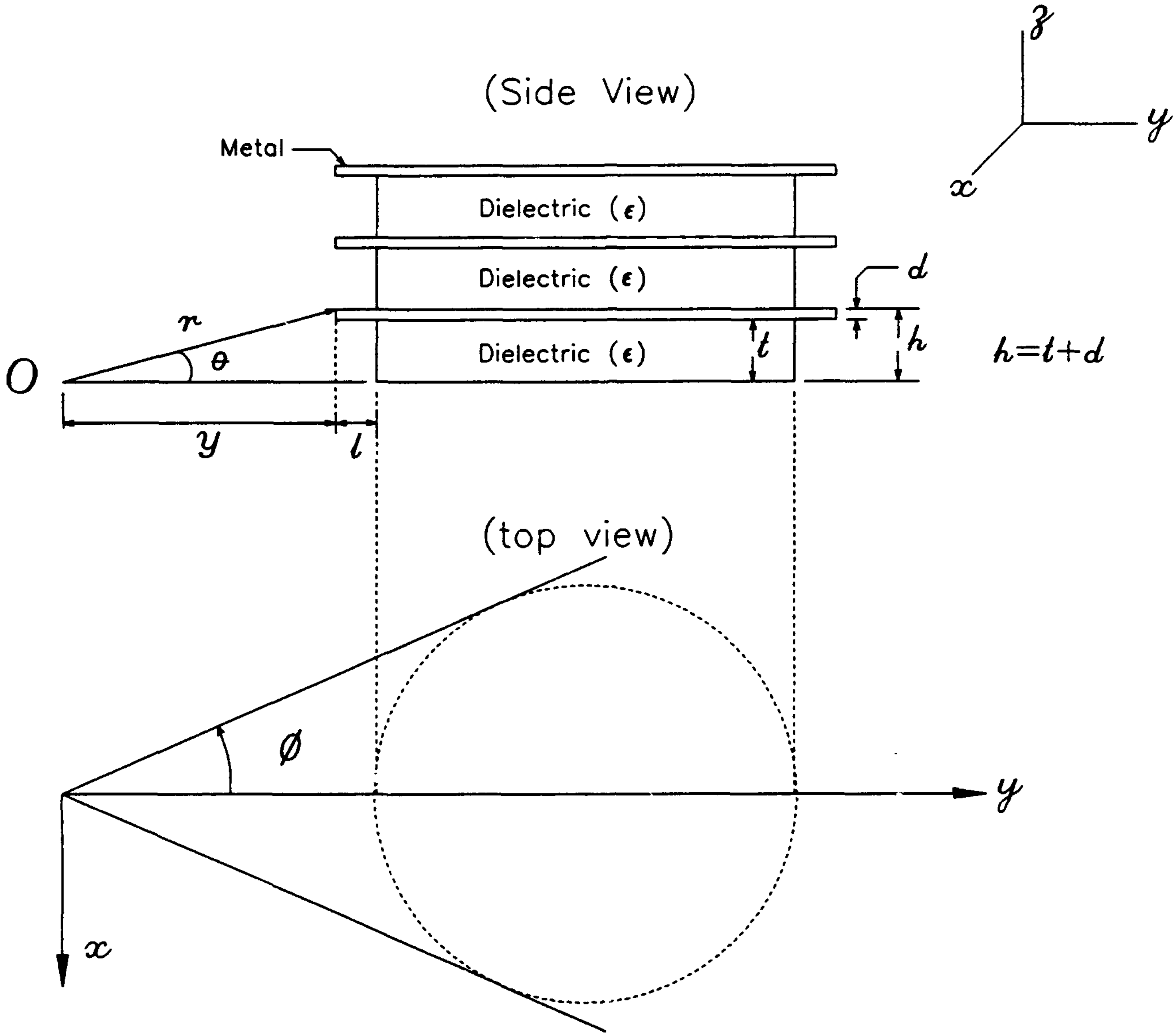

Approximate microstack surface area exposed to an electron cloud emitted from point O.

Figure 3. Microstack sample.

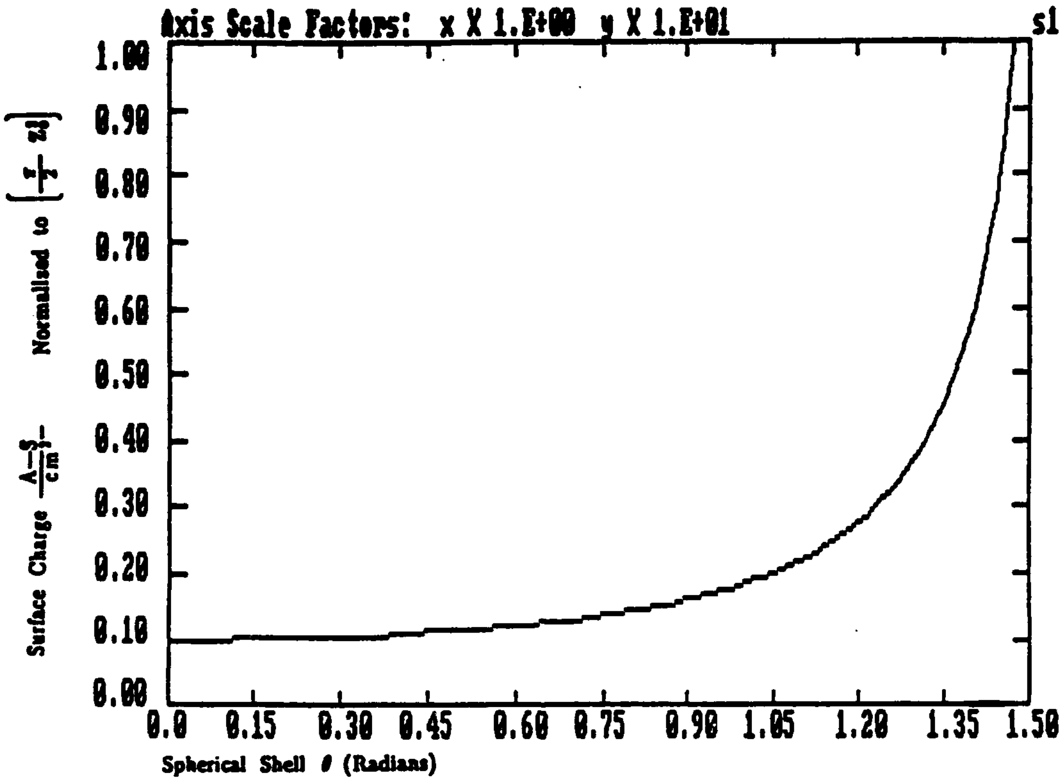

Figure 4a. Effective surface charge deposited on a cylindrical dielectric sample with the geometry as shown in Figure 2.

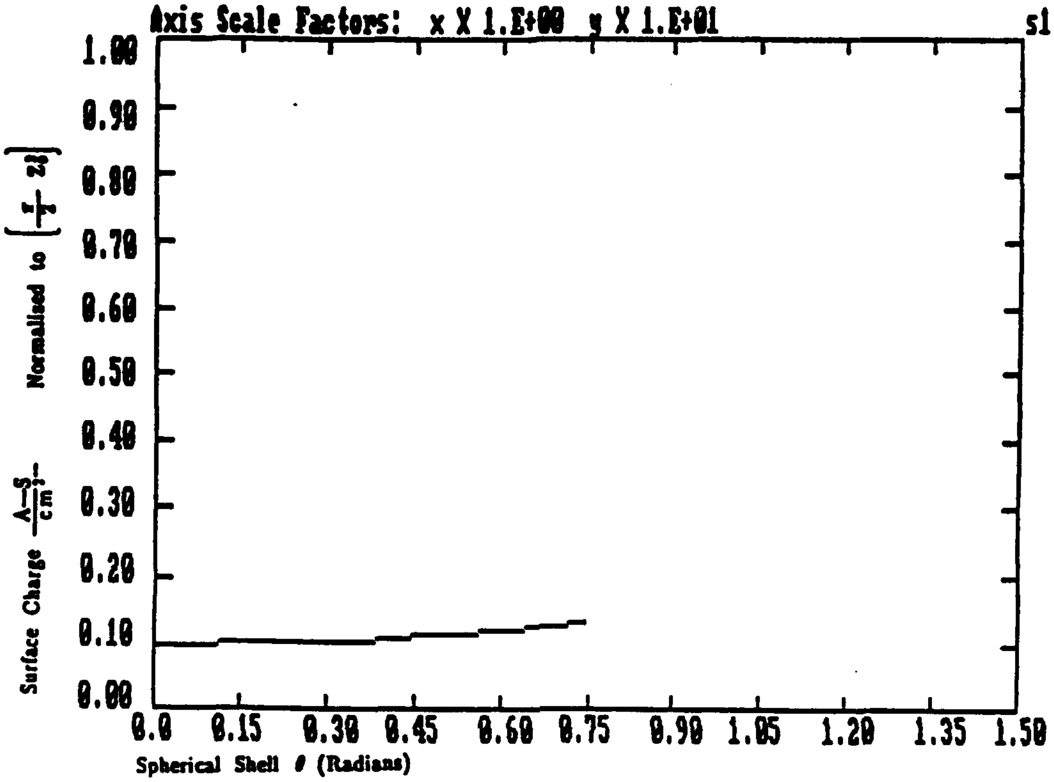

Figure 4b. Effective surface charge deposited on a cylindrical sample using the microstack. (Same positions as in Figure 2.) The cut–off is the effect of shielding by the metallic wafers.

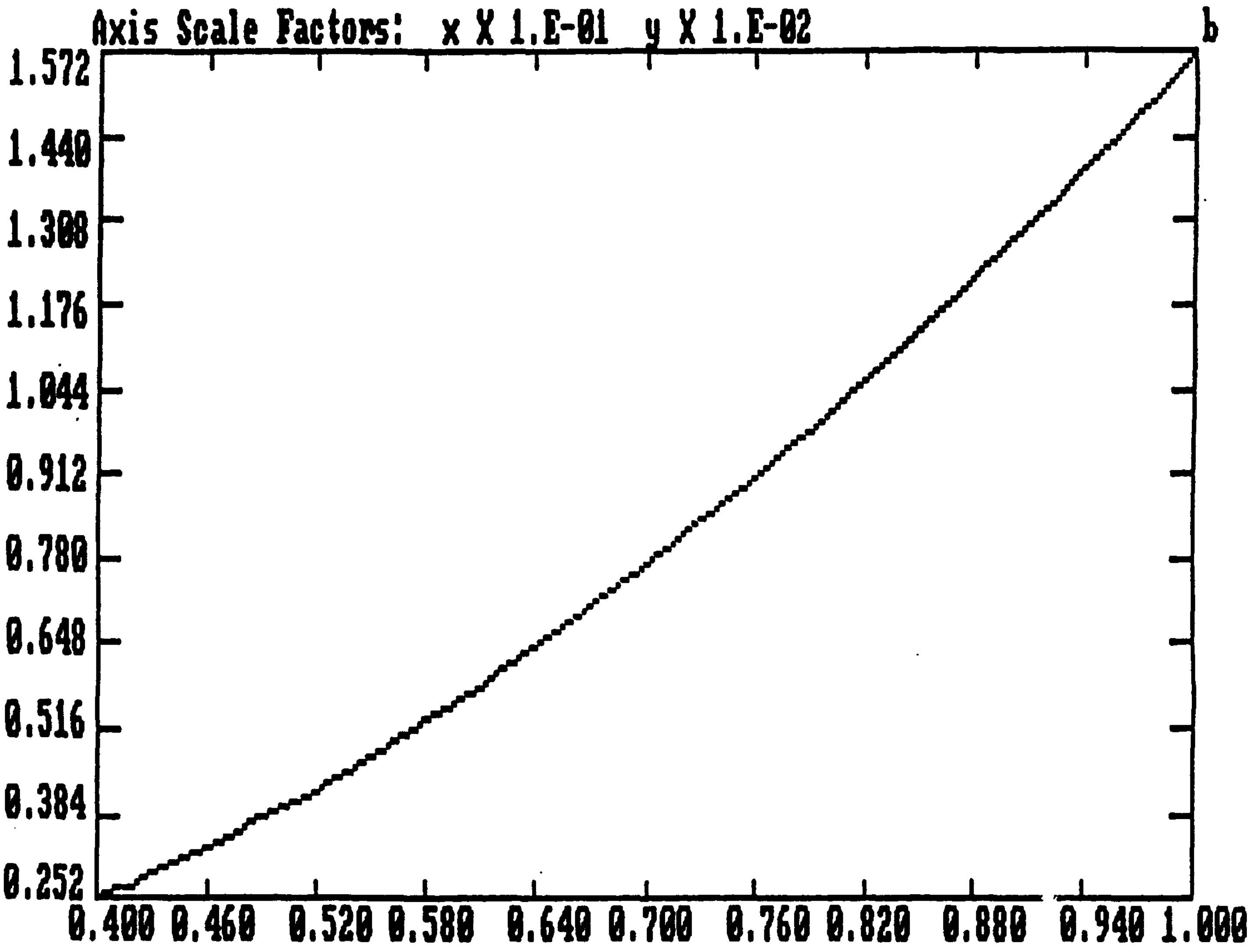

$$S = \frac{\pi}{2} r^2 \cos\theta = \frac{\pi}{2}\left[t^2+y^2\right]\left[\frac{y}{(t^2+y^2)^{\frac{1}{2}}}\right] = \frac{\pi}{2} y[t^2+y^2]^{\frac{1}{2}} \quad (4)$$

The figure refers to the case when $y \leq \ell$, where ℓ is the distance of the stainless steel (S.S.) strips protruding from the stack. Vertical axis corresponds to s ——— horizontal axis is (y).

Figure 5. Plot of the interaction surface area S with respect to the parameter y.

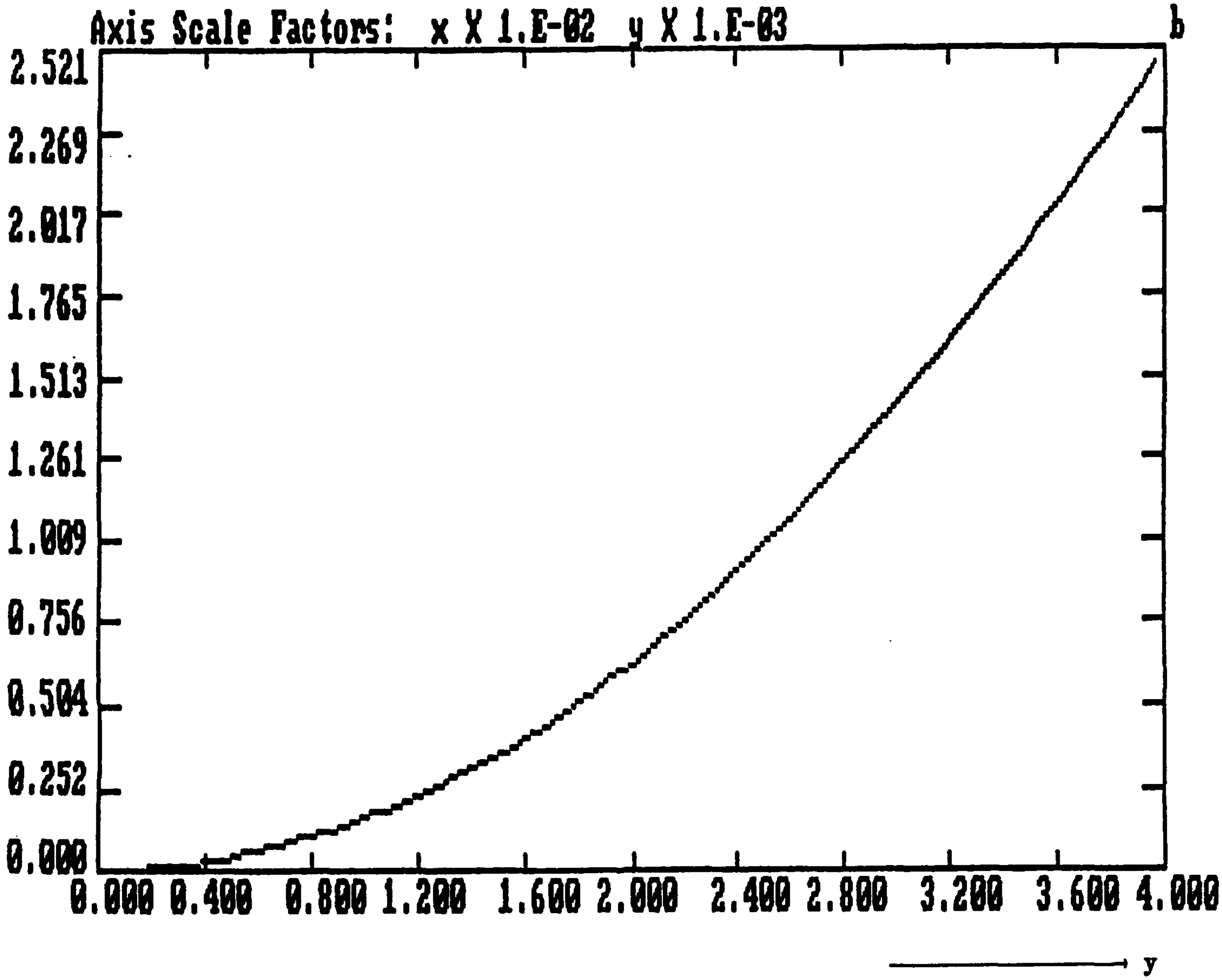

Figure 6. The plot of S as in Figure 5. But this plot differs for the plot of Figure 5 because it describes the case when $y>\ell$ The parameter ℓ is defined for the case of Figure 5.

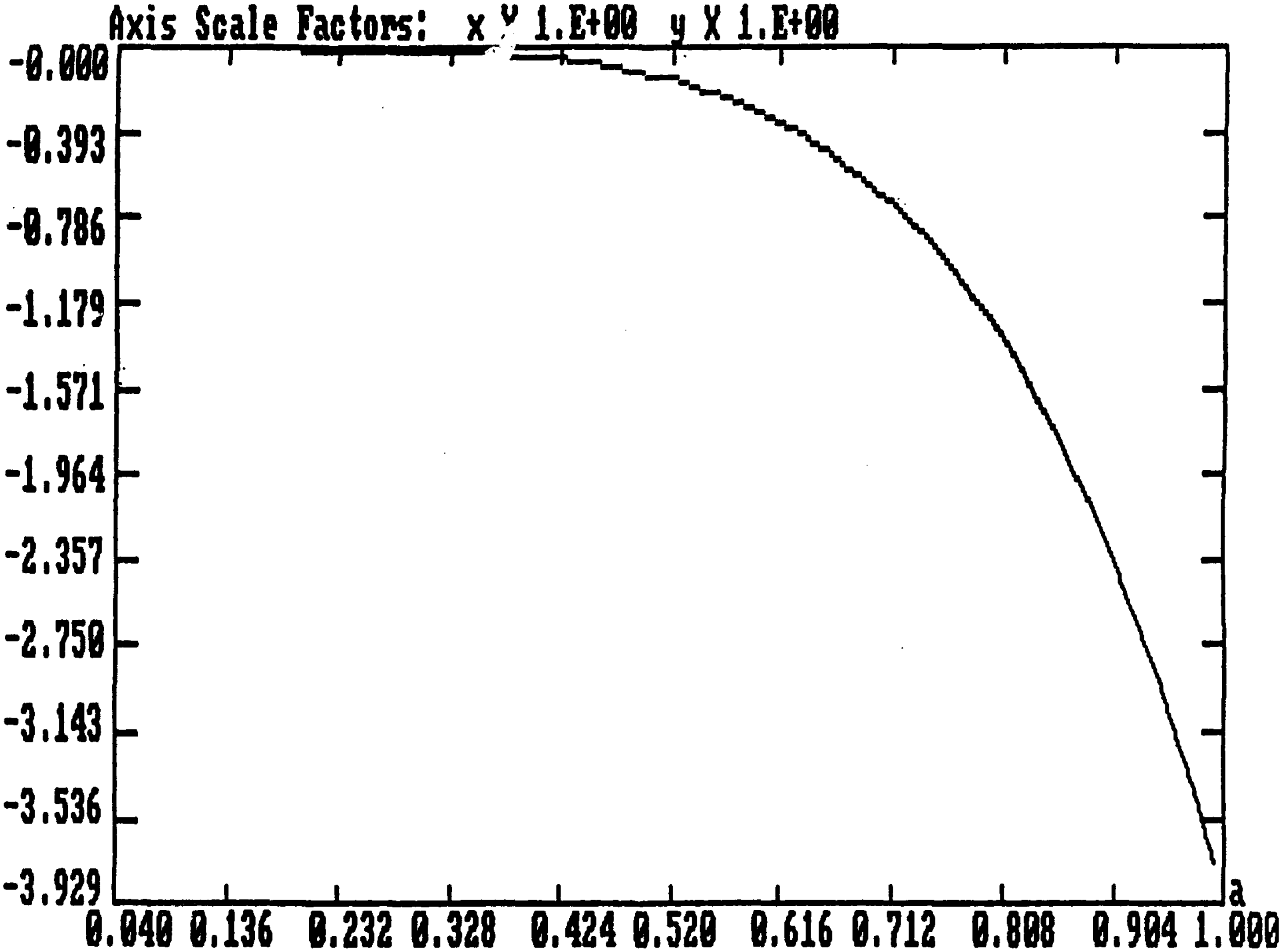

$$Q_T = \frac{\pi}{2}\,\epsilon_0 E_0\left[1-(K-1)\frac{y}{(t^2+y^2)^{\frac{1}{2}}}\right]y[t^2 + y^2]^{\frac{1}{2}}$$

Figure 7. Plot of Q_T versus y for $y>\ell$. Q_T is the total charge contained by the microstack.

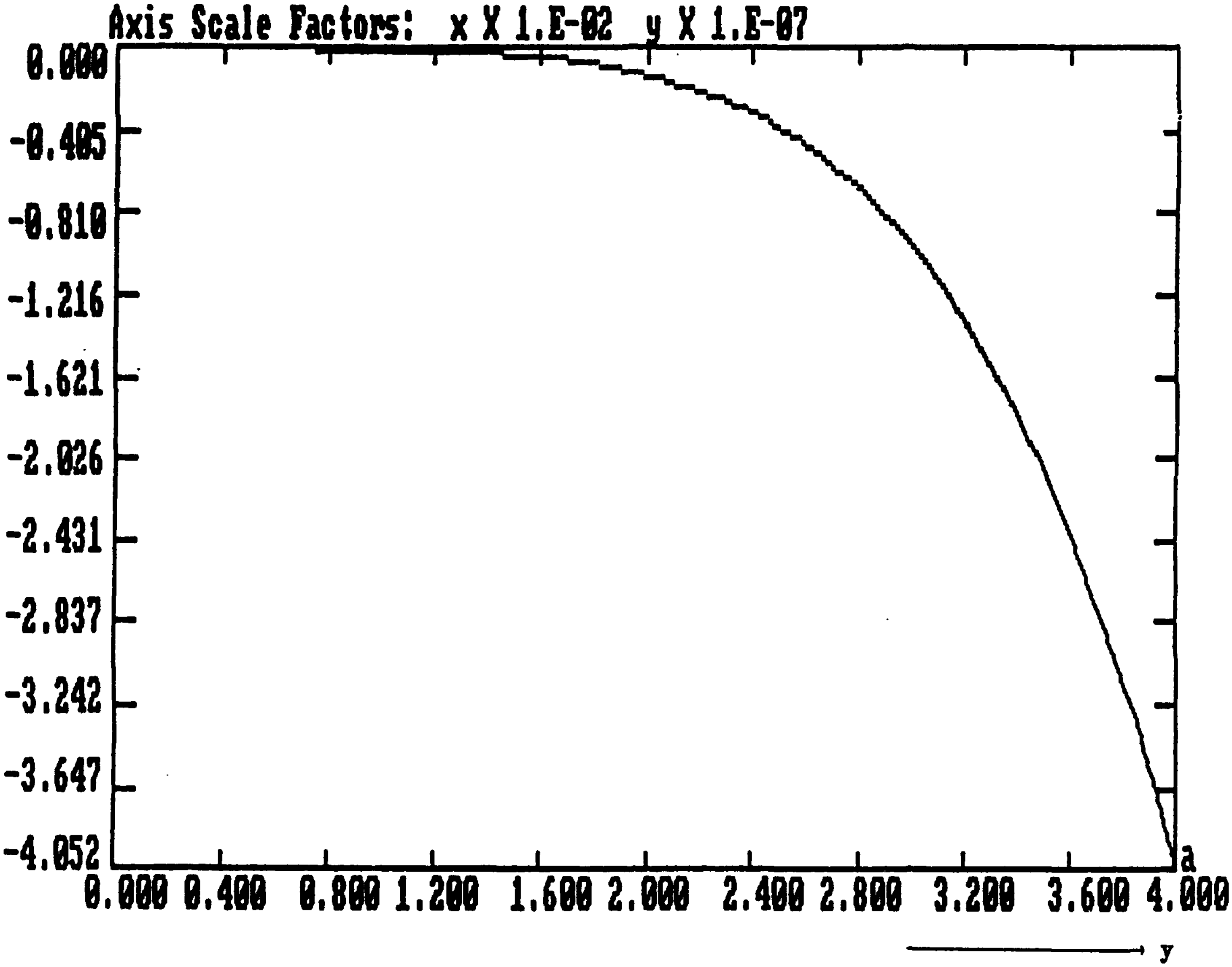

Figure 8. Plot of Q_T defined in Equation (6) above but now with $y \leq \ell$

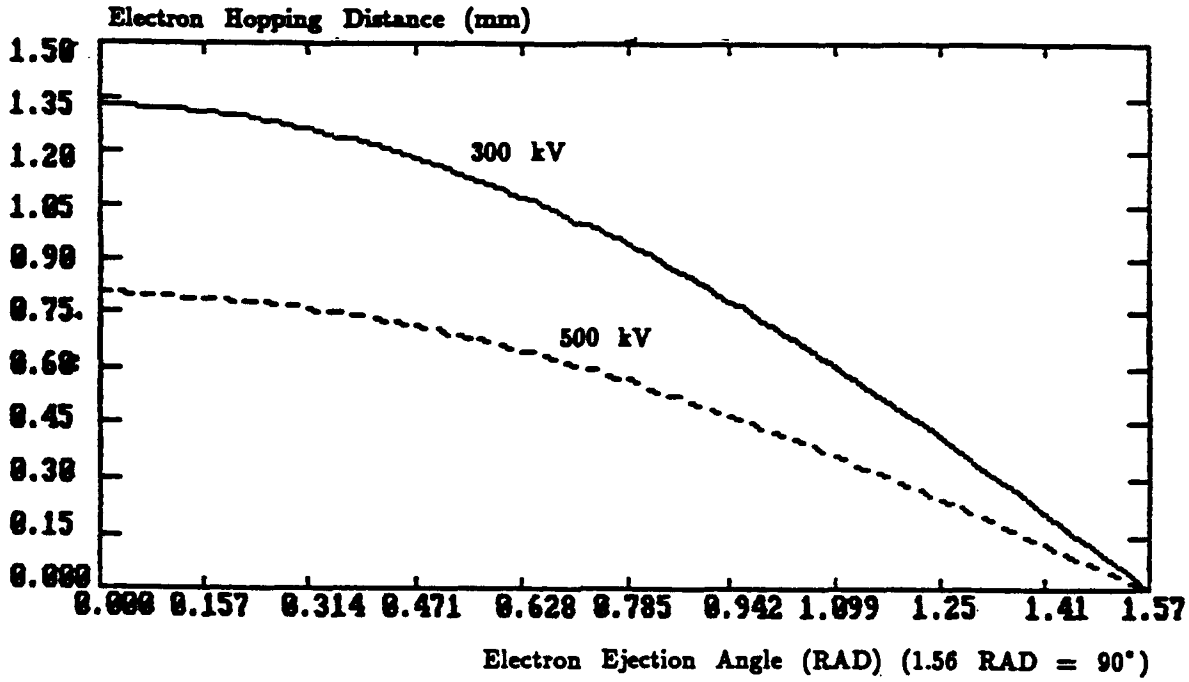

Figure 9. Electron hopping distance vs electron ejection angle, assuming W_o = 100 ev, E_n = 0.1 E_0 for two external field (E_o) values.

SECTION 3
EXPERIMENTAL SETUP

The experimental facility was built to accomplish two major program goals:

a) High voltage vacuum testing to develop the technology and accumulate data with a megavolt, variable length pulser.

b) Low voltage vacuum testing to carefully take measurements of the microstack surface charge properties.

The one megavolt Marx pulser was built using a design that provides a fast (20–30 nsec) risetime. The Marx layout as shown in Figure 10 consists of 22 capacitors and 11 switches. The unique features of this Marx (fast risetime; flat top) are accomplished by the capacitor arrangement and the gas switch construction.

The capacitors are distributed in a zig–zag configuration which reduces considerably the stray capacitance from capacitor pairs. At the same time current flows in opposite paths throughout the Marx thus reducing the effective stray inductance of the Marx. The gas switches are placed in two symmetrically placed pipes with the switch closure sequence as indicated in Figure 10 where it can be observed that once the first two switches close, UV radiation from the initial arc, "conditions" the rest of the switches. This UV conditioning reduces the switch closure jitter and so far has produced less than 1 % no–trigger situations.

The switches are loaded with dry air and the operating pressure is from 10 to 100 psig. The first three switches are triggered with a 40+ kV fast risetime pulse, provided by a voltage inverter pulser. The Marx triggers are controlled through a PT–55 (Pacific–Atlantic pulse generator) and they are timed through a Maxwell 1605 delay generator. The Marx characteristics are shown in Table 2.

The delay generators are required to activate the (trigatron) crow–bar that controls the pulse length. The crow–bar is an SF_6 externally controlled trigatron. It is operated with two gap settings, up to 500 kV and up to 1000 kv. Figure 11 shows a series of traces showing different pulse lengths.

The Marx generator is capable of producing pulses from 100 nsec long to 3 μsec long. Most testing was done at 100 nsec long pulses with the last series of samples tested at about 50 to 80 nsec long pulses. The system in this configuration will trigger at charging voltages as low at 7.5 kV. For the program it was subjected to an excess of 2000 pulses before refurbishing of the switch electrodes was necessary.

The integrated system is shown in Figure 12 where the vacuum system is placed on top of the Marx output. Figure 13 shows the physical layout where the pipe switches can be observed together with the special capacitor layout. Figure 14 shows a side view of the SF_6 trigatron crowbar switch, with the control trigger on the top section and the input resistors at the bottom of it. Figure 15 shows the high voltage feedthrough inside the vacuum chamber with one electrode in place. The current return is measured using a current transformer T&M (CT series). The voltage is measured with a calibrated C_uSO_4 voltage divider matched to 50Ω output.

The vacuum is monitored using an ion gauge (Huntington IK–100) with a controller (Varian #843). All testing was done with a diffusion pump system as shown in Figure 12. Samples were tested at an average pressure of 7×10^{-6} Torr with a minimum of 1.1×10^{-7} Torr and a maximum of 4×10^{-6} Torr.

Table 2. Mega-Marx specifications.

Maximum Voltage Output:	1.1 MV
Pulse Width:	$100 \leq t \leq 3000$ ns
Rise Time:	$30 \leq t_R \leq 100$ ns
Maximum Current:	$3.5 \leq I_m \leq 8$ kA
Series Load:	$50 \leq R_L \leq 300\ \Omega$
Total Capacitance (erected)	10 nF
Total Inductance:	2 μh
# Capacitors:	22
# Switches:	11
Crowbar	SF_6 trigatron
Instrumentation:	$CuSO_4$ voltage divider
	CVR current monitor

The Marx is configured so that it could be split into two 550 kV independent generators. The timing between Marx triggering and crowbar is controlled by using Maxwell's 40150's delay generator. The Marx and crowbar are triggered by a PT70/PT55 system with total jitter under 5 ns.

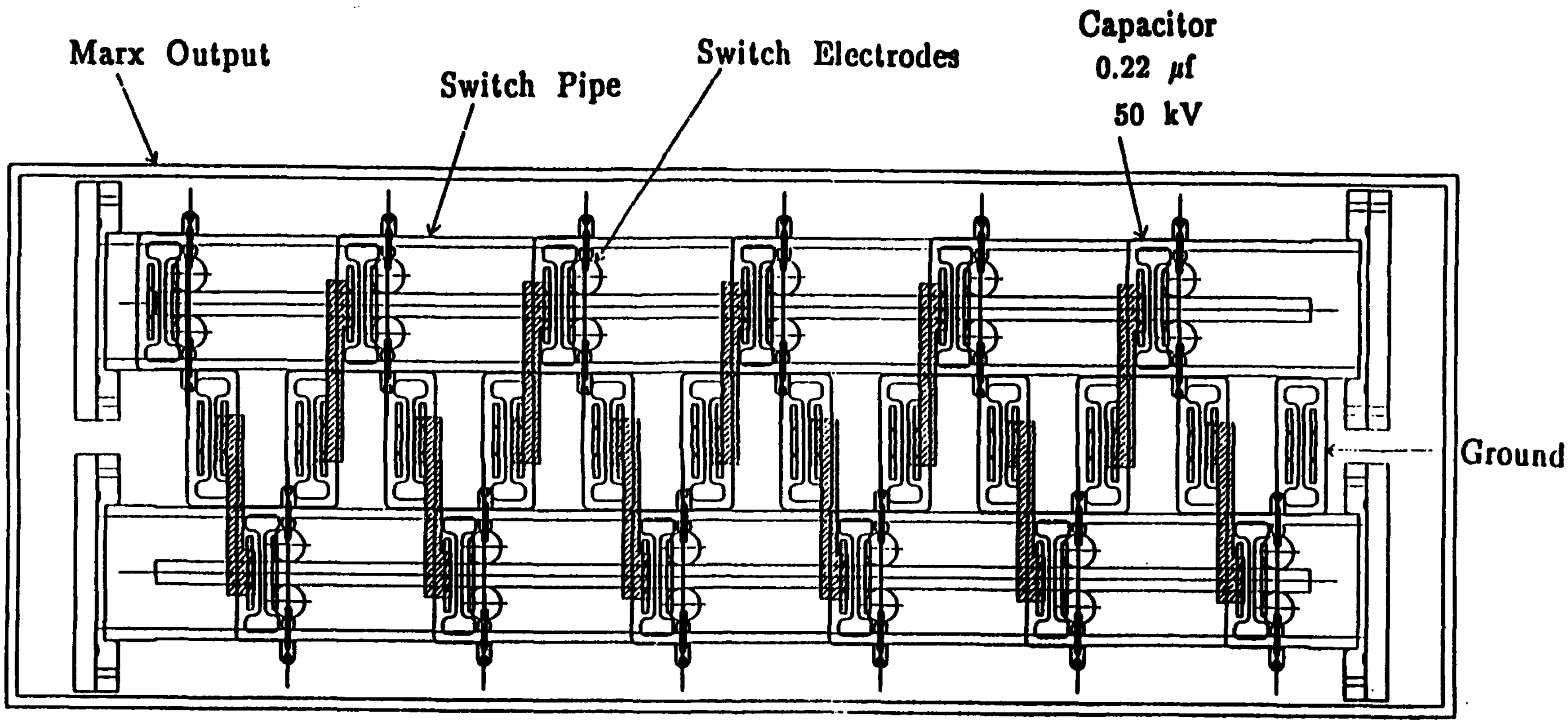

Figure 10. Marx layout top view.

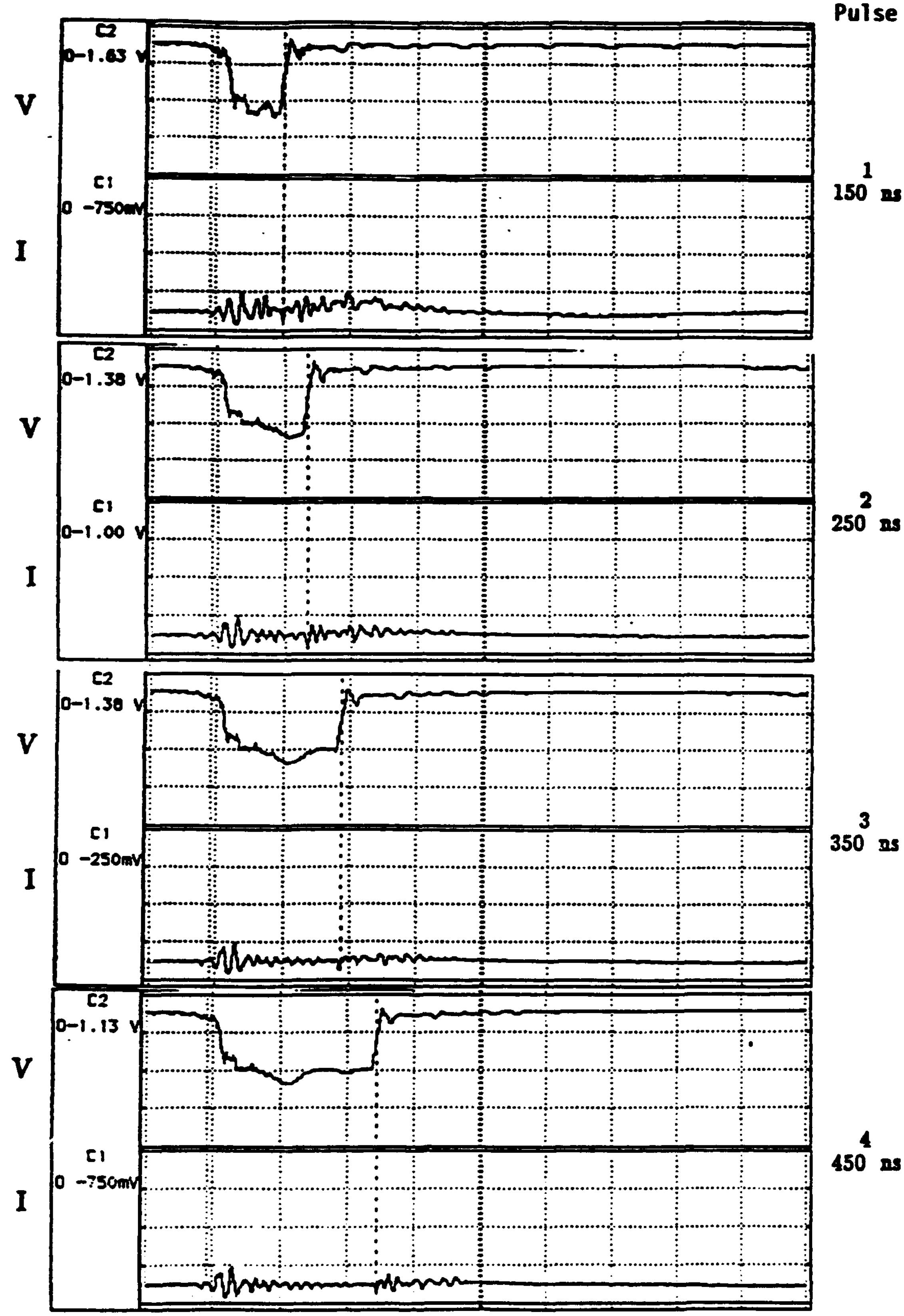

Figure 11. Traces for bare electrode electron emission. For all traces time scale is 200 nsec/DIV, voltage is 180 kV/DIV current is 400 A/volt.

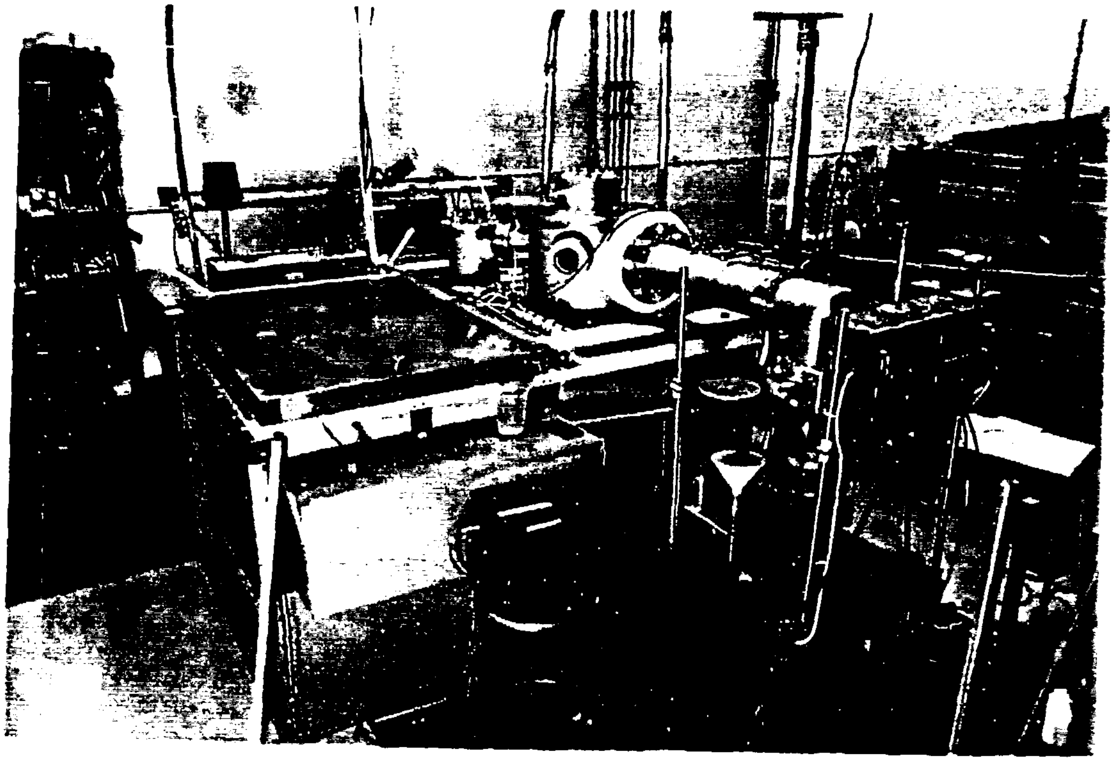

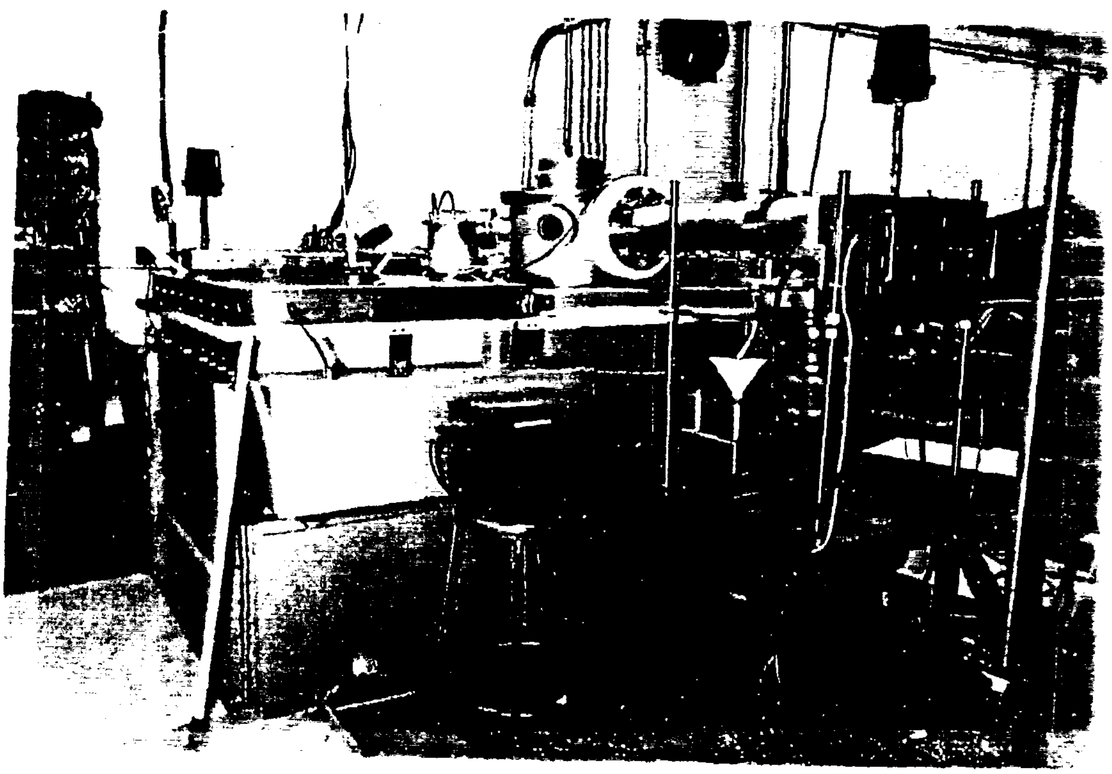

Figure 12 "Mega–Marx" setup with the vacuum chamber and support equipment

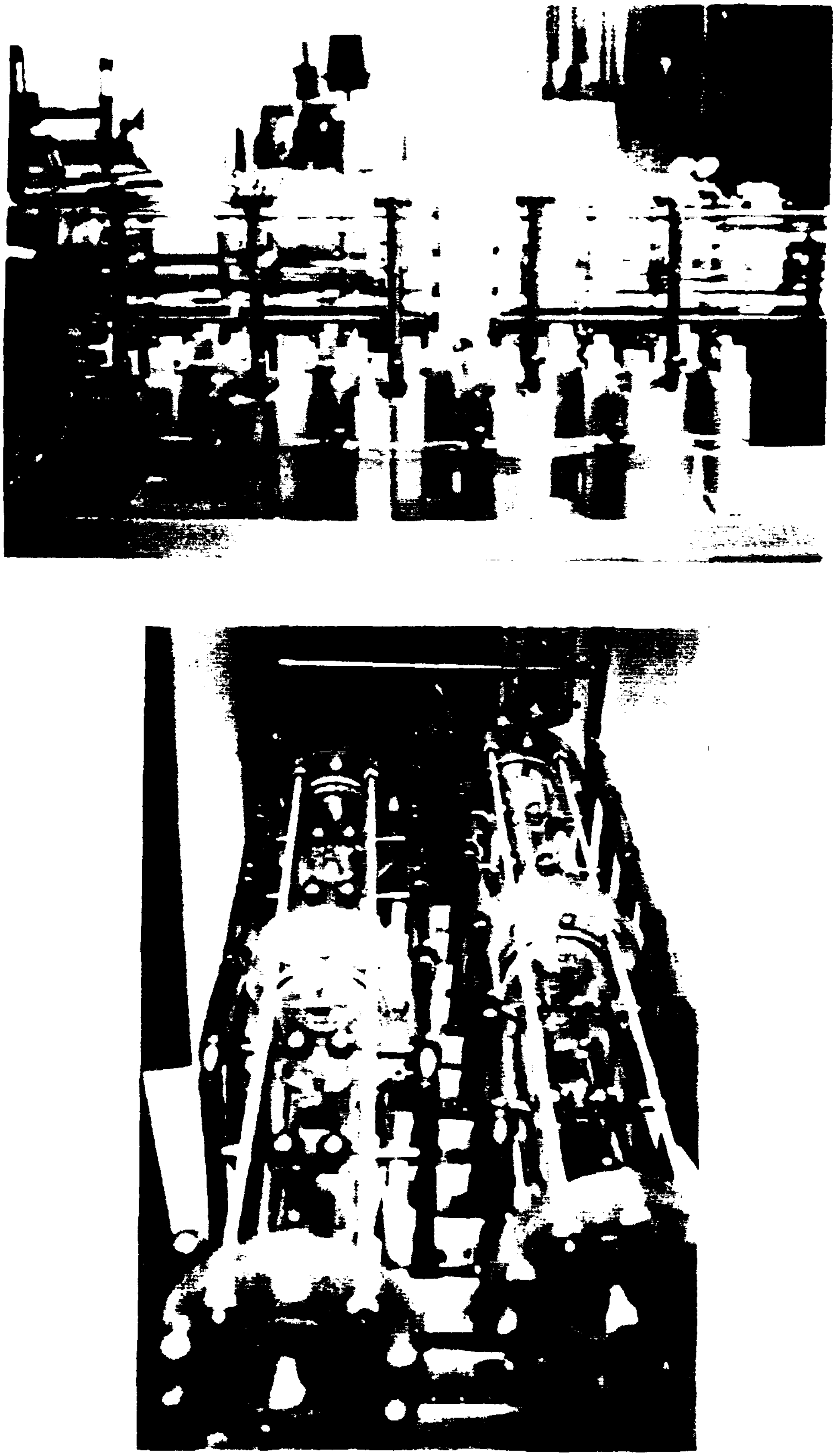

Figure 13 Megavolt Marx layout for fast risetime.

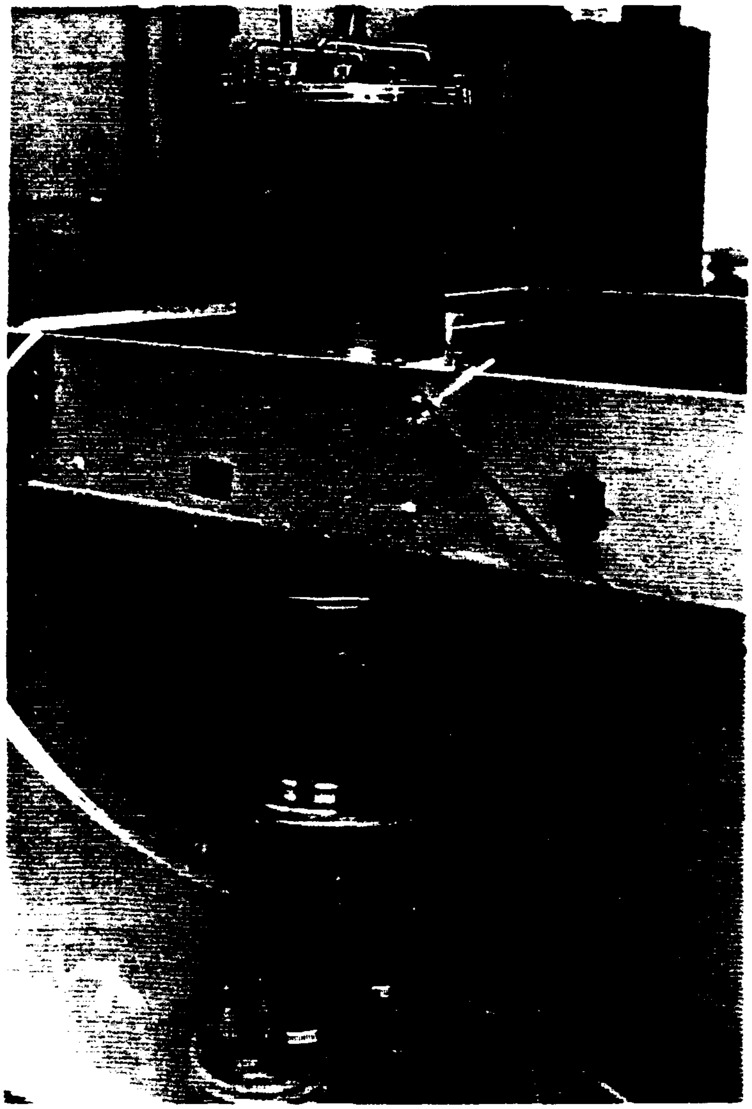

Figure 14. Side view of the trigatron with the trigger pulse on top and the input resistors at the bottom.

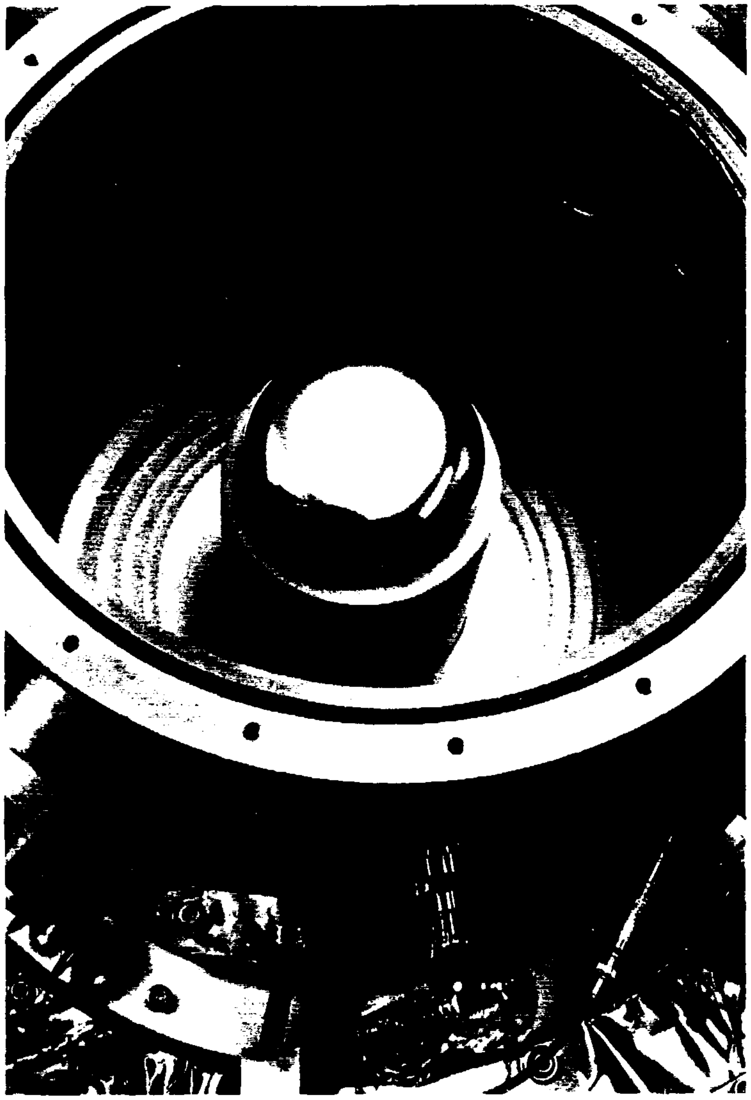

Figure 15. Vacuum chamber high voltage feed–through from Marx.

SECTION 4
SAMPLE CONFIGURATION

The basic program was experimental in nature with a large number of samples tested. Fabricating the samples without using sophisticated methods was part of the challenge. Several materials were eliminated from the original test Matrix as a result of fabrication difficulties. Materials such as copper and tungsten were either too soft or too hard to be machined and handled. Dielectrics such as nylon, teflon, and even polycarbonate were too unstable or melted during the fabrication process (Ref. 14).

The fabrication process was as follows. The method of construction was generally to machine the discs to size (either 1.42" diameter or 1.50" diameter in the case of the straight stacks) and to machine (drill) the appropriate hole in the center of the discs. A cylindrical heater constructed of aluminum silicate and Nichrome V resistance wire was used to heat the preassembled stack while being pressed in a hydraulic press.

In the case of the conical insulator with straight conductor stacks, the insulators and adhesive were machined conical with simulated conductor thickness. The machined conical stacks were then disassembled, disc–by–disc and reassembled with the appropriate number of insulator pieces, with a 1.50" diameter conductor being inserted in place of the simulated conductor. Then the stack was placed into the heater and pressed.

Most samples were fabricated following this procedure. After 24 hours curing time, the sample is polished to avoid flaws in parallelism.

A total of 100 samples were fabricated with 81 tested. Some of them were tested at 0°, 15°, 30°, and 45°. Figure 16 shows a typical group of samples made with Mylar (0.010") and stainless steel (0.010"). Figure 17 shows some of the samples after being cut to a 45° inclination. Figure 18 shows a typical group of samples made with Kapton (0.005") and stainless steel (0.010"). Figure 19 shows samples with the metal recessed from the dielectric.

The first series of samples were built using mylar and stainless steel. The mylar thickness is 0.010" and the SS thickness is 0.005". The epoxy holding the layers together is about 0.001" thick. Table 3 describes a typical Matrix of different thicknesses and ratios:

Table 3. Mylar typical sample matrix.

SAMPLE ID	# MYLAR LAYERS	#SS LAYERS	LAYERS RATIO	THICKNESS RATIO
MSI 101A	(40)*	3	10:1	20:1
MSI 81A	(40)*	4	8:1	16:1
MSI 61A	(36)*	5	6:1	12:1
MSI 41A	(36)*	8	4:1	8:1
MSI 21A	(34)*	16	2:1	4:1
MSI 0A	(ALL)	0	—	—

*To initiate and terminate the stack with dielectric material one extra layer of mylar is always added.

In all the samples the metal is shielding the dielectric surface and protrudes 0.040" from the dielectric surface. Most samples are about 1 cm in thickness with the exact dimensions included in the field value reported in the results.

The second sample series was identical to the one reported before to improve on the statistics and to measure the performance of a 45° modification to the microstack. The third sample series involved samples built the same way as the ones presented previously but using kapton instead of mylar. As shown in Figure 17, once the samples are tested at 0°, a cut to 15°, 30° and 45° was made to evaluate the angular dependence of the different samples. The samples were divided in two groups: Mylar based and Kapton based. The Mylar samples were fabricated just as described before. Basically a number of 0.010" thick Mylar wafers was layered and then a metal wafer, typically 0.005" thick stainless steel, was placed in between. Samples with Kapton were fabricated the same way, but the Kapton film was 0.005" thick. The following table describes the matrix of different thicknesses and ratios:

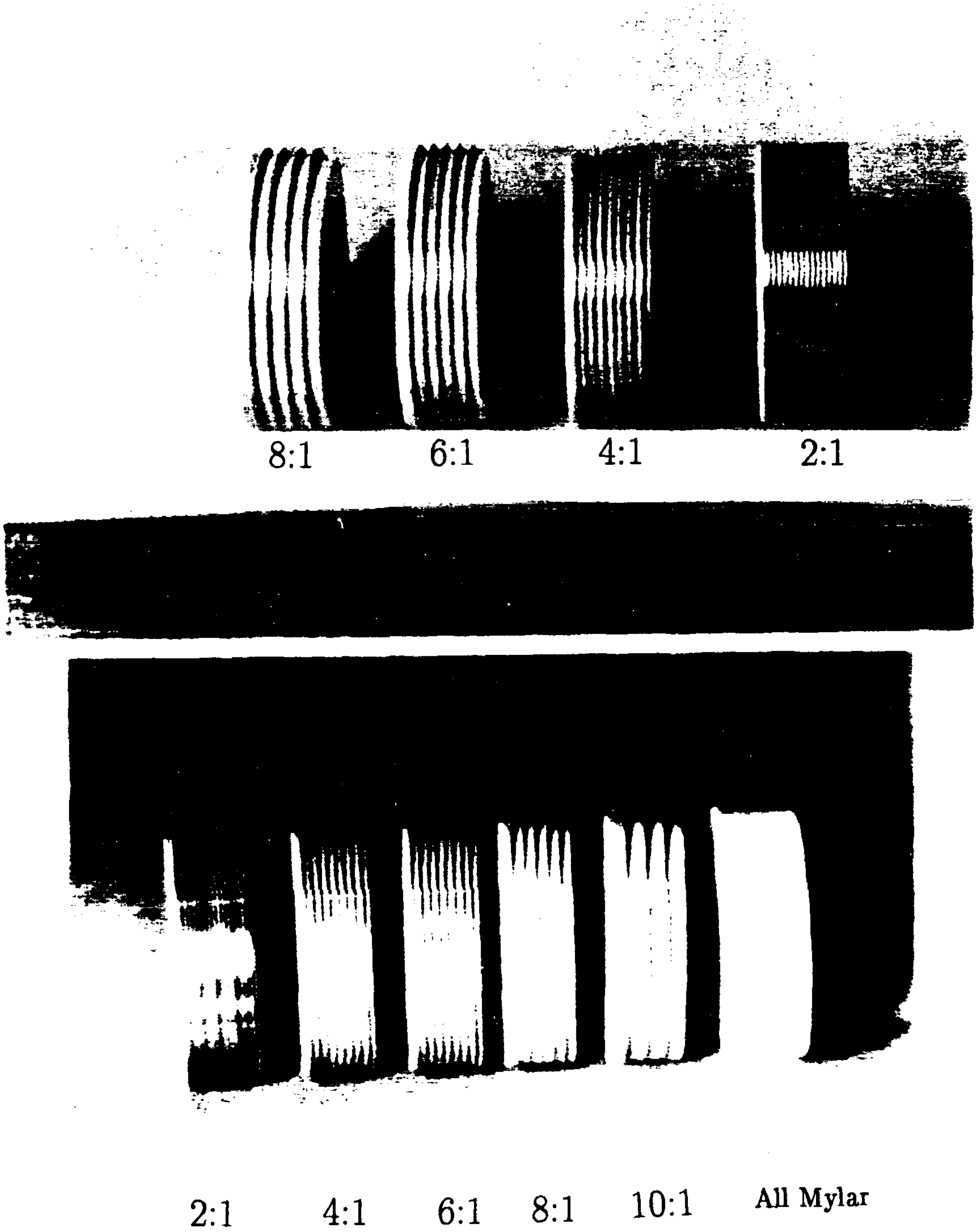

Figure 16 Microstack sample batch to test scaling with respect to dielectric to metal thickness ratio.

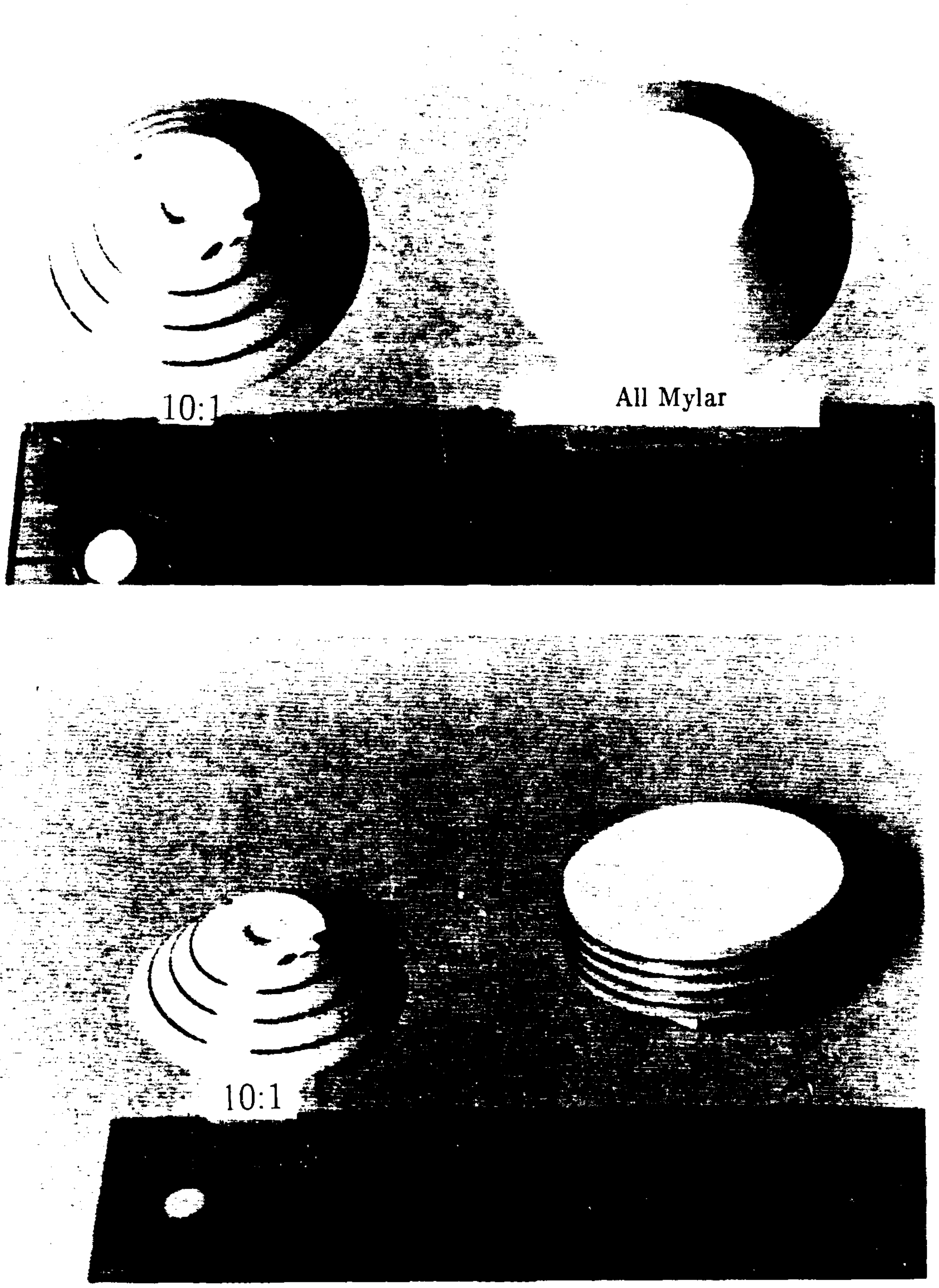

Figure 17. Two samples after being machined out to 45° mylar 10:1 and mylar stack

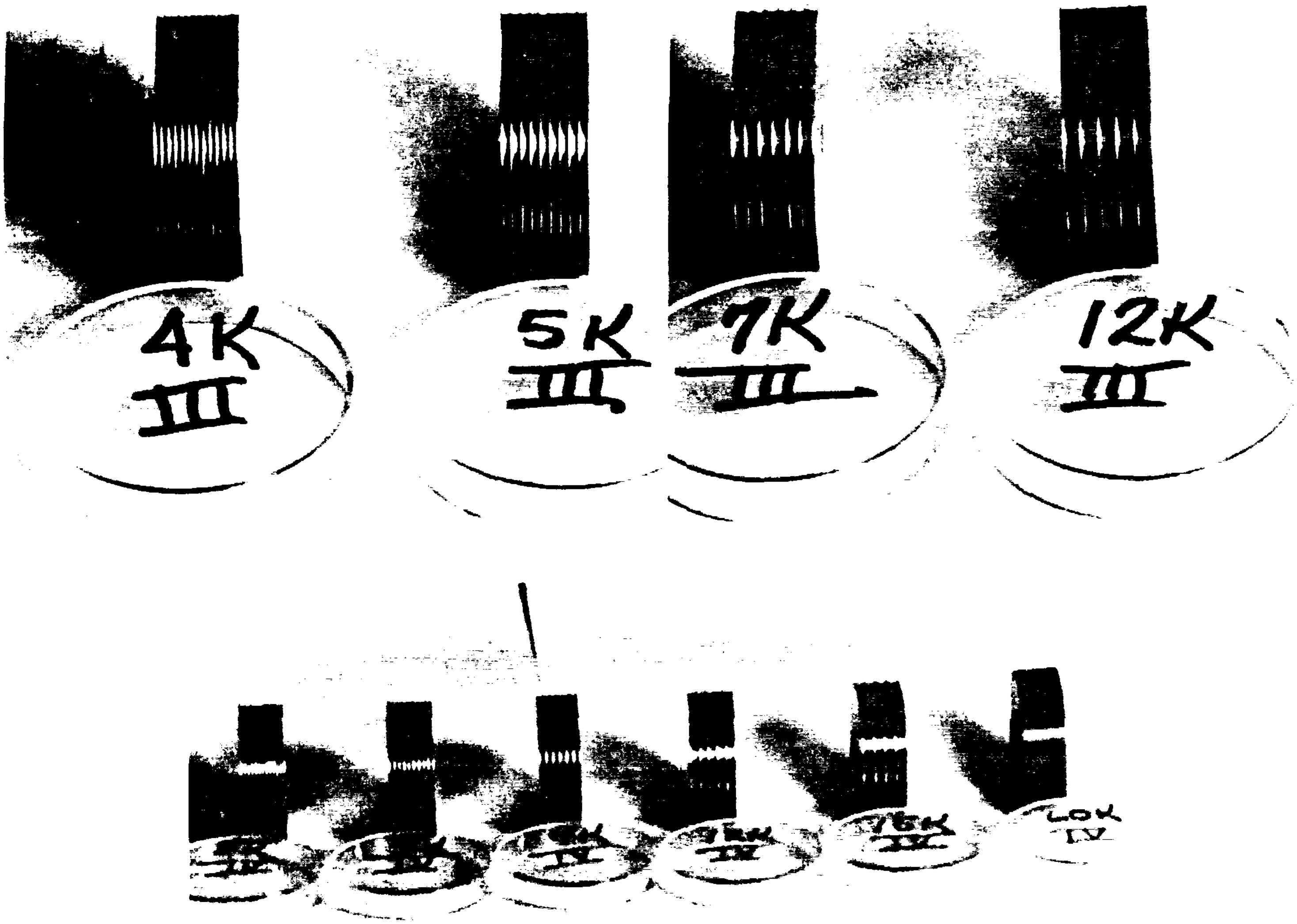

Typical Kapton Samples in its Original Microstack Configurataion

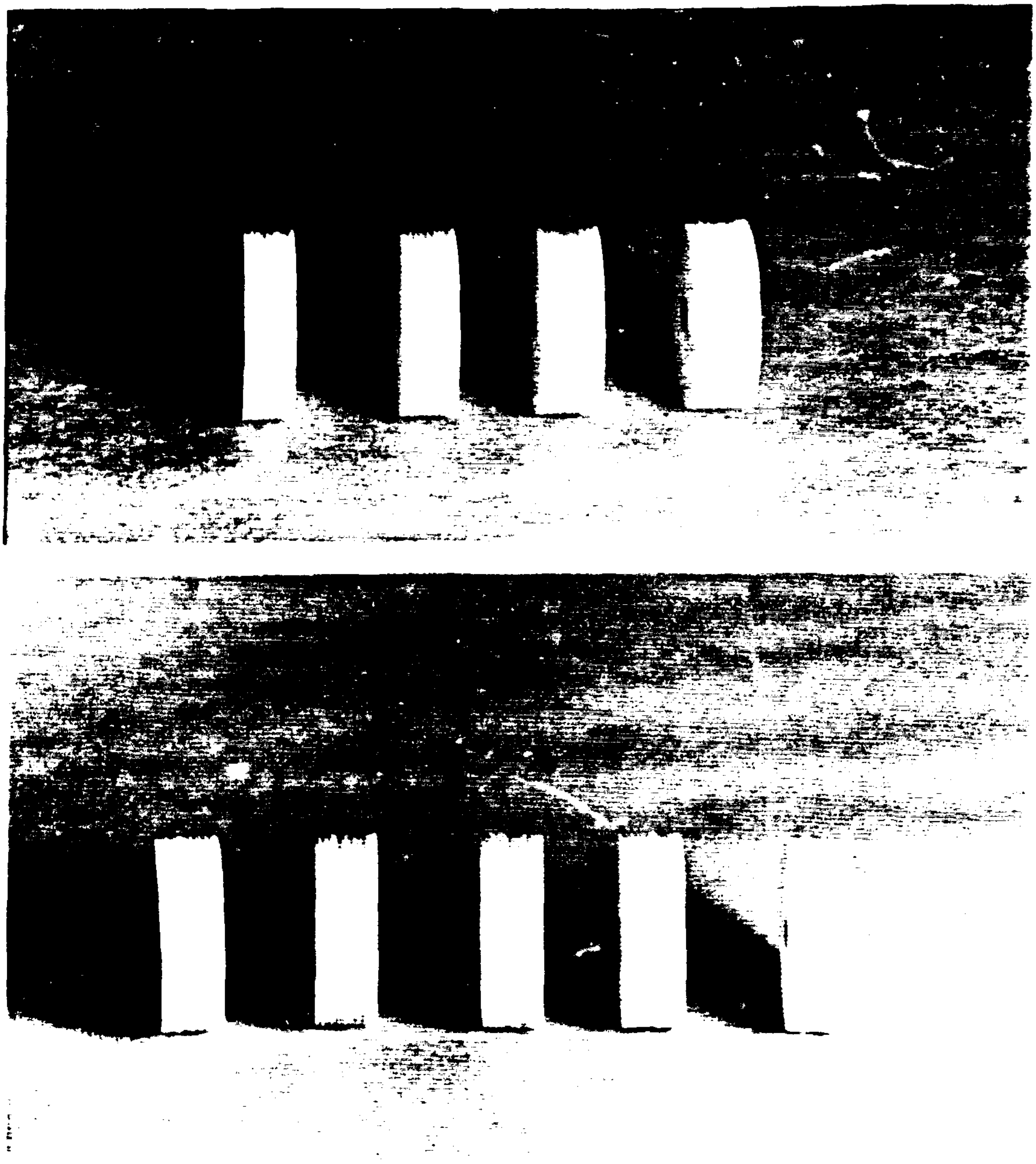

Figure 19   Samples with the metal recessed from the dielectric.

SECTION 5
EXPERIMENTAL RESULTS

The experiments produced excellent results and large quantities of data. The data was compressed as much as possible for publication purposes, but some individual sample data is shown in its entirety. As will be observed in the results, the lowest values obtained show average fields of 200 kV/cm. This is a remarkable trait of the technology to show a minimum failure field of such magnitude. The average field value for most samples is about 300 kV/cm. Chapter 6 will show the results of the final samples where we obtained average fields of 400 kV/cm.

Table 4 shows the condensed peak voltage values for the Mylar test matrix. The category averages and the one sigma deviation are shown. The best values were obtained with the 45° configurations.

Figure 20 shows the data for the all mylar stack. The stack is fabricated by stacking 0.010" mylar on top of each other until 0.400" thick (1 cm) total thickness is obtained. The plot shows the average of 5 pulses vs total field across the sample. Figure 21 shows the behavior per pulse. It can be observed that when the first flashover occurs in the sequence (shot #12). the voltage dips. This is an indication that the sample flashes before the voltage reaches full value.

Figure 22 shows the average field (kV/cm) for 5 shots versus shot numbers for the sample with a 2:1 layer ratio (4:1 thickness ratio), very similar behavior as the one shown by the previous sample. A difference is that a more consistent climb is observed in the voltage. With this sample, we can reach 15 shots without a failure. Figure 23 shows the individual shot statistics. All pulses after #16 produced a flash with a shorter time delay.

Figure 24 is the data for the sample with the 4:1 layer ratio (8:1 thickness ratio). A much better statistical behavior is observed with a probable region of conditioning between 20 and 35 pulses. A dramatic improvement with respect to the last 2 samples in the total number of pulses and in total voltage hold off. Figure 25 shows the individual shot behavior. The changes in the voltage pulse are due to variations in the marx output, which in this case shows a ± 10% (not bad for 100 nsec pulses).

Table 4. Layers ratio for Mylar and Kapton samples.

MYLAR	(QTY)	KAPTON	(QTY)
10:1	4	20:1	2
8:1	4	16:1	2
6:1	4	12:1	2
4:1	4	8:1	2
2:1	4	4:1	2

In all the samples, the metal is shielding the dielectric surface and protrudes 0.040" from the dielectric surface.

Figure 26 shows average field values for 5 shots vs shot number for the sample with a 6:1 layer ratio (12:1 thickness ratio). The symbol towards the end of the plot (X) marks when flashing was observed. A very similar curve compared with the 4:1 sample. These two samples begin to show the best field value (~ 200 kV/cm) before flashover. The next batch of samples, with variations to the way we arrange the dielectric, will be done starting at this ratio level. Figure 27 shows the individual shot statistics.

Figures 28 to 31 show the data for samples with 6:1, 8:1, and 10:1. Figure 32 shows a summary of the data. By following Figure 32 we fabricated a sample with a thickness ratio of 10:1, but with a 1 to 1 layer ratio. This is dielectric (Lexan) 0.005" (100 μm) with metal (ss) 0.0005" (12.5 μm). Given the metal thickness (half mil) the surfaces are leveled to each other (no metal shielding) the purpose is to see if the thickness ratio of 10:1 as indicated in Figure 32 yields a good flashover value. Figure 33 and 34 show the results, and to this author's knowledge this is the highest value ever achieved in a cylindrical sample with 100 nsec long pulses. Figure 33 shows a 250 kV/cm field before flashover, Figure 34 shows the individual shot behavior.

The second sample matrix consisted of Mylar samples similar to the ones previously tested. The previous results were confirmed as to the performance of the 4:1 and 6:1 layer ratio showing the best results. Figure 35 shows the resume of the four samples tested in its original configuration. Figure 36 shows the behavior of the 4:1 sample.

This 4:1 sample was then modified to 3 different inclinations, O°, 15°, 30°. Figure 37 shows the configurations as tested, the angle of inclination is measured against the vertical axis and the samples are positioned with the cathode at the base of the truncated cone. Figure 38 shows the 4:1 sample results after being tested at the O° configuration. At this configuration, the sample shows a very poor behavior with severe flashing after 10 pulses. The last 10 shots showed consecutive flashing even though it seems to recover.

Figure 39 shows the results of testing the 4:1 sample at 15° inclination with the metal and dielectric wafers leveled to the edge. The sample shows a series of ups and downs after 15 shots. This indicates random flashing after the voltage is increased beyond 220 kV. The operational voltage for such samples is limited at 220 kV as a reliable operating point. Figure 40 shows the results of testing the 4:1 sample at 30° inclination. In all this testing the base of the truncated cone is at the cathode. The inclination begins to show an effect on the maximum voltage sustained by the sample. The results, as compared with those in Figure 36, show a maximum voltage of just under 260 kV. Figure 41 shows the behavior when compared to the original microstack configuration. Testing at 45° was not done with the 4:1 sample, because the sample was destroyed during the last pulses at 30° inclination.

The best values have been at 15° and 45° for different configurations:

a) All Mylar stack 45°, E = 306 ± 12 kV/cm.
Figure 42

b) Mylar 6:1 Ratio 15°, E = 315 ± 6 kV/cm.
Figure 43

c) Mylar 10:1 Ratio 45°, E = 351 ± 16 kV/cm.
Figure 44

d) Mylar 8:1 Ratio 15°, E = 376 ± 1 kV/cm.
Figure 45

The Kapton sample series was tested in its original configuration with the results being within the Mylar statistics. In general, Kapton made no significant difference even though it is a higher temperature material. The high temperature capacity of Kapton was expected to lower the secondary electron emission and thus enhance the flashover voltage. The results are a good indication that the material is not a significant issue since the metal breaks the insulator continuity. Table 6 show the results from the Kapton counterparts.

The best values from the Kapton series were at different configurations:

e) Kapton 6:1 Ratio Original Stack.
$E = 320$ kV/cm

f) Kapton 9:1 Ratio Original Stack.
$E = 306$ kV/cm

g) Kapton 9:1 Ratio @ 15°.
$E = 292$ kV/cm

h) Kapton 6:1 Ratio @ 45°.
$E = 281$ kv/cm

i) Kapton 12:1 Ratio @ 45°.
$E = 382$ kV/cm

Table 5. Mylar samples (all values kV/cm).

	1:1	2:1	4:1	6:1	8:1	10.1	
Mylar Original	214	205 248	247 272	261 275	190 260 272	260 233	$\bar{x}$ = 244 σ = 27
Mylar 0°		225 239	202 245	242	247 207 197	247	$\bar{x}$ = 227 σ = 19
Mylar 15°		225 147	250 171	323 146	382	191	$\bar{x}$ = 227 σ = 80
Mylar 30°		220	298	335 225	135		$\bar{x}$ = 242 σ = 70
Mylar 45°	400 304	193	260	260	383 260	374 260 324	$\bar{x}$ = 301 σ = 63
	$\bar{x}$ = 306 σ = 76	$\bar{x}$ = 212 σ = 30	$\bar{x}$ = 243 σ = 37	$\bar{x}$ = 258 σ = 55	$\bar{x}$ = 253 σ = 75	$\bar{x}$ = 270 σ = 56	

Table 6. Kapton samples (all values kV/cm).

	1:1	4:1	6:1	9:1	12:1	15:1	
Original Configuration	323	244	323	306	259	272	$\overline{X}$ = 287 σ = 31
0°	267	260	250	---	185	295	$\overline{X}$ = 251 σ = 36
15°	---	261	260	292	---	290	$\overline{X}$ = 275 σ = 15
45°	----	----	281	250	382	----	$\overline{X}$ = 304 σ = 56
	$\overline{X}$ = 295 σ = 28	$\overline{X}$ = 252 σ = 8.25	$\overline{X}$ = 278.5 σ = 28	$\overline{X}$ = 282 σ = 24	$\overline{X}$ = 275 σ = 81	$\overline{X}$ = 285 σ = 9.8	

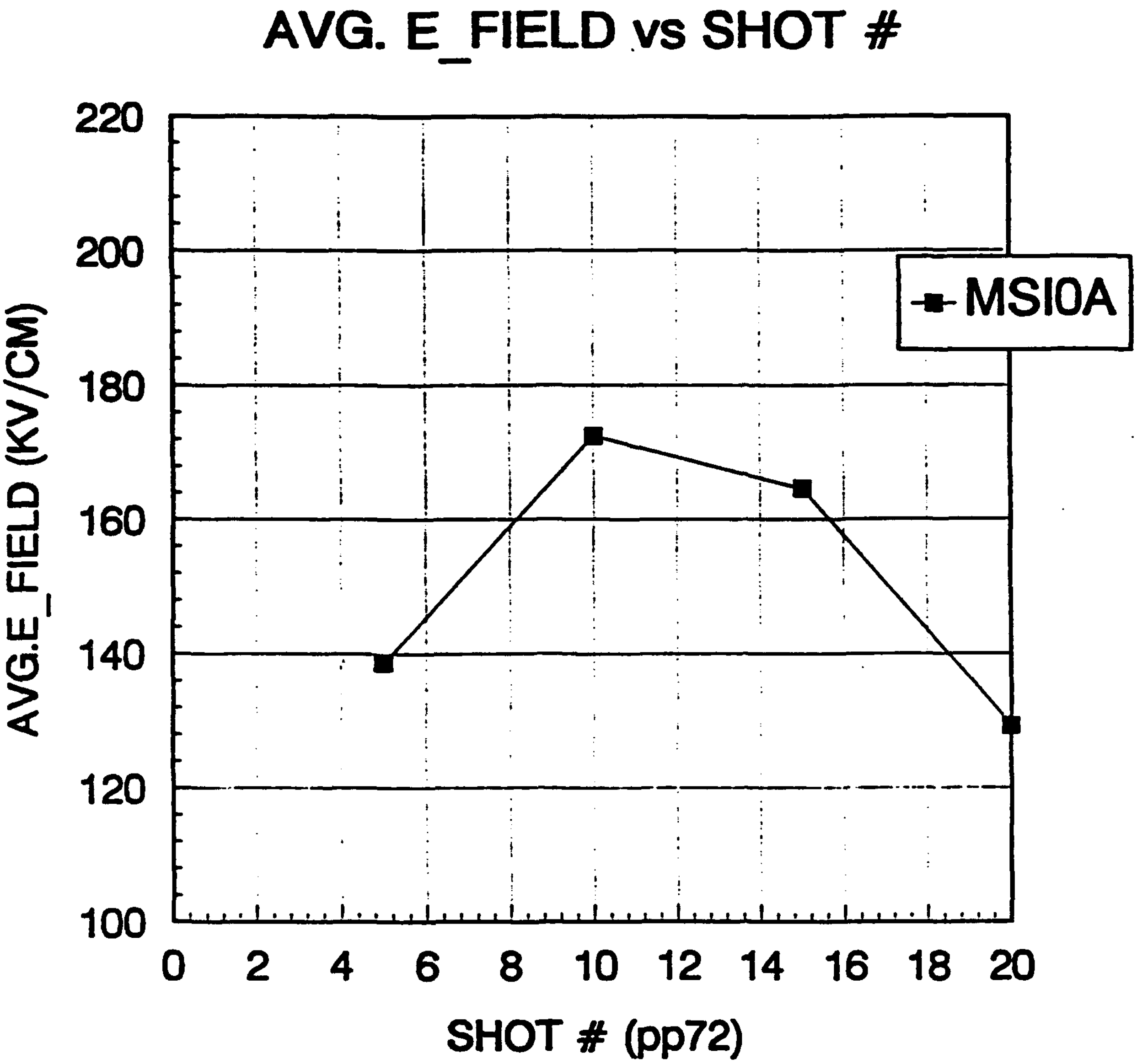

Figure 20. All Mylar sample plot of averaged field (kV/cm) before flashover for 5 consecutive pulses vs pulse count.

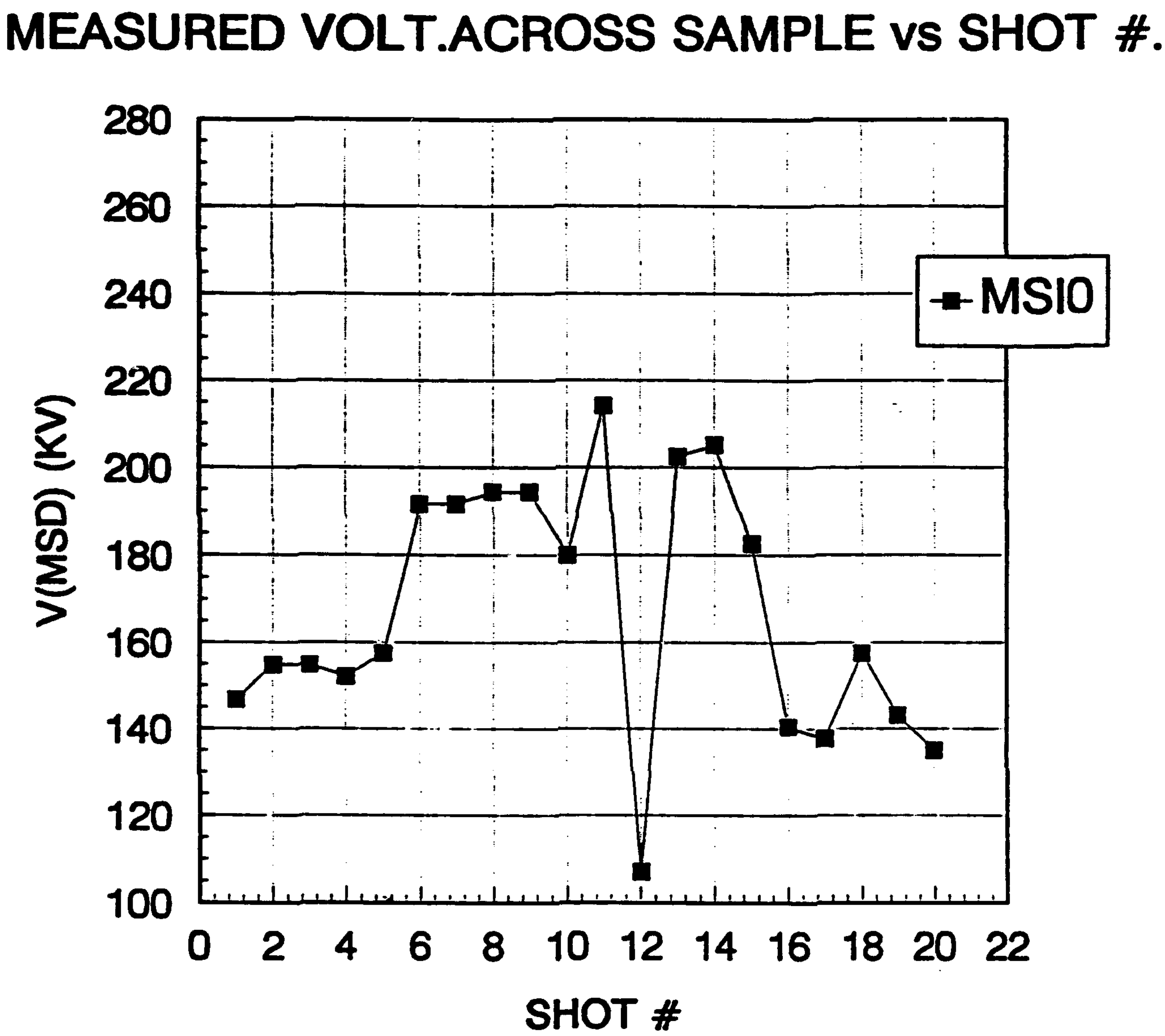

Figure 21. All Mylar sample plot of voltage vs shot count behavior. Deterioration on the voltage hold off ability of the sample can be observed.

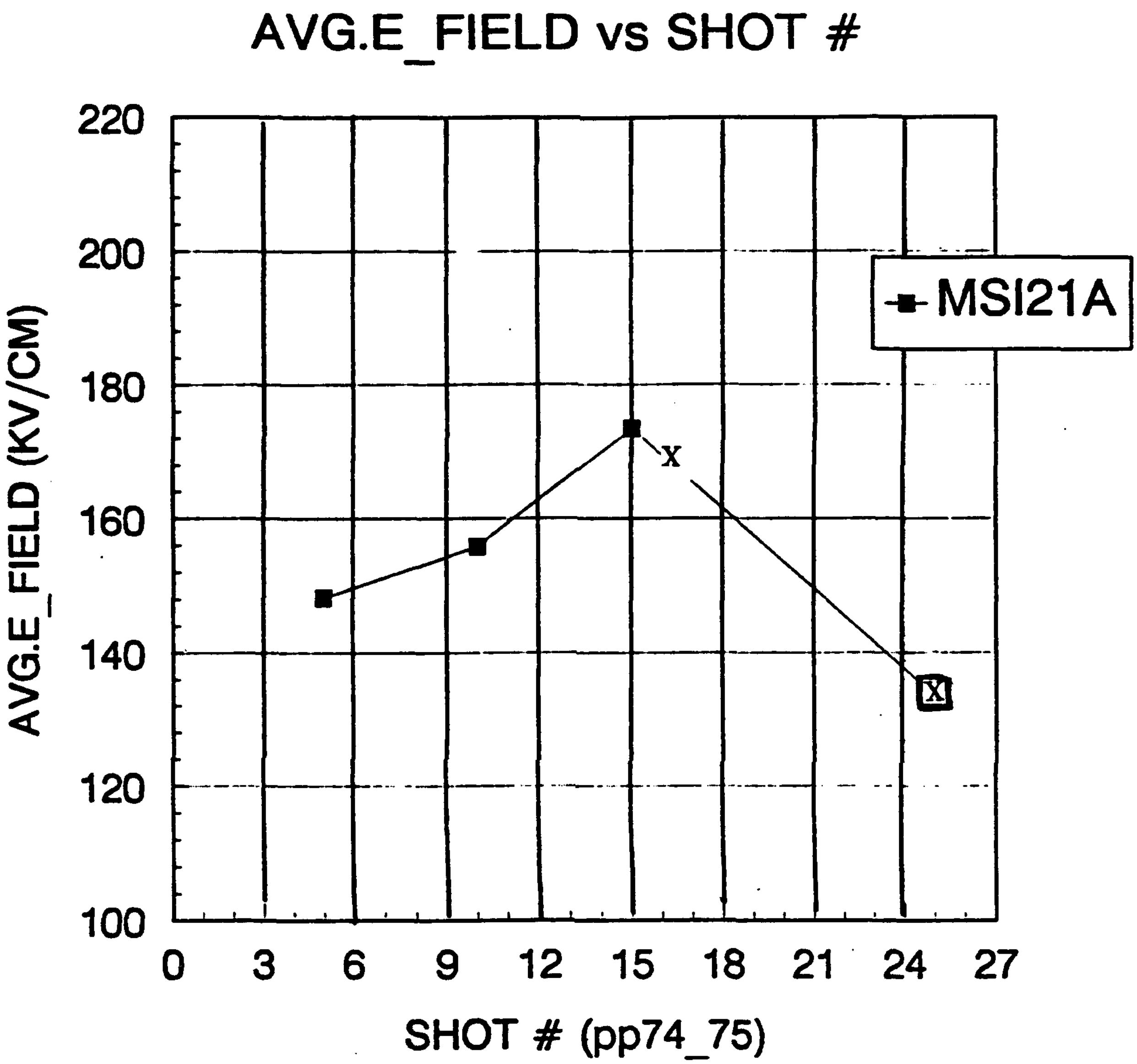

Figure 22. Plot of averaged field (kV/cm) before flashover for 5 consecutive flashes vs pulse count, for the 2:1 layer ratio sample.

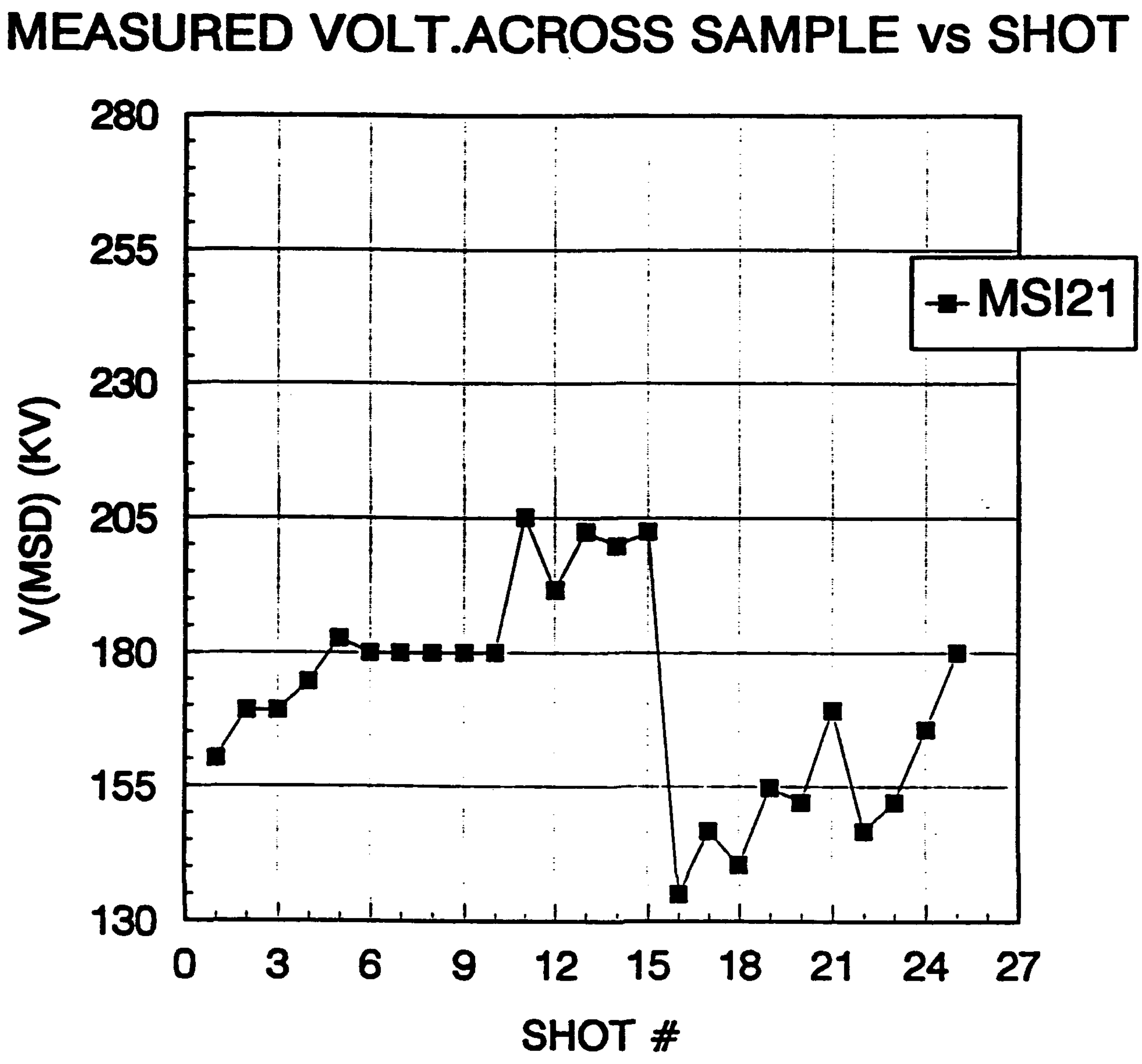

Figure 23. Plot of voltage vs shot count for the 2:1 layer ratio sample.

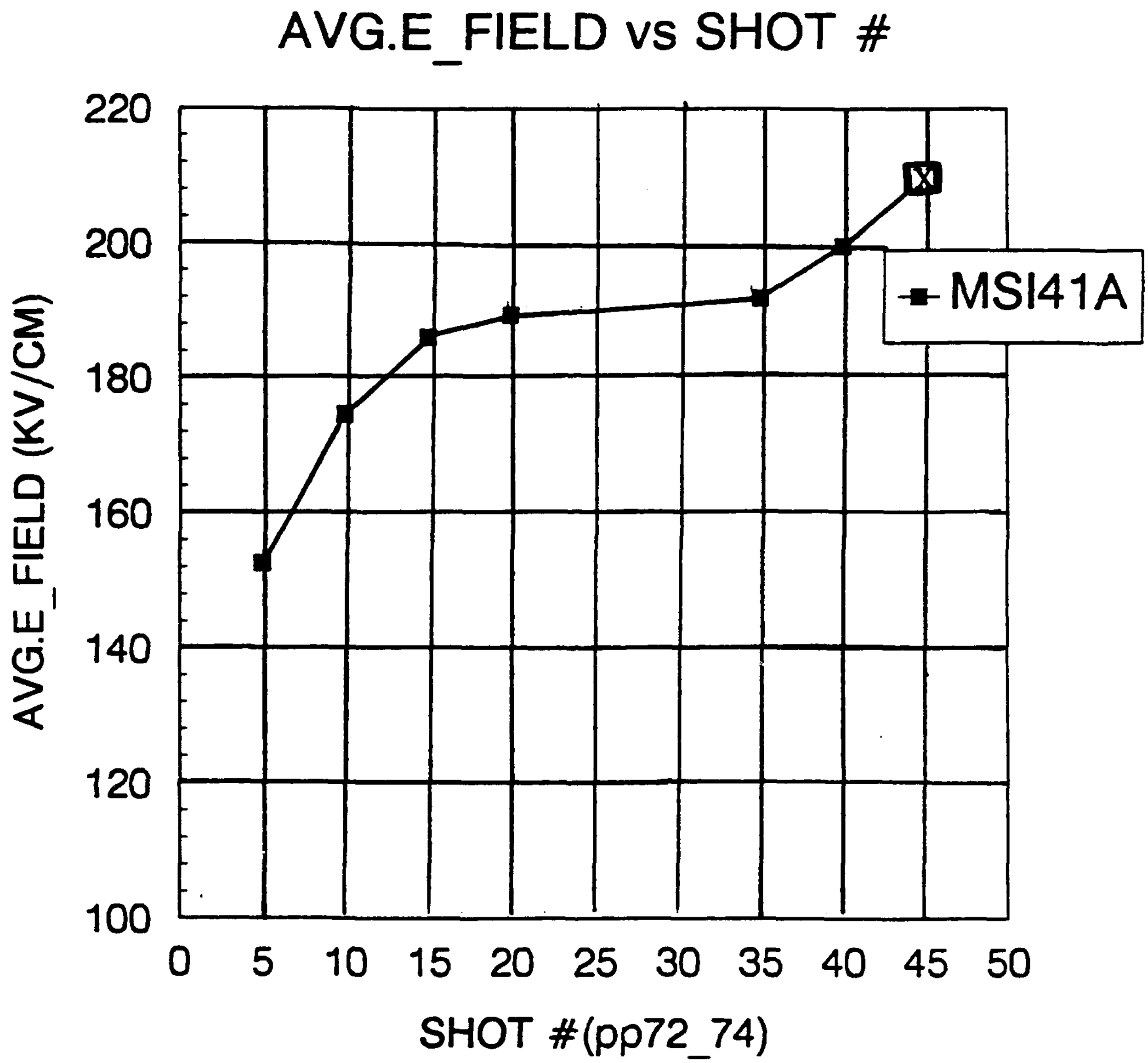

Figure 24. Plot of averaged field (kV/cm) before flashover for 5 consecutive flashes vs pulse count, for the 4:1 layer ratio sample.

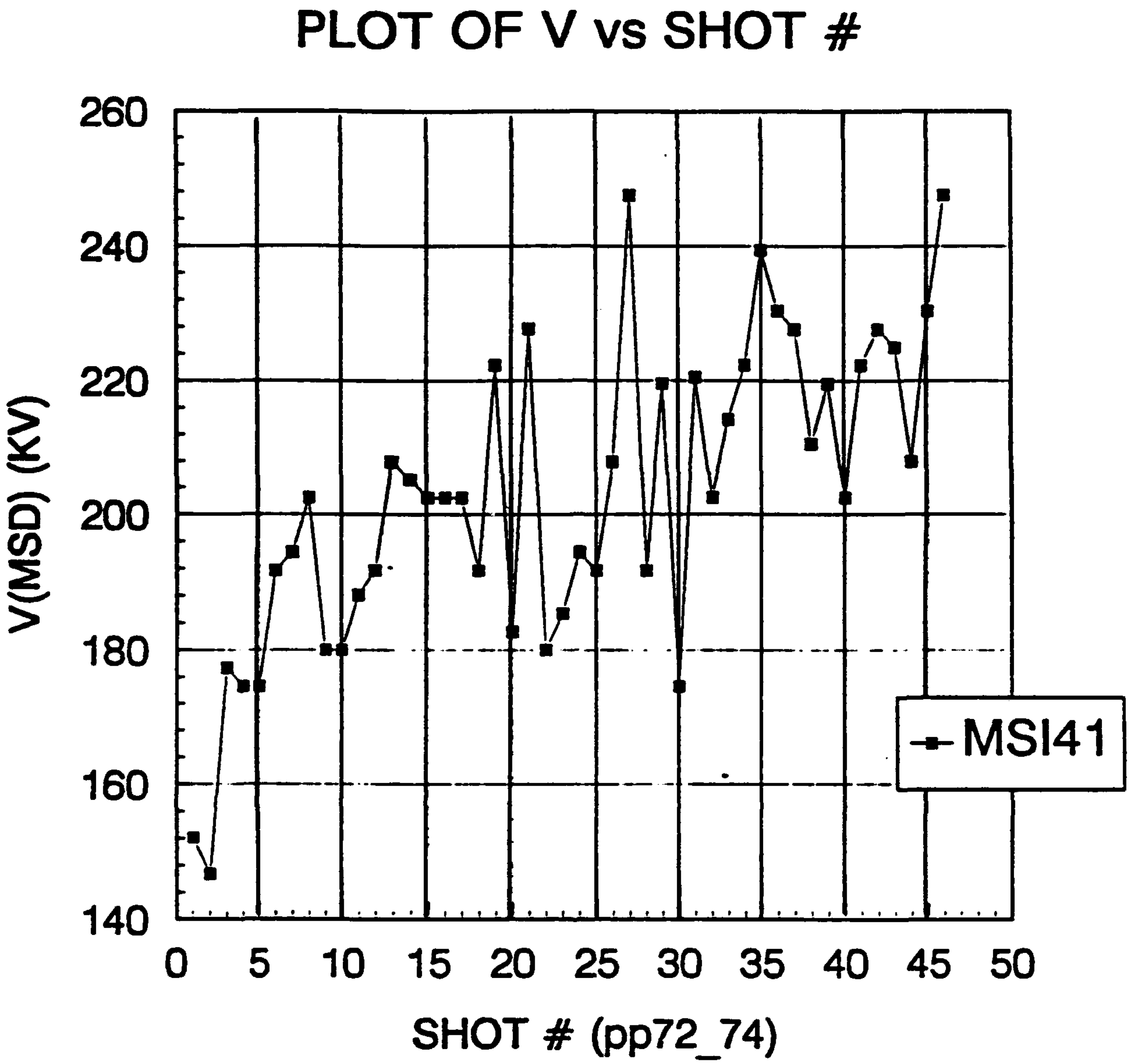

Figure 25. Plot of voltage vs shot count for the 4:1 layer ratio sample.

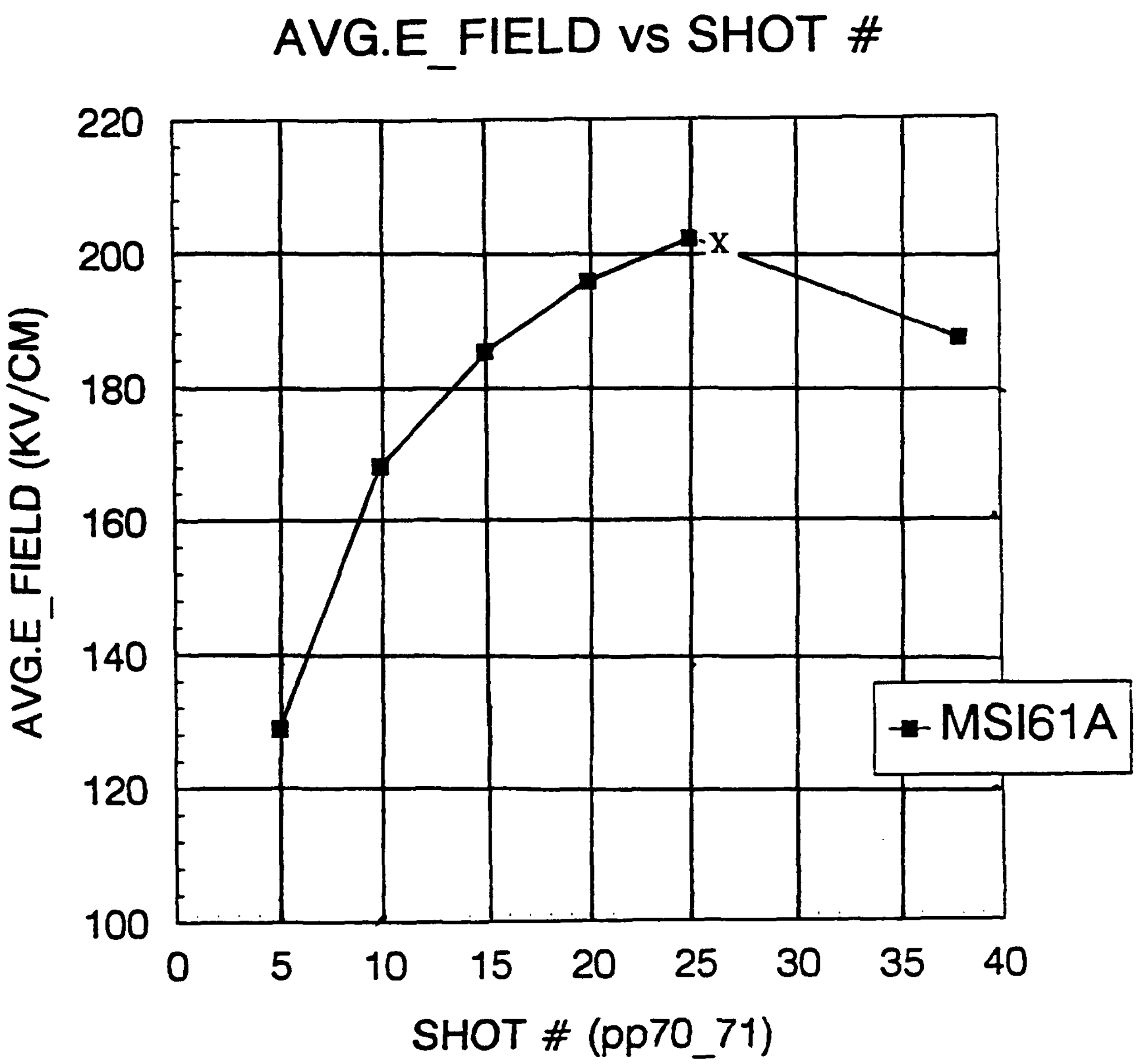

Figure 26. Plot of averaged field (kV/cm) before flashover for 5 consecutive flashes vs pulse count, for the 6:1 layer ratio sample.

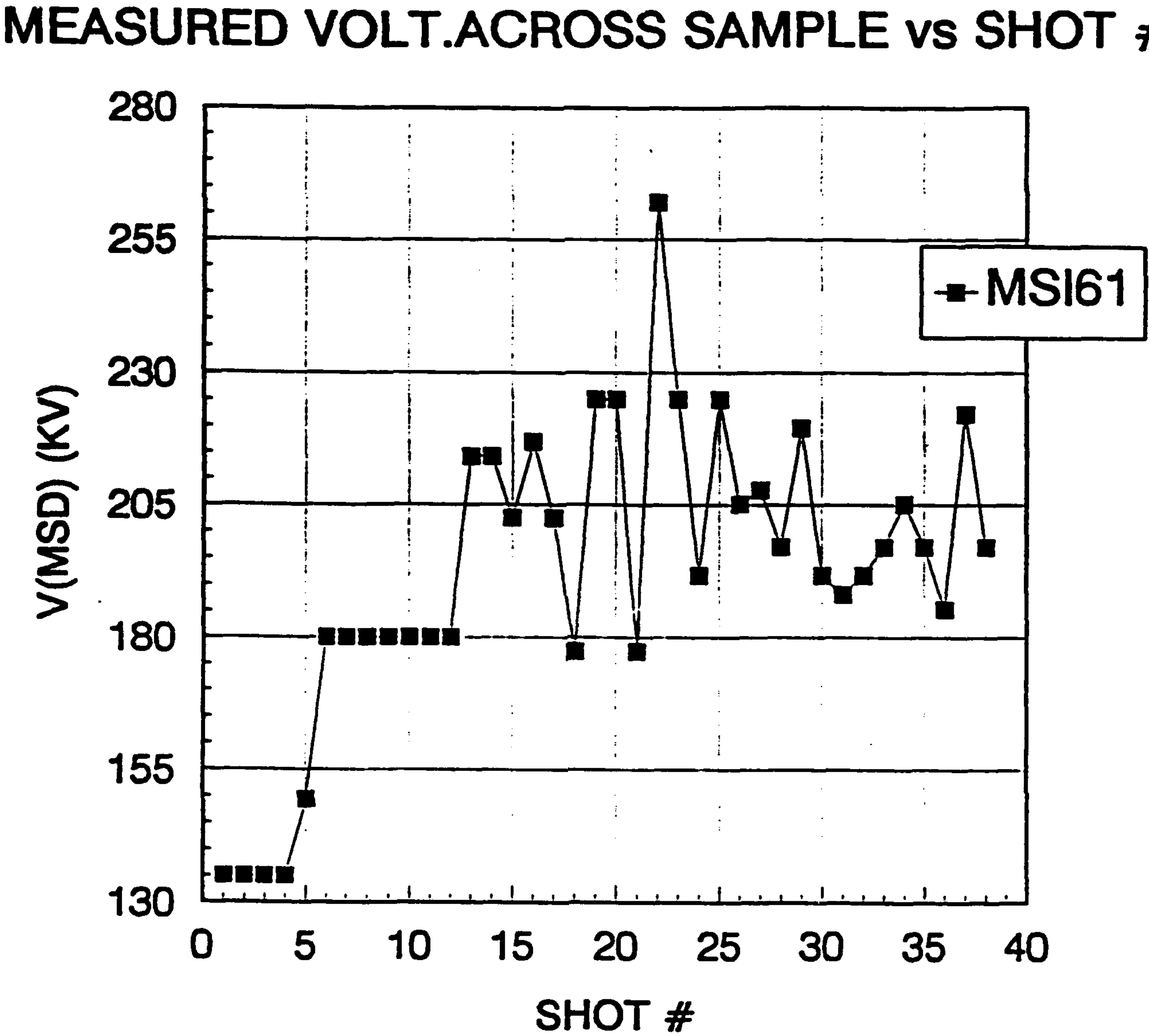

Figure 27. Plot of voltage vs shot count for the 6:1 layer ratio sample.

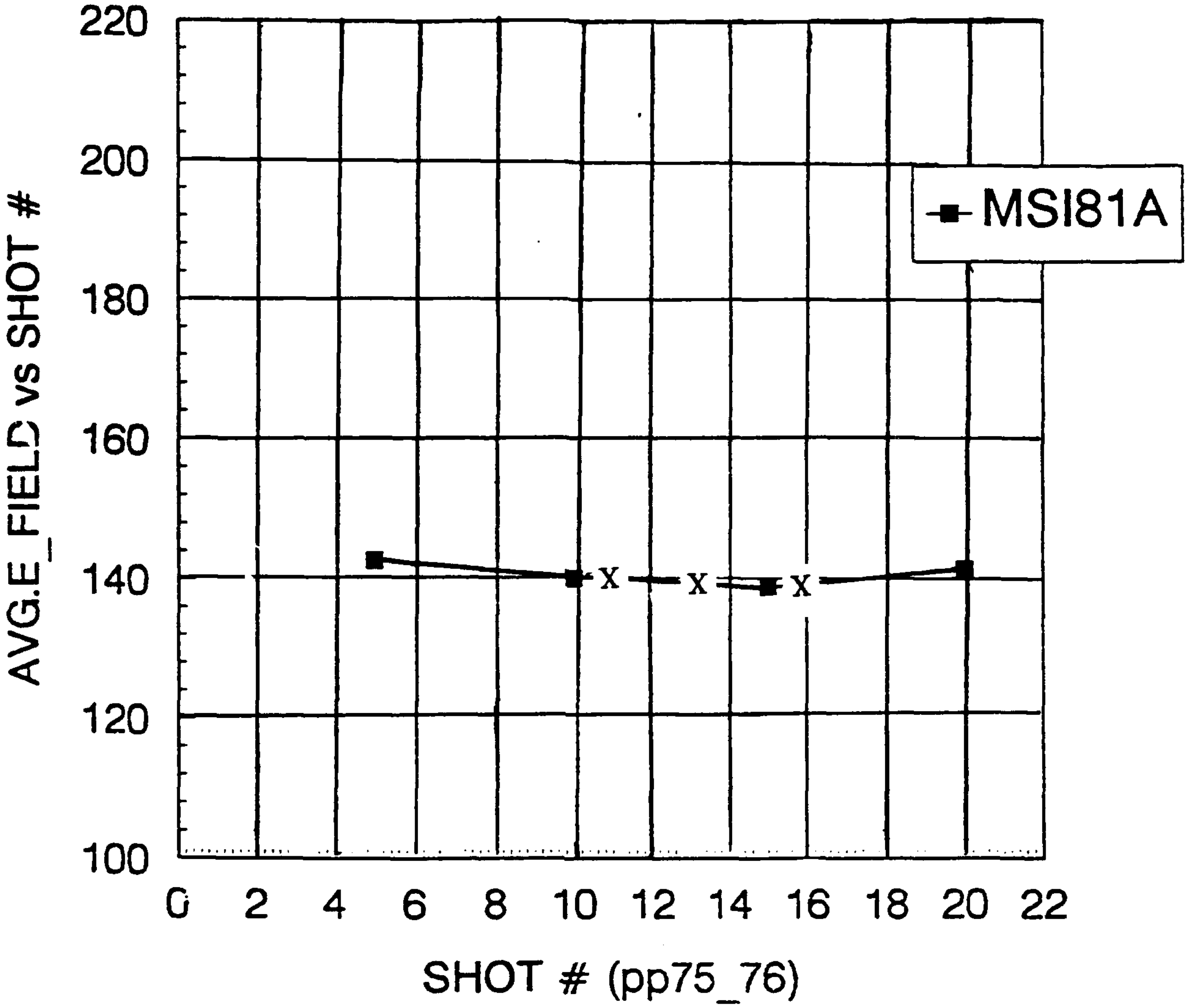

Figure 28. Plot of averaged field (kV/cm) before flashover for 5 consecutive flashes vs pulse count, for the 8:1 layer ratio sample.

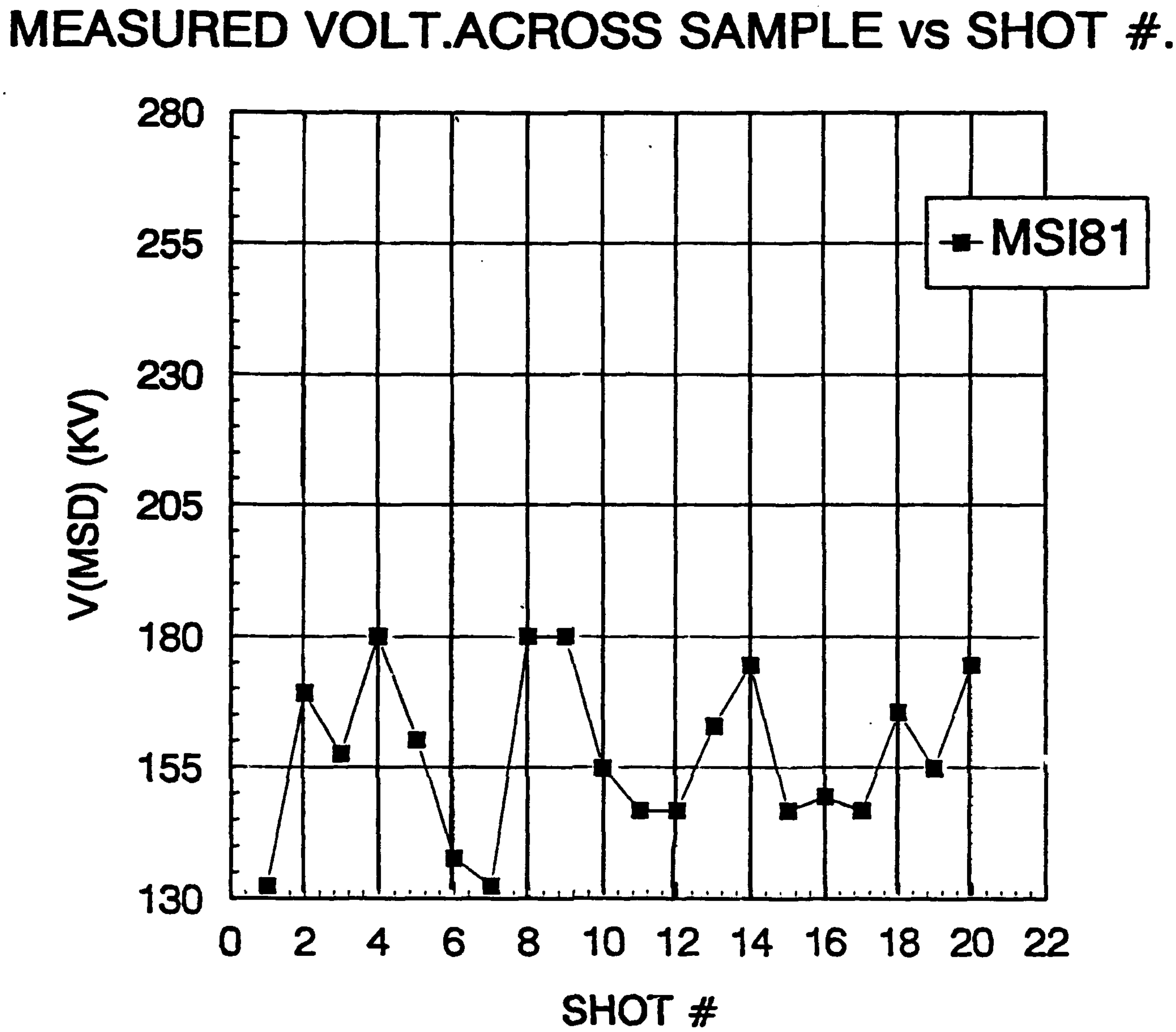

Figure 29. Plot of voltage vs shot count for the 8:1 layer ratio sample.

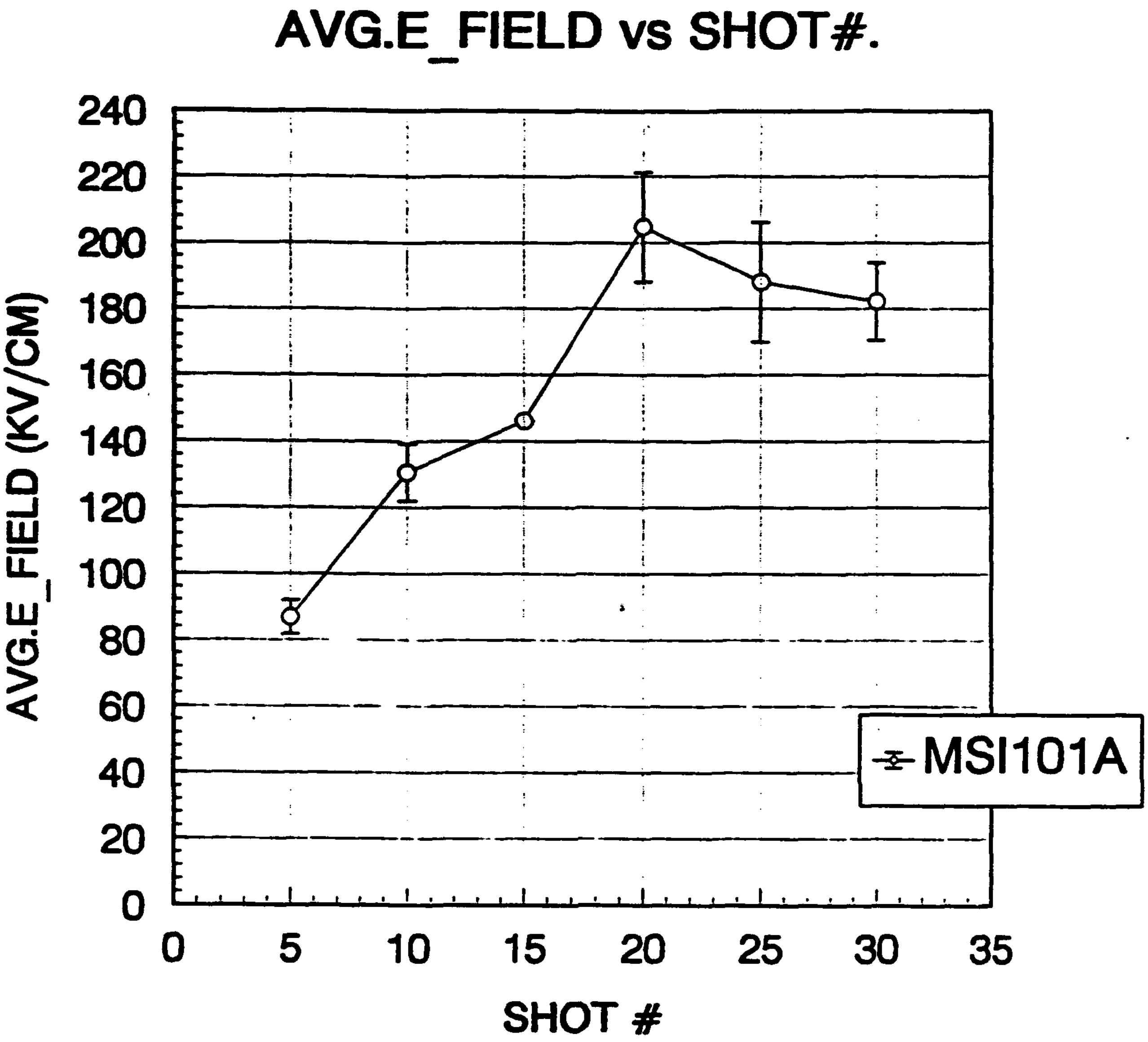

Figure 30. Plot of averaged field (kV/cm) before flashover for 5 consecutive flashes vs pulse count, for the 10:1 layer ratio sample.

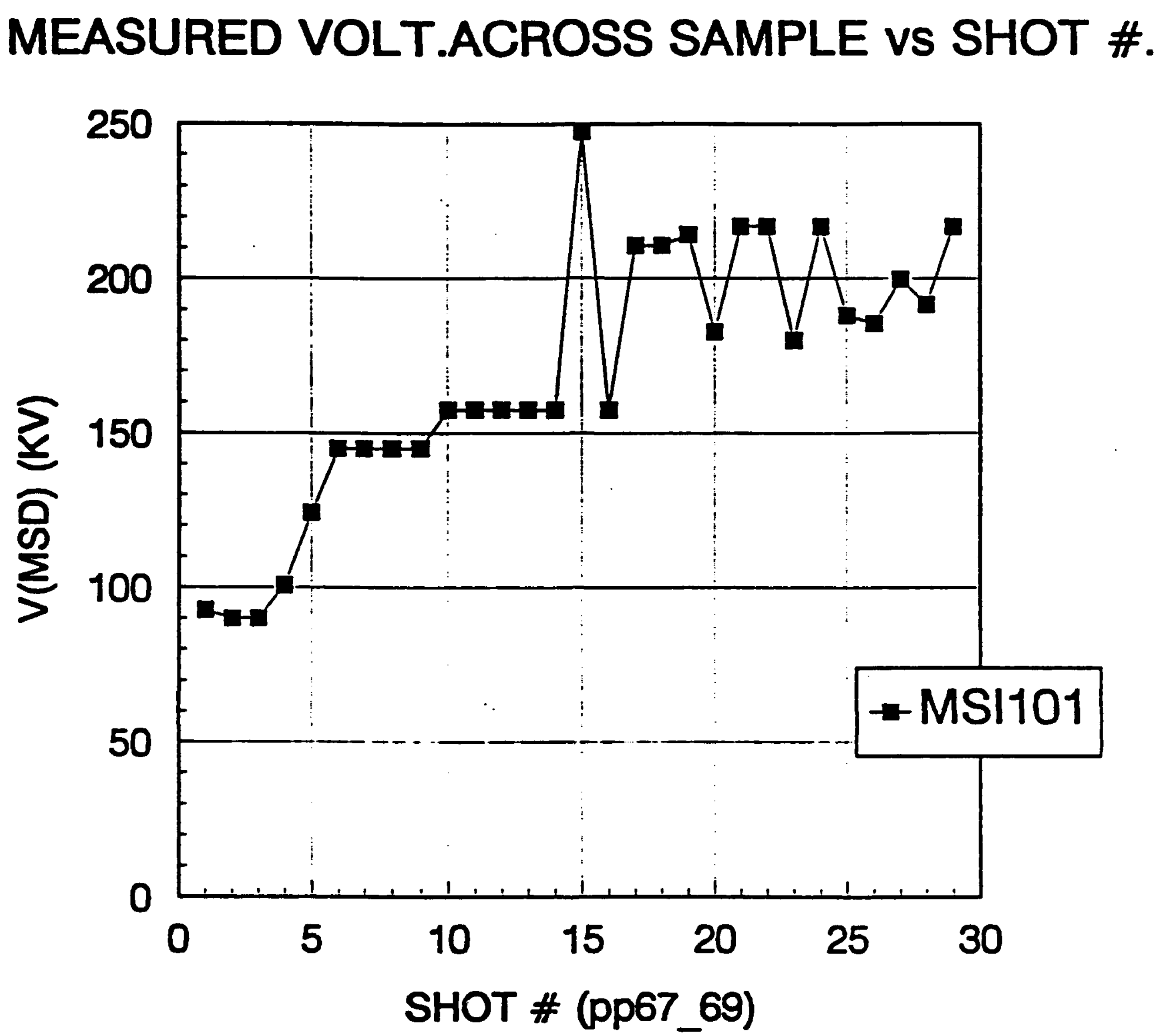

Figure 31. Plot of voltage vs shot count for the 10:1 layer ratio sample.

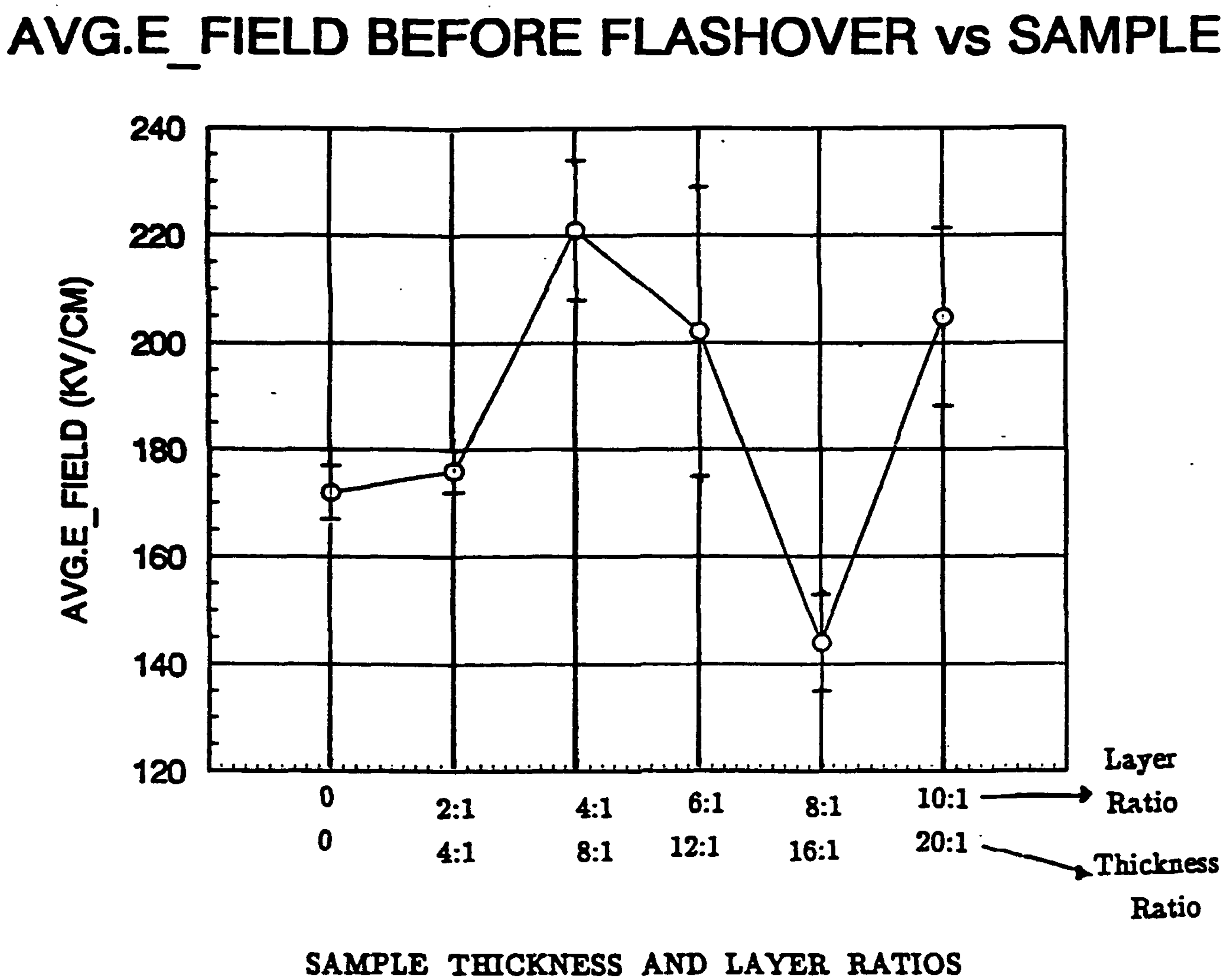

Figure 32. Averaged field (kV/cm) before surface flashover vs sample layer ratio.

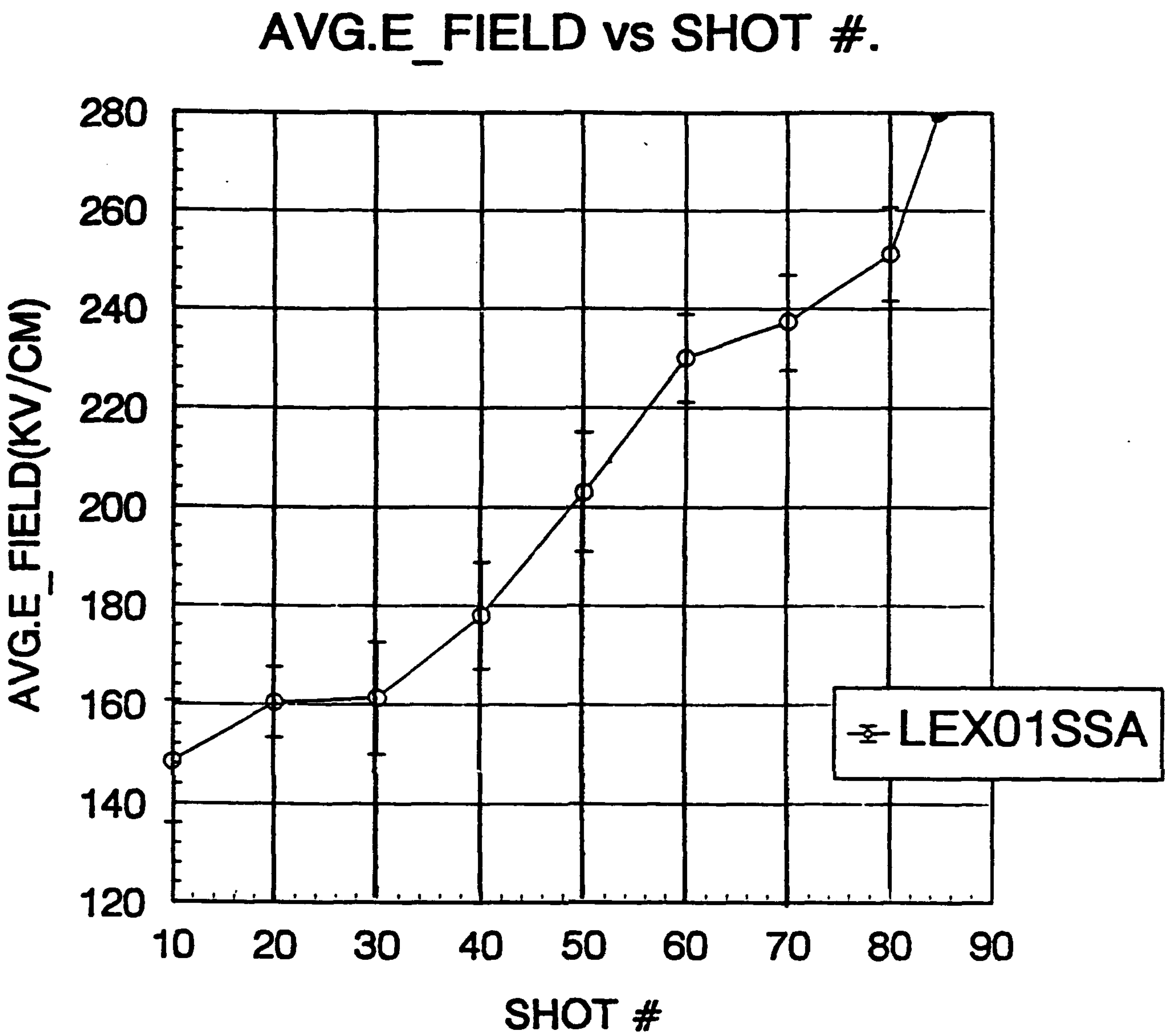

Figure 33. Cylindrical sample made with 0.005" (100 μm) lexan and 0.0005" (12.5 μm), total thickness 1.27 cm. The metal and dielectric surfaces are of the same diameter (no metal shielding effect) the sample is a 10:1 thickness ratio and shows the highest values <u>ever</u> reported for 100 nsec pulse length, before flashover, in non–coated electrodes and no inclination. The figure shows the averaged field and one sigma values for every ten shots.

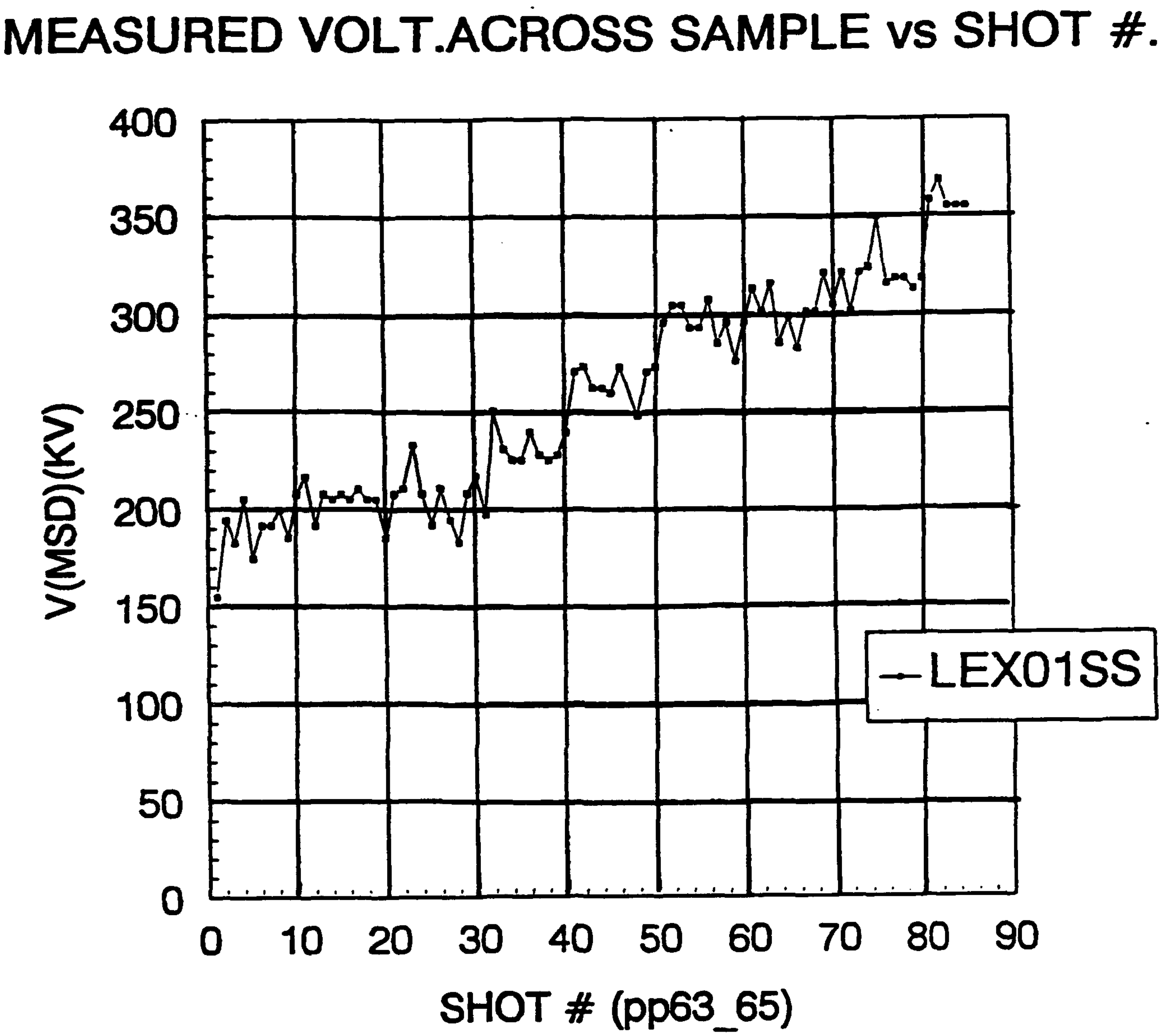

Figure 34. Lexan sample with 10:1 thickness ratio showing the pulse to pulse statistics.

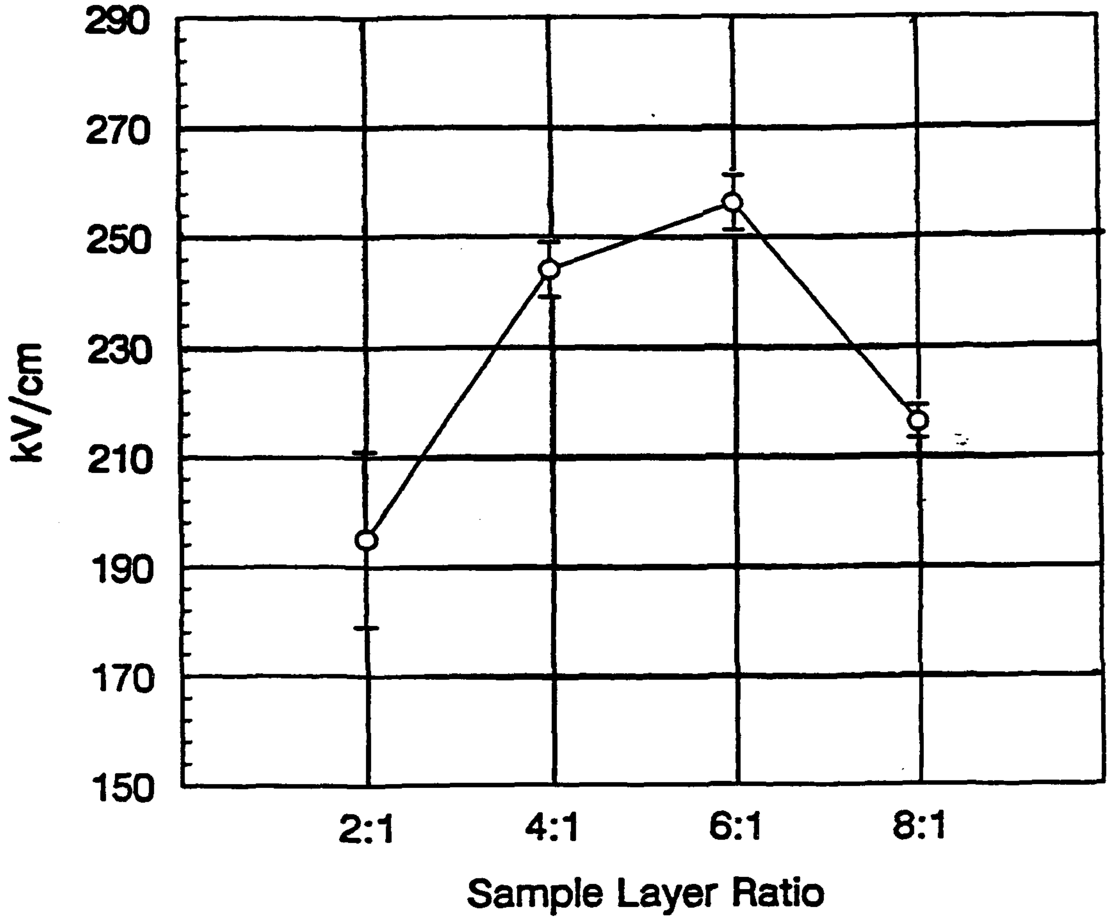

Figure 35. Mylar second set average field before surface flashover vs sample layer ratio.

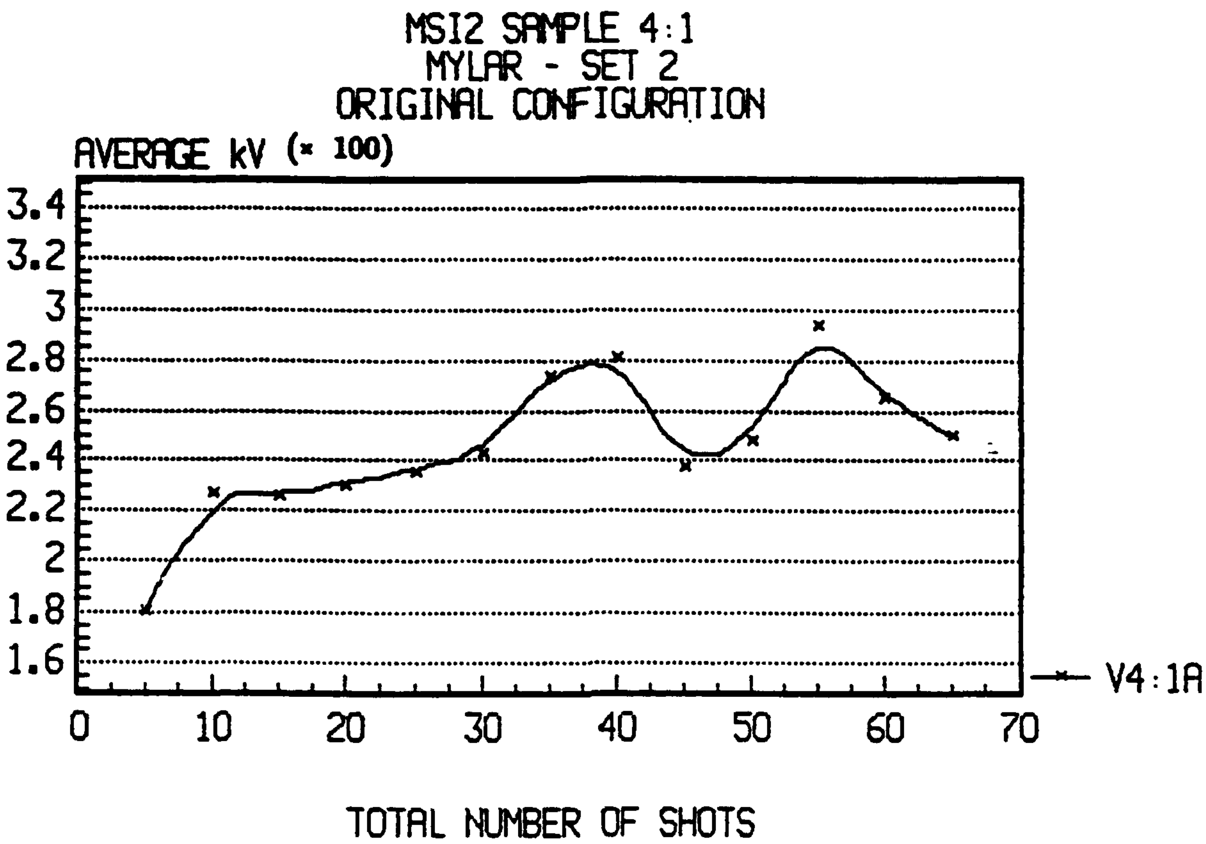

Figure 36. Mylar 4:1 sample from the second matrix tested in its original form. After 40 shots of no observed flashes some flashes are observed within the next ten shots, (Voltage Dips). The sample then recovers for a maximum voltage of ~260 kV after that flash occurred on ten consecutive shots.

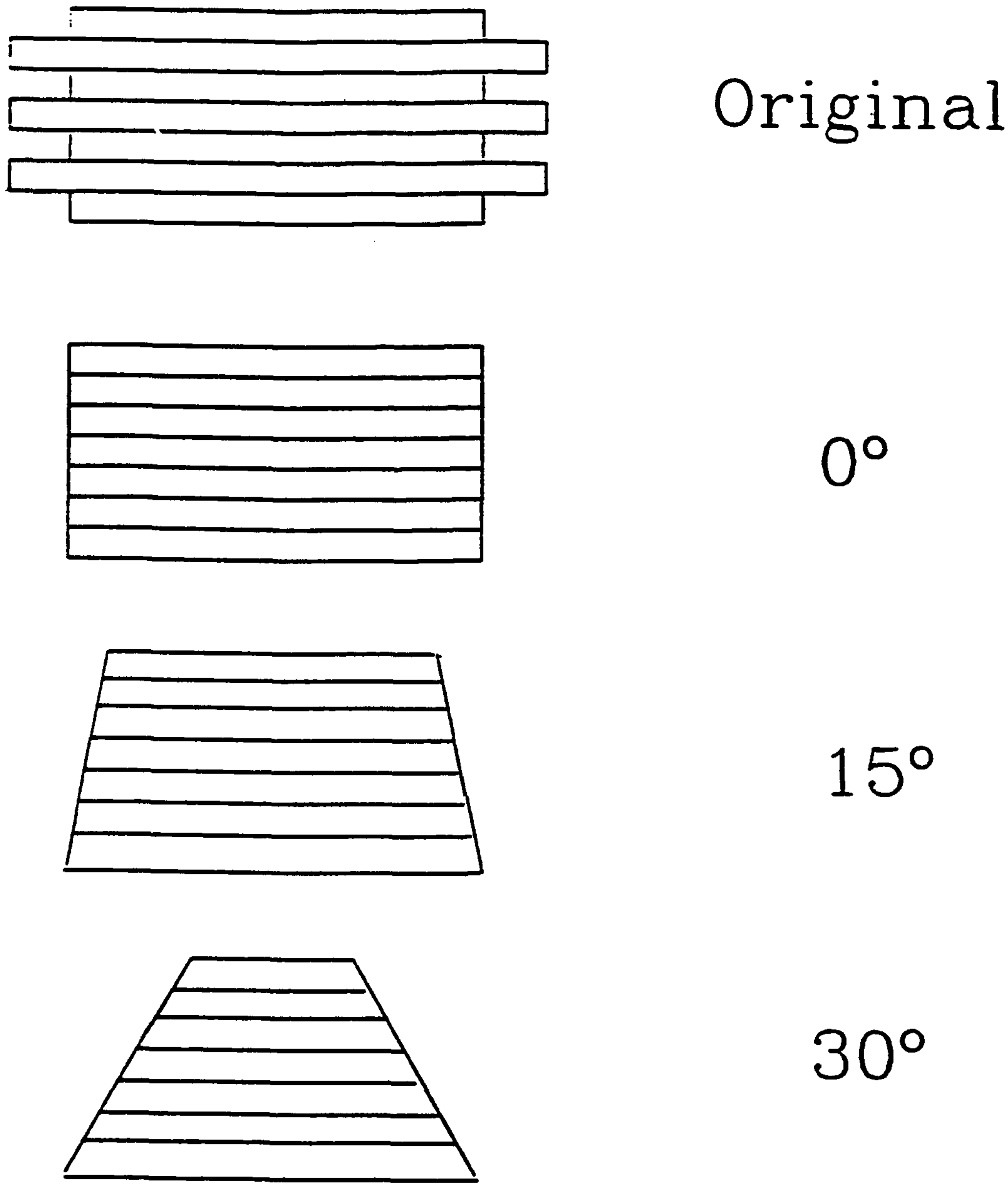

Figure 37. Angular dependence of the microstack with surfaces machined to different angles.

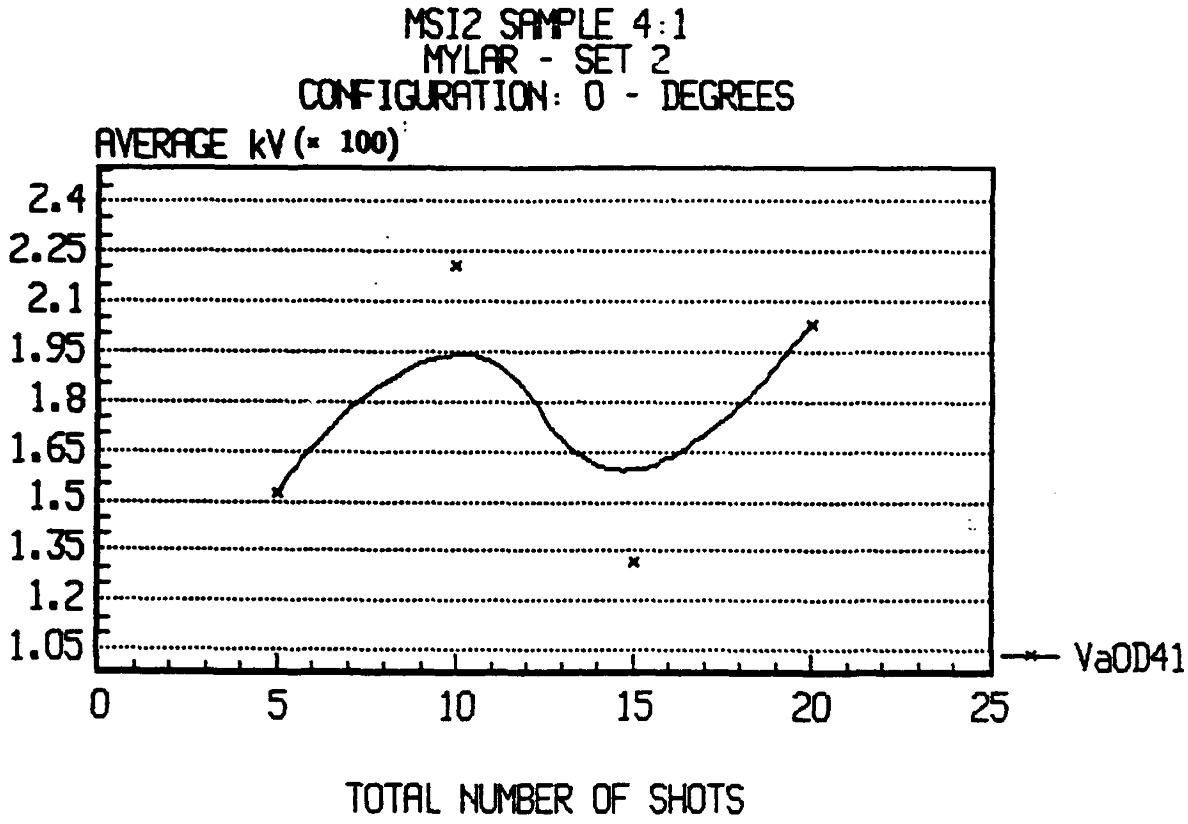

Figure 38. 4:1 sample tested at 0° with the metal and dielectric wafers leveled to the surface. The low value after 15 shots is probably due to surface damage, the last 5 shots showed consecutive flashing.

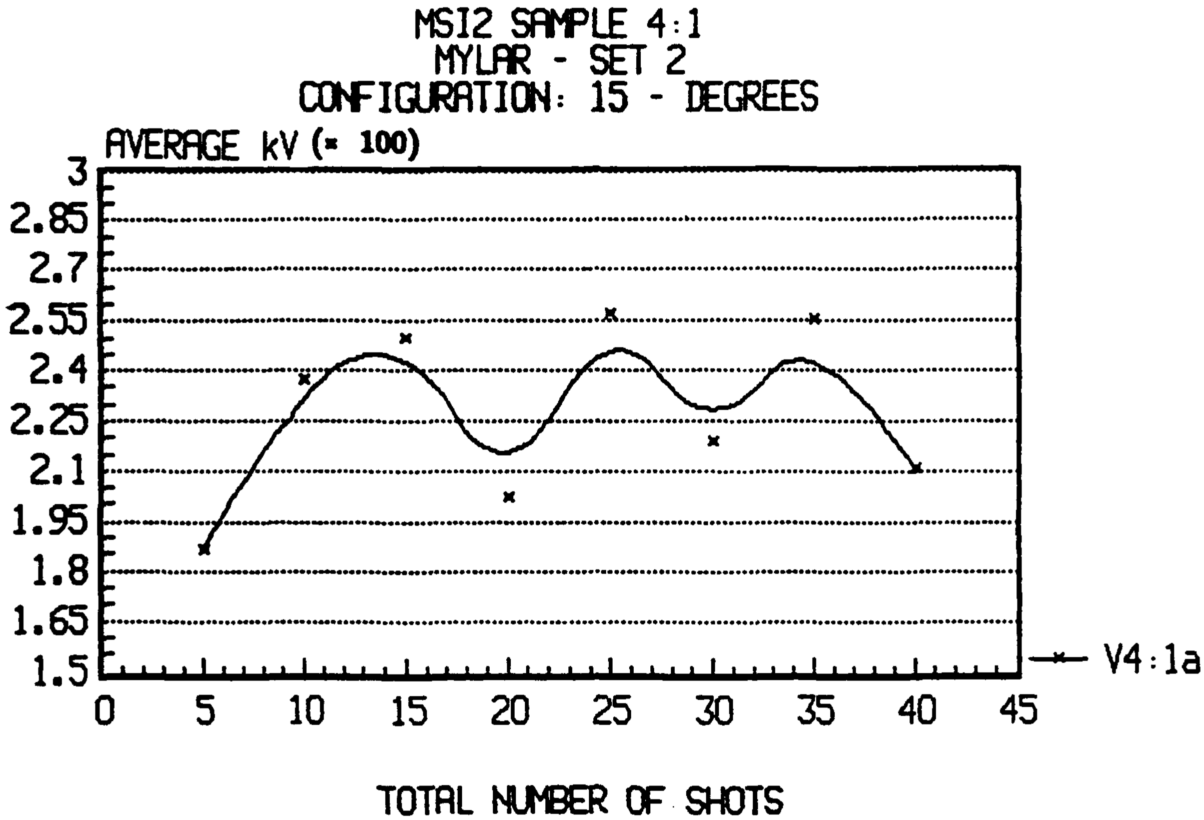

Figure 39. 4:1 sample tested at 15°, the low points are consecutive flash–events.

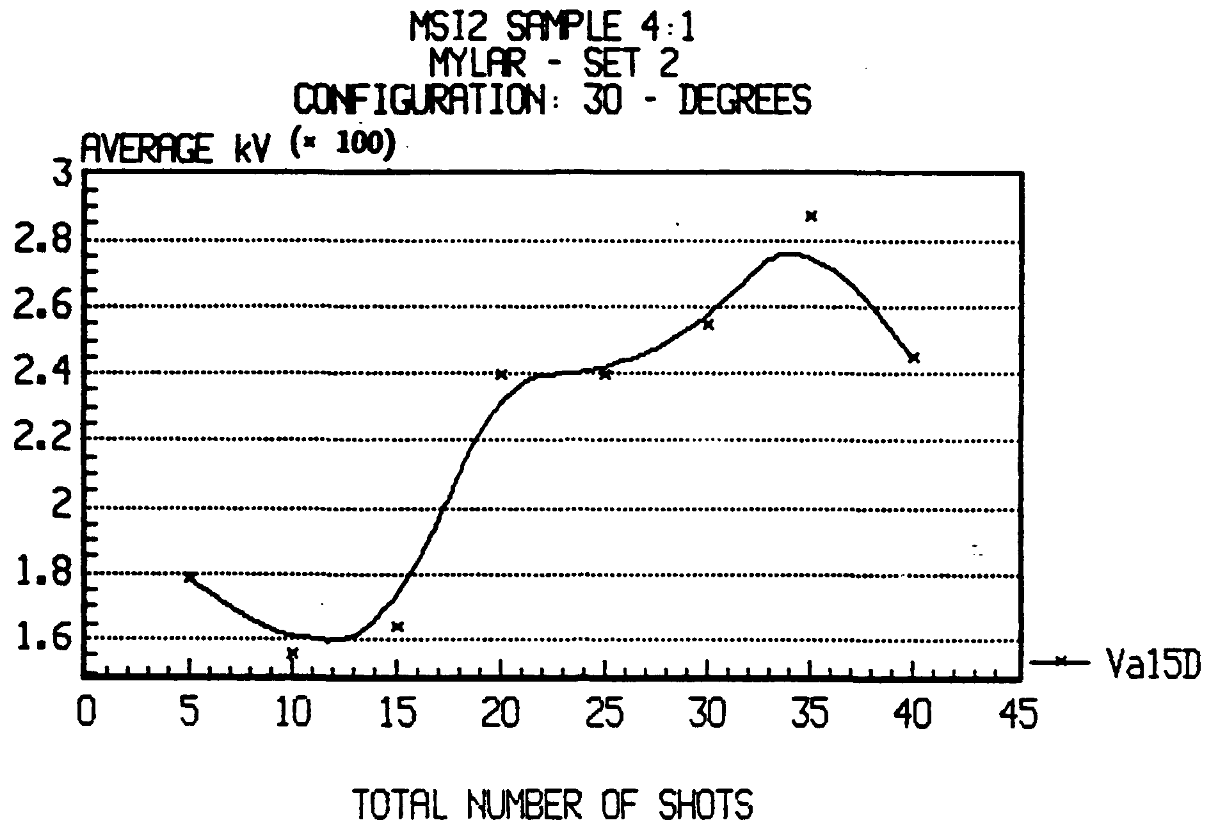

Figure 40. 4:1 sample tested at 30° inclination. The sample showed heavy damage through the bulk after the last 5 shots.

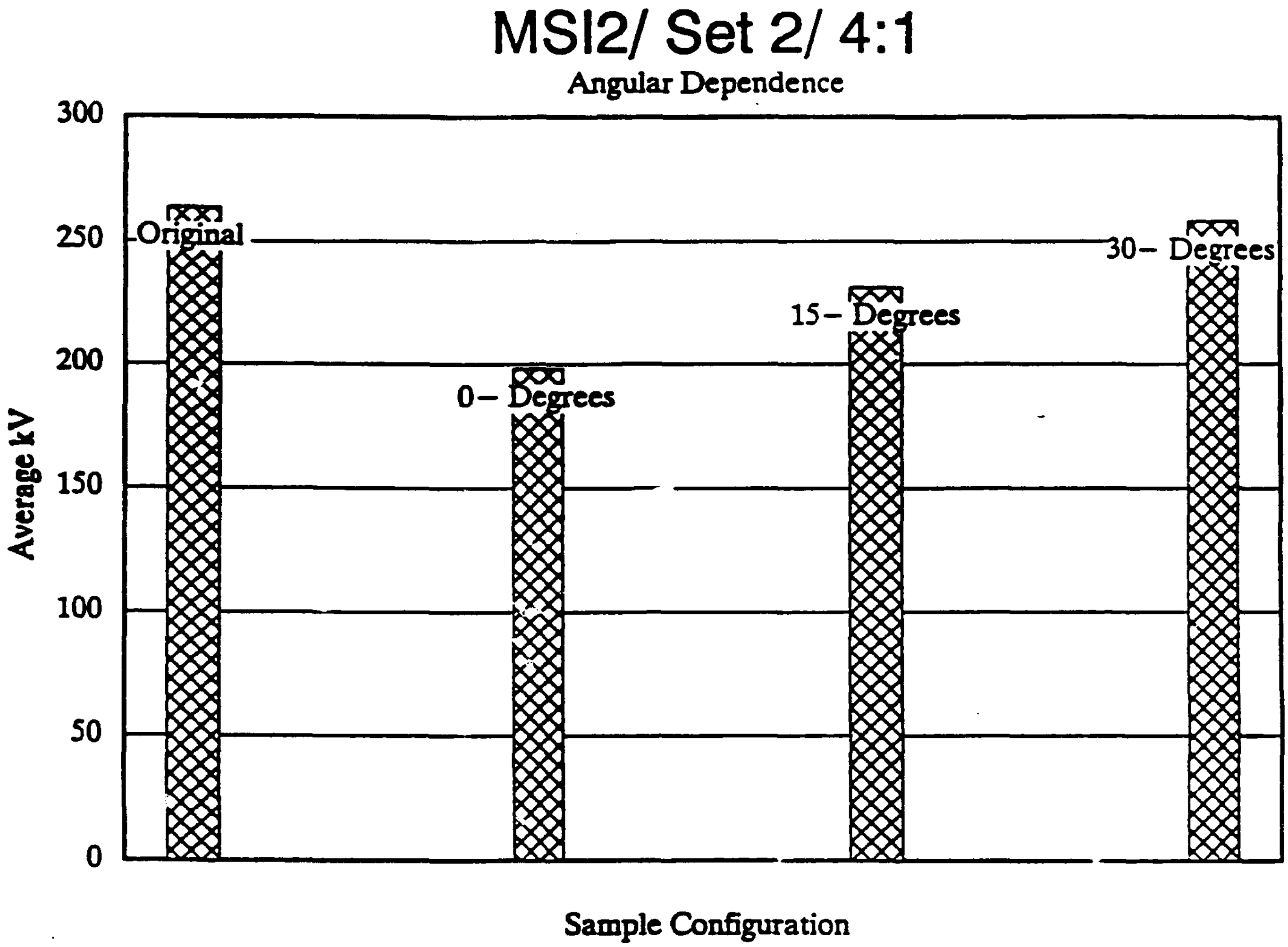

Figure 41. Behavior of the sample averaged voltage as the inclination is changed.

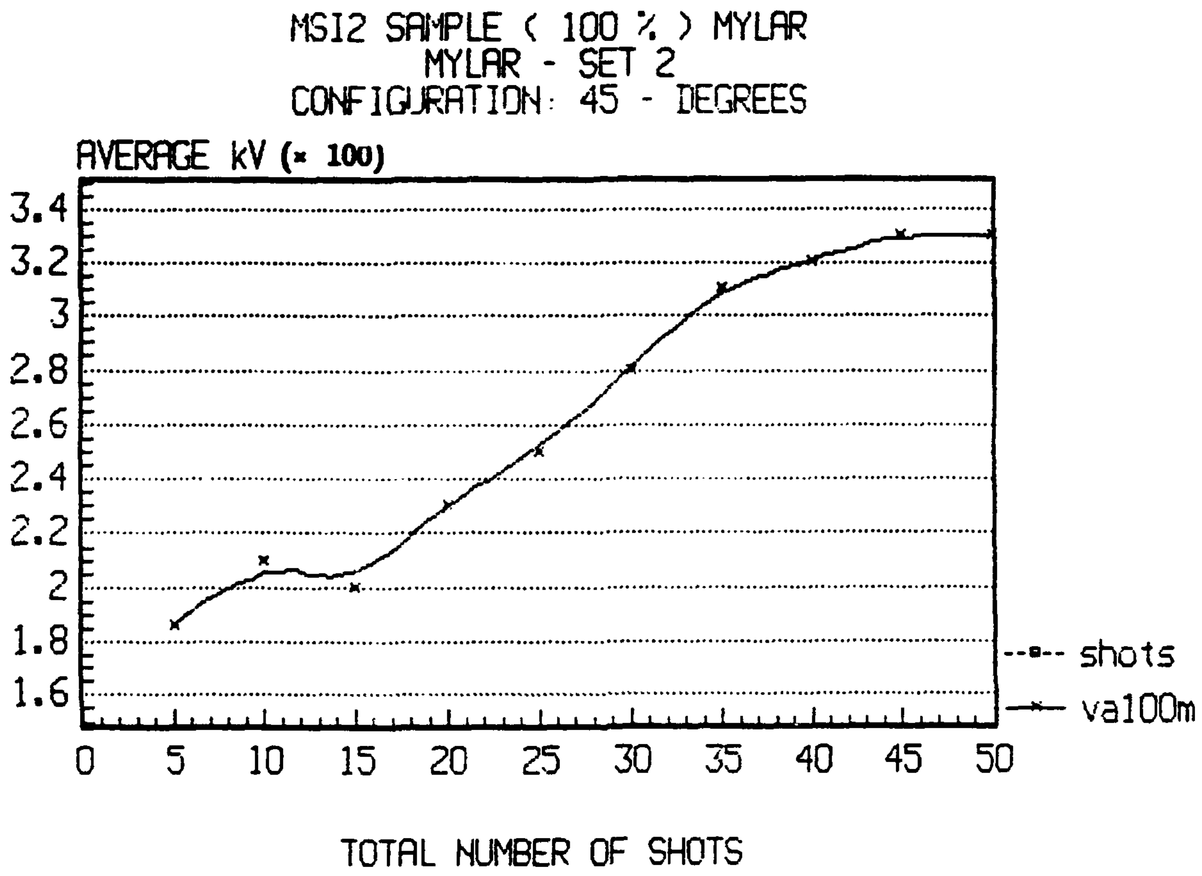

Figure 42. All Mylar stack machined to 45°, the sample failed through the bulk.

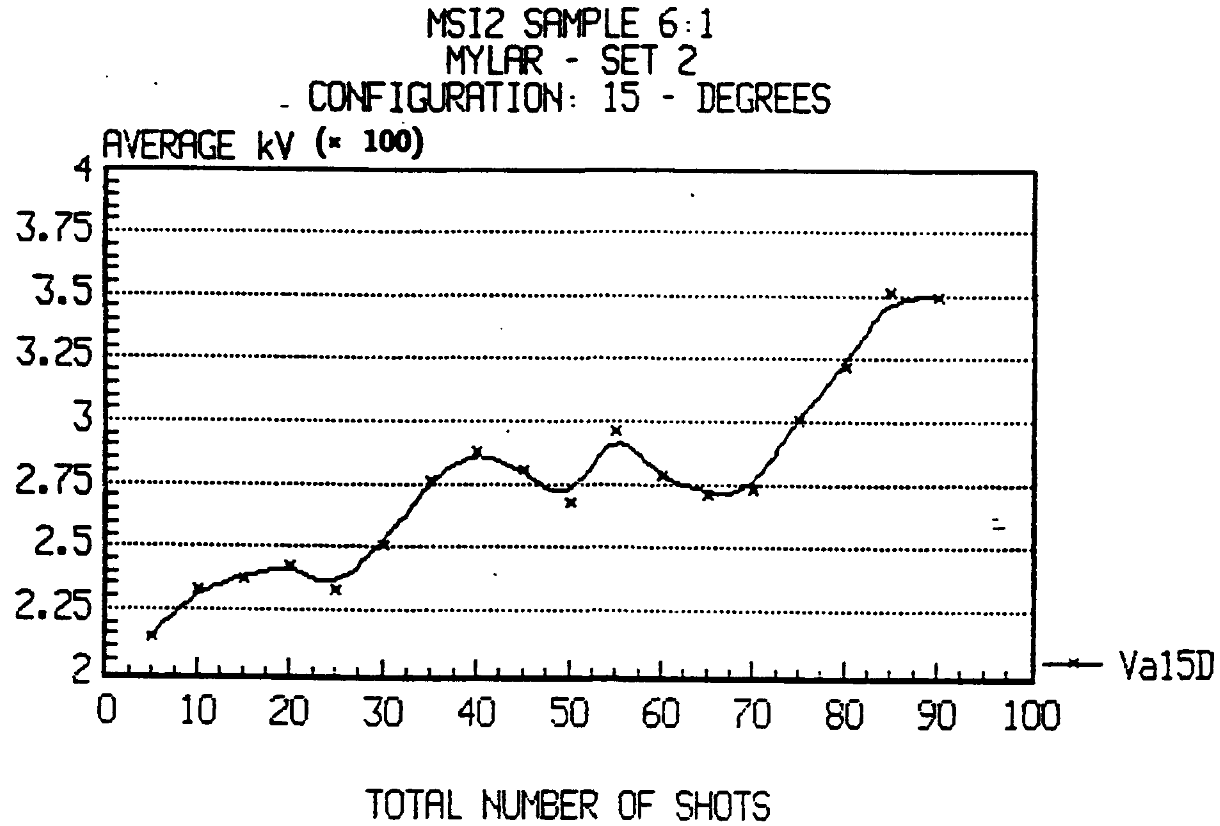

Figure 43. Mylar sample at a 6:1 ratio machined to a 15° inclination. Performance beyond 300 kV/cm is observed with no flashing.

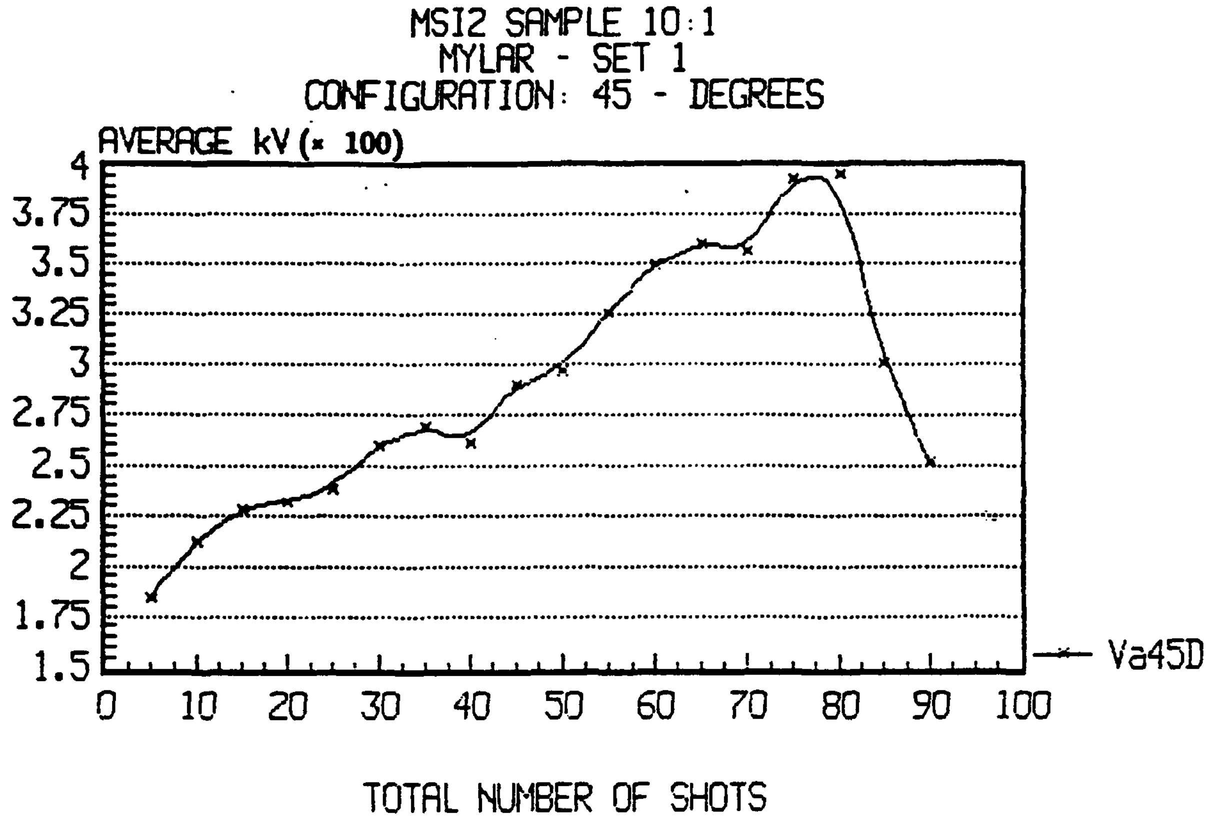

Figure 44. Mylar sample with a 10:1 ratio cut to 45° inclination. After tolerating an excess of 350 kV/cm the sample failed through the bulk.

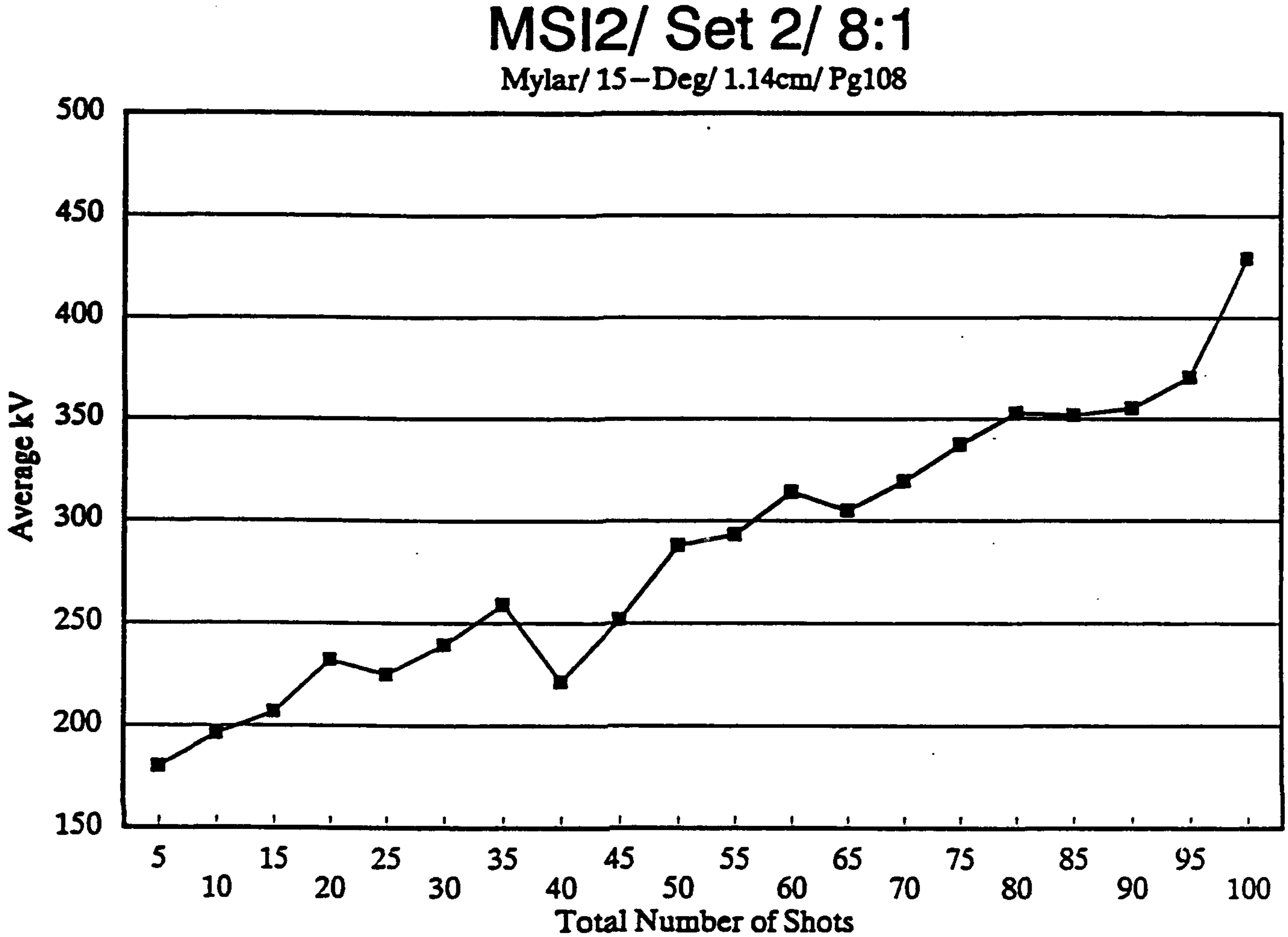

Figure 45. Mylar sample with an 8:1 ratio cut at 15°. The sample started flashing after the 450 kV voltage. Observed that the sample thickness is 1.14 cm which results in an effective field of 376 kV/cm.

SECTION 6
ANALYSIS OF RESULTS AND FINAL DESIGN

To investigate the apparent 350–400 kV/cm limitation, we performed a series of tests to measure the electron emission from the surface of the electrodes. This value has been indicated before as the point where anode dominated processes start (Ref. 15). The mechanism for flashover that uses surface initiated avalanches due to electron bombardment, is assumed to require considerable electron emission from the electrode surfaces. The test was done by removing the sample and testing a 1 cm vacuum gap between the electrodes. Stable discharges were observed up to 300–350 kV/cm, after that value, flashes, partial and full arcs were observed.

Figure 46 shows the current density measured through the 1 cm vacuum gap formed by the two electrodes. As shown in the figure, the emission from the surface grows in a parabolic function shape. To a first approximation this behavior is predicted by the field electron emission from metal surfaces. The current then is due to a combination of effects: Explosive emission and tunneling, both effects included in the Fowler–Nordheim equation (Ref. 16):

$$J\left[\frac{A}{cm^2}\right] = 6.2\text{x}10^6 \, \frac{\left[\phi / E_F\right]^{1/2}}{\phi + E_F} \, E^2 \exp\left[-6.8\text{x}10^7 \frac{\phi^{3/2}}{E}\right]$$

where:

- J: Current Density [A/cm²]
- ϕ: Material Work Function [eV]
- E_F: Material Fermi Energy [eV]
- E: Field Intensity [V/cm]

As can be seen to first order this can be approximated to a constant times the square of the field.

As can be observed in Figure 46, the measured current density after a field of 300 kV/cm is in excess of 10 $\left[{}^{A}/{cm^2}\right]$. At that level of emission the insulator best performance is given by its property of not affecting the current distribution. If the current is constricted or perturbed by any means, a flashover will occur. To avoid the effect of all this current emitted from the electrode surface we attempted to test the samples in the configuration shown in Figure 47. Using this configuration we experience problems with the electrodes contact to the sample surface. The first flash event destroyed the two immediate layers of the sample adjacent to the electrode.

A special set of samples was fabricated based on the previous results. The configuration is shown in Figure 48, the dielectric is cut at 45° and the metal wafer diameter is kept constant. Two sets of samples were fabricated using Mylar and Kapton as base materials.

The Mylar set consisted of three samples with a thickness ratio of 4:1, 5:1, and 6:1. The results are very impressive:

Mylar 4:1	354 kV
Mylar 5:1	495 kV

These are peak values obtained with 50 μs long pulses, but they reflect the behavior established before with shielded 45° samples. Figure 49 shows the per shot statistics of the 5:1 sample with Figure 50 showing the comparisons between the two samples.

The Kapton samples averaged values at the gap's breakdown voltage. The Kapton sample matrix consisted of 3 samples with the same thickness ratio as the mylar samples: 4:1, 5:1, and 6:1. The results are as follows:

Kapton 4:1	358 kV	(8:1)	4
Kapton 5:1	361 kV	(10:1)	5
Kapton 6:1	450 kV	(6:1)	3

These are also peak values obtained with 50 nsec long pulses. The 5:1 Mylar and the 6:1 ratio samples show the best results as Figure 51 indicates the averaged values are all better than 300 kV/cm. Figure 52 shows the statistics for the last

15 pulses on the 6:1 sample. It can be observed that the mean expected value is at 360 kV/cm.

The behavior with respect to pulse length can be inferred by comparing Figure 53, which shows the two sigma pulse length for the three samples. As can be observed, the highest fields are obtained with the average shortest pulse width, but in general the pulses were changed from 30 to 50 nsec FWHM. When the voltage is correlated with the pulse width the plots in Figure 54 show again the improved behavior as the pulse width gets shorter. The power equations are:

$$F_6 = 10.85 * t^{-0.2689}$$
$$F_{10} = 7.67 * t^{-0.2194}$$

normalized to MV/cm yields:

$$F_6 = 0.9765 * t^{-0.2689}$$
$$F_{10} = 0.69 * t^{-0.2194}$$

The time dependence shown above, is very close in value to that predicted by Martin's equation. The difference between the two constants may include the effect introduced by the ratio of thickness. Figure 55 shows the combined power regression equation for all the data from the three data sets. The equation:(normalized to MV/cm)

$$F_{6,8,10} = 1.007 * t^{-.3155}$$

yields a time dependence closer to $t^{1/3}$ which is the trend on the two individual previous sets. The difference in the constants can be accounted for by the following:

$$\frac{F_6}{F_{10}} = 1.41$$

assuming the same time dependence. The ratio between the layers is:

$$\frac{F_6}{F_{10}} = 1.66$$

Now, the ratio between the individual power fit and the overall:

$$\frac{F_{overall}}{F_{10}} = 1.45$$

The area dependence yields a factor of:

$$A^{1/10} = 1.24$$

Very close, so the best fit using the combined power fit yields (in the conservative side):

$$F\ t^{1/3}\ A^{1/10} \cong 1$$

where F: Field in MV/cm
t: In Nanoseconds
A: Lateral Area cm^2

This is valid for metal wafers in the 100 μm range in thickness and insulator dimensions between 500 and 1500 μm in stacks formed with dielectric wafer with the same thickness as the metal or smaller.

As an example, consider the need for 2 MV total voltage in 10 nsec pulses, with a bushing 10 cm long and 40 cm in diameter, first the field required per cm is:

$$F = \frac{2\,MV}{10\ cm} = 0.2\ MV/cm$$

Then the surface area per cm length

$$A = \pi\ (a+b)\ \ell$$

with a = 19 cm and b = 20 cm:

$$A = 122\ \text{cm}^2$$

The sample tolerates:

$$F = \frac{1}{(122)^{1/10}\ (10)^{1/3}} = 0.310\ \text{MV/cm}$$

The insulator fabricated as described will tolerate 310 kV/cm at 10 nsec.

These numbers are excellent considering that the fitted data corresponds to 1 failure out of 15 pulses. The scaling equation from J. C. Martin is used for a 50% probability of failure. The scaling equation produced by the microstack insulator comes from better than 10% (6.6%) probability of failure, or 94% reliability at the calculated voltage.

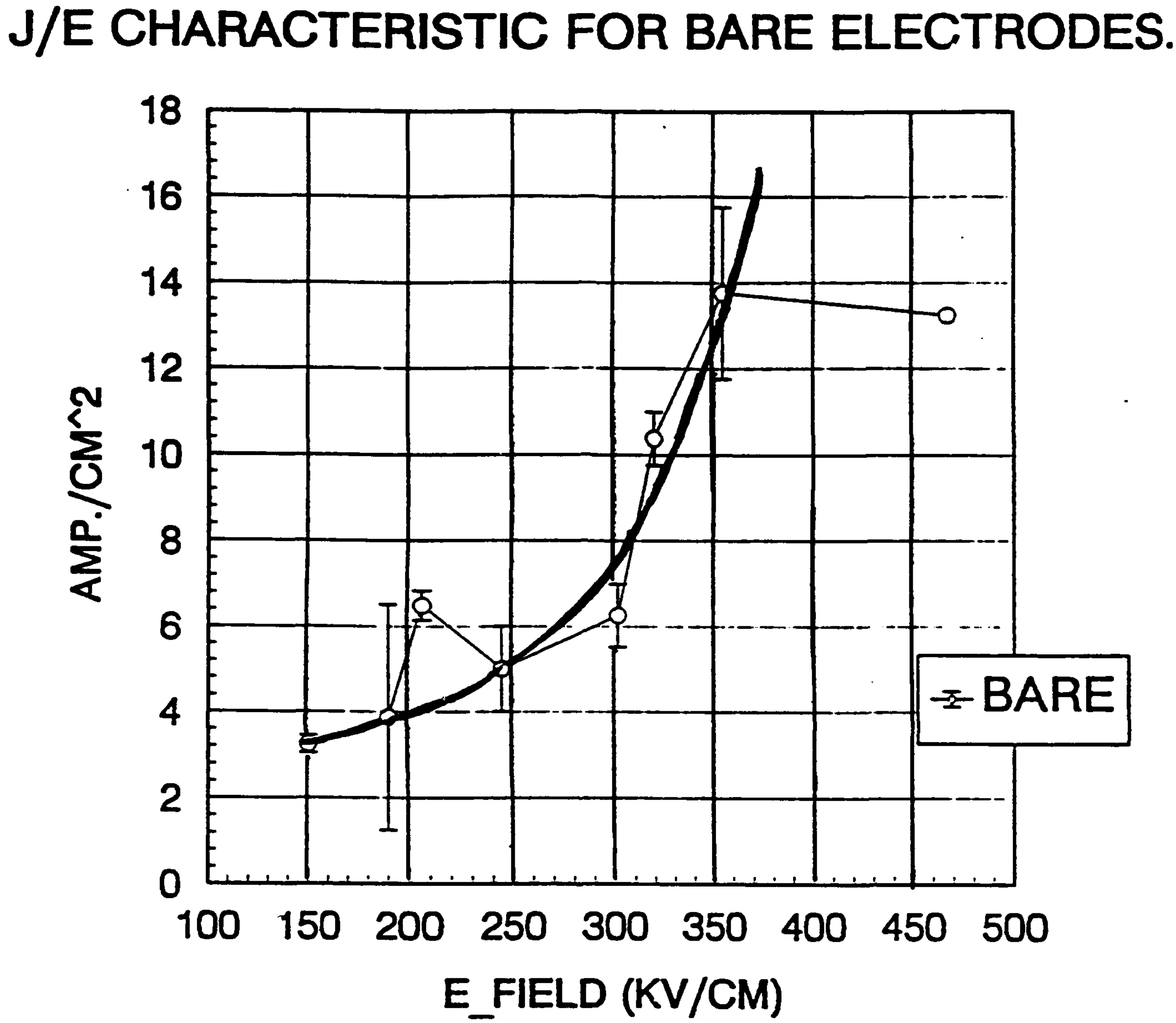

Figure 46. Current density through the 1 cm vacuum gap formed by the two electrodes used to test the samples. Data is taken with no sample in between and pulse lengths of 100 nsec.

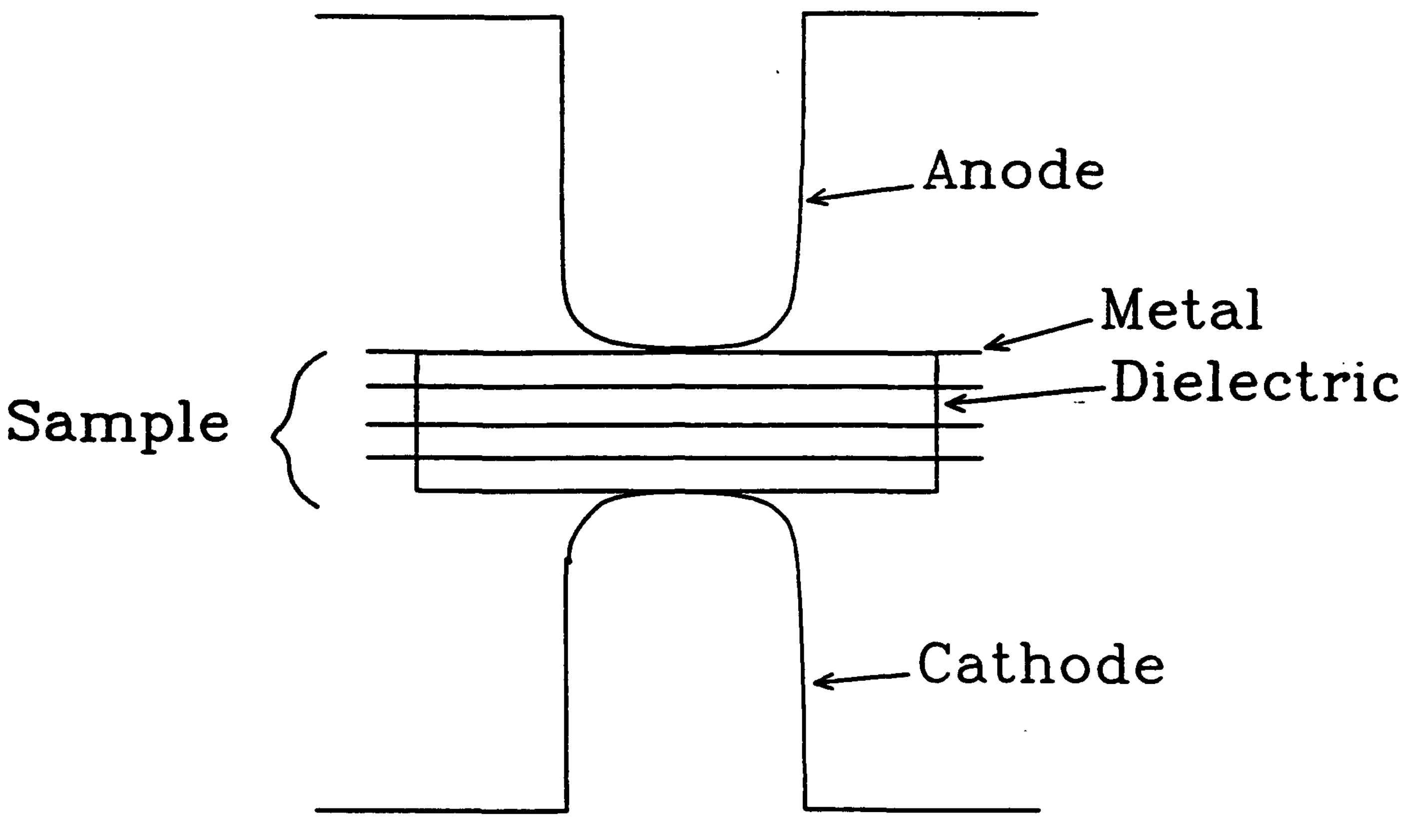

Figure 47. Experimental setup for testing surface flashover without emission from the electrode surface.

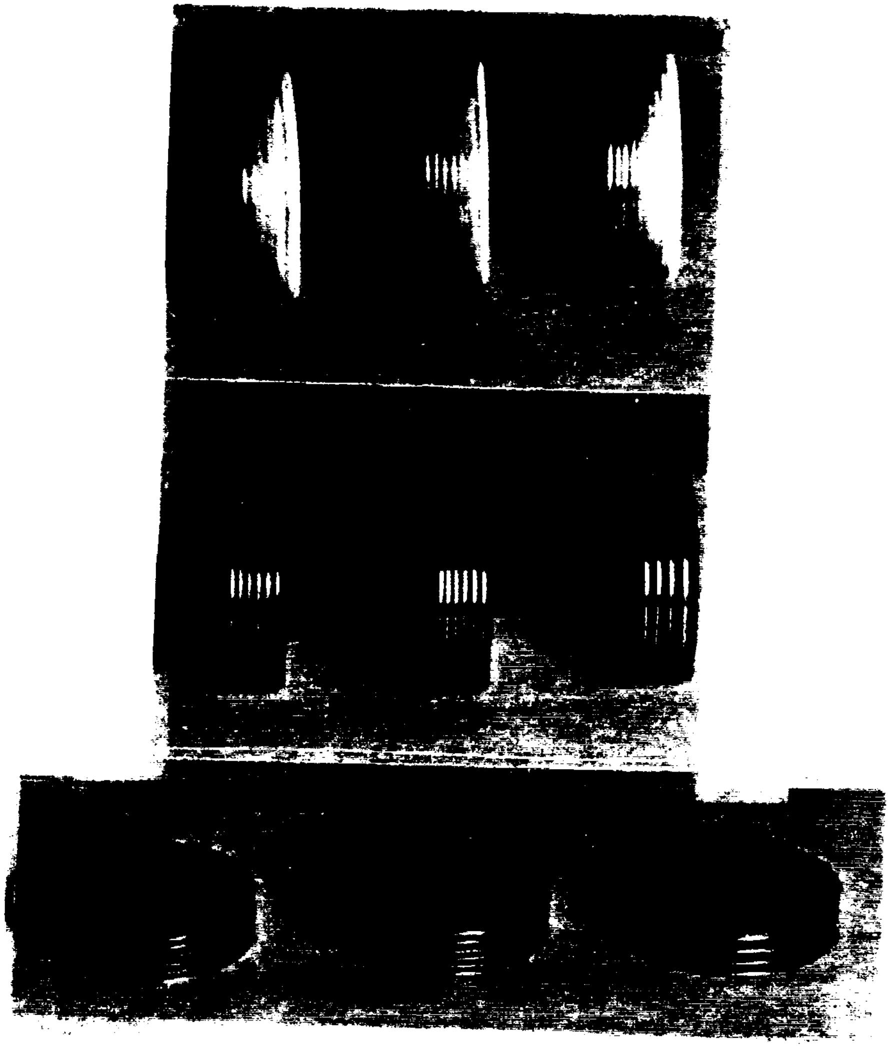

Figure 48. Special samples with 45° dielectric stacked within the metal wafers.

HISTOGRAM OF SAMPLE 5:1 SPECIAL TEST
MYLAR – FINAL SAMPLE

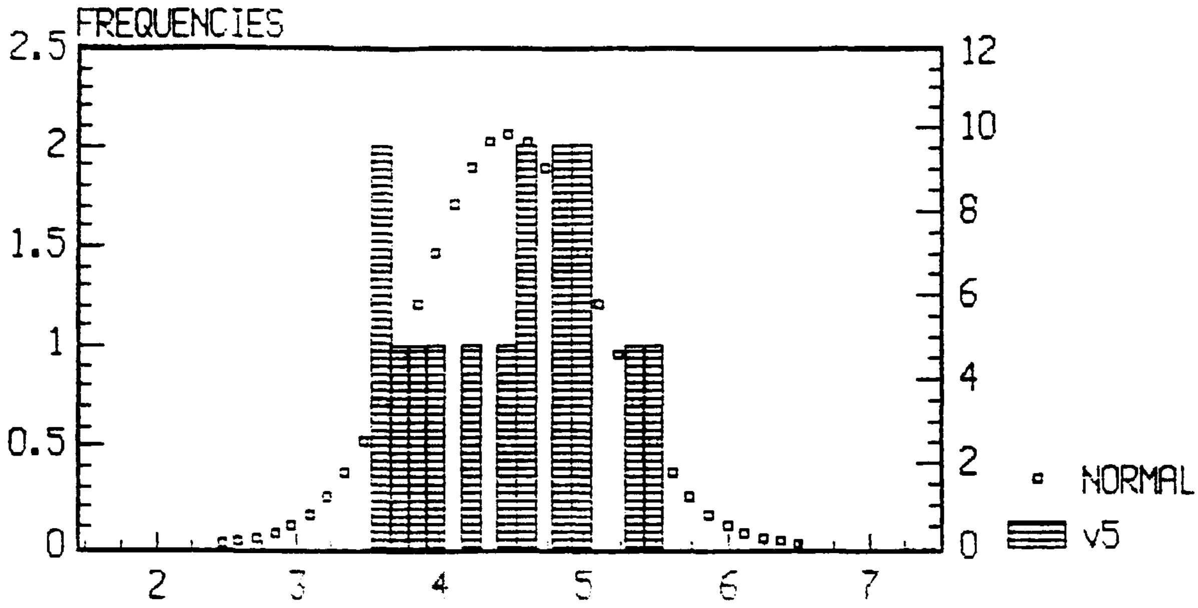

FIELD VALUES kV/cm
CALIBRATION FACTOR: VALUE X 90

Figure 49. Mylar 5:1 sample. Histogram showing the normal distribution around the mean value. As shown before, this sample achieved 495 kV/cm. Peak voltage with the mean value at 400 kV/cm.

The bottom figure shows the sample configuration.

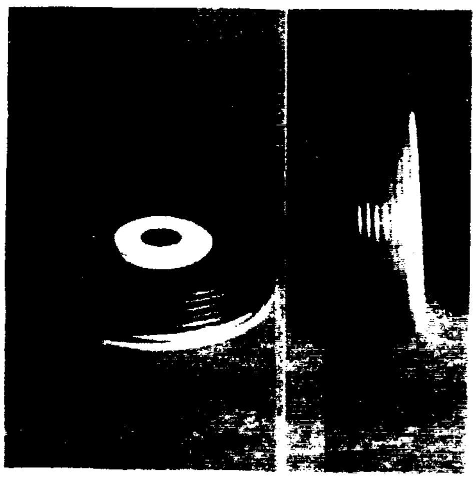

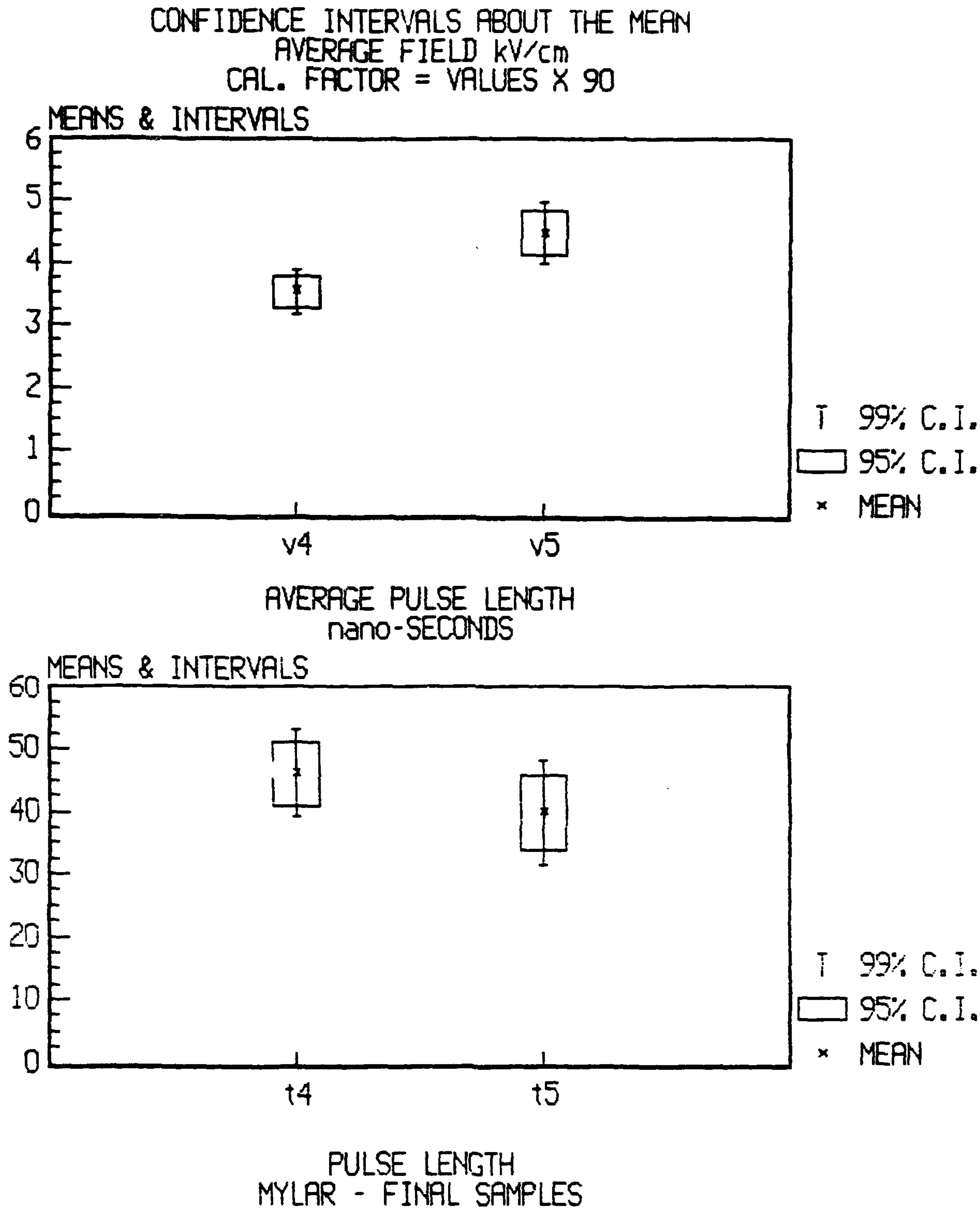

Figure 50. Mylar Samples 4:1 and 5:1. Top figure shows the averaged field values with the two sigma error bars. Bottom figure shows the averaged pulse length with the two sigma error bars. The trend of better averaged value with shorter averaged pulse length is evident.

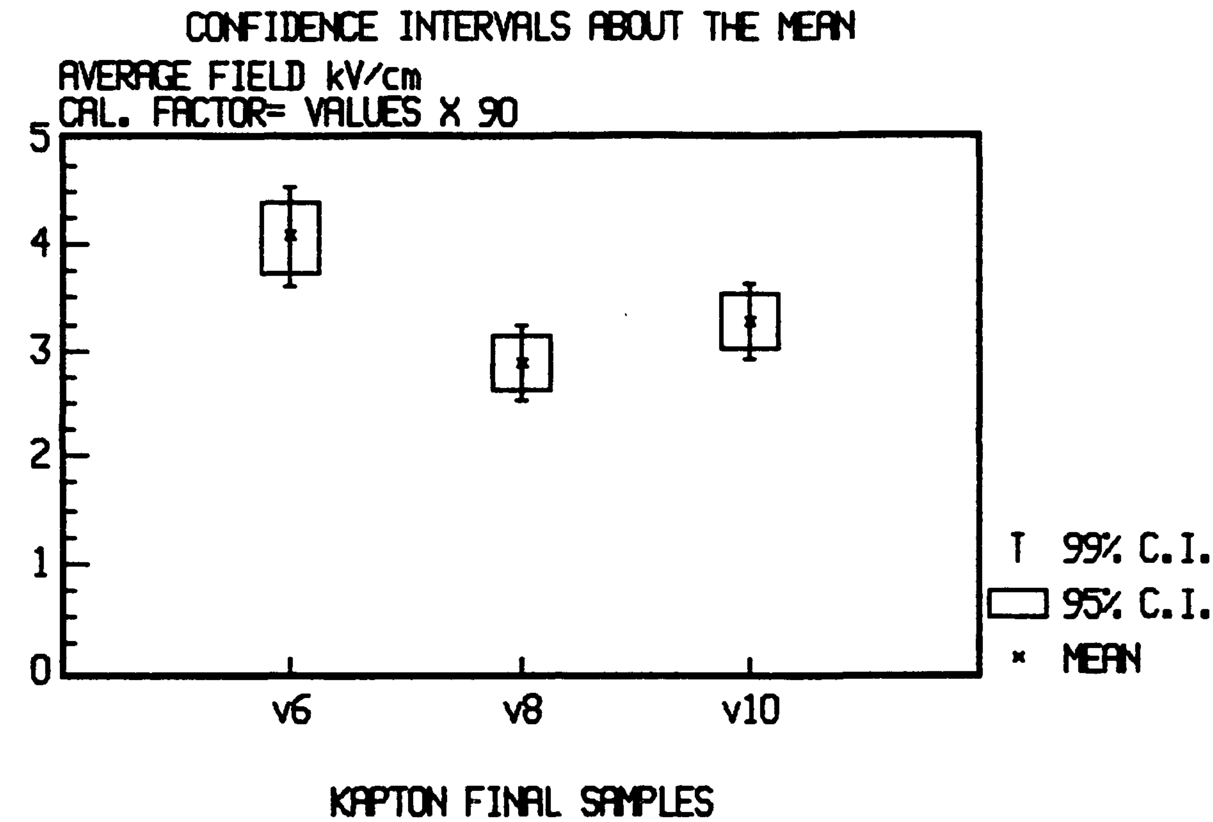

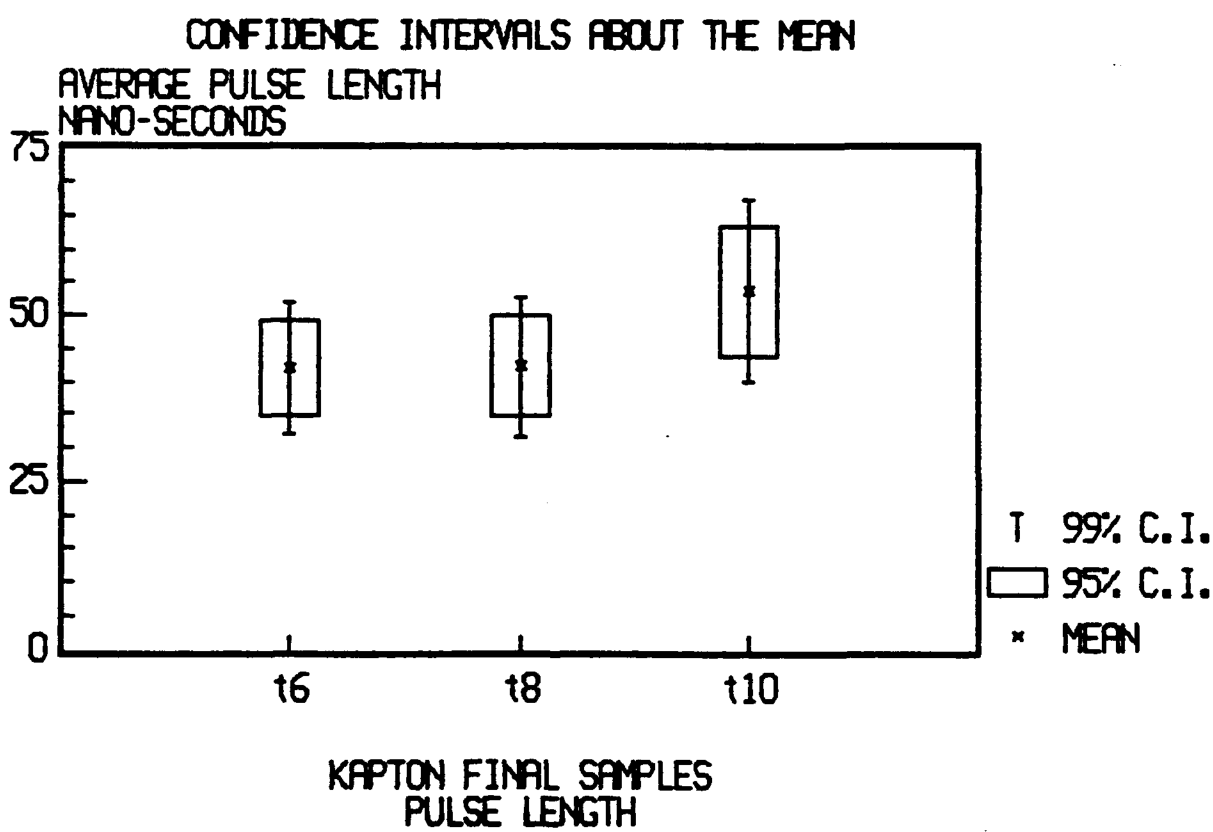

Figure 51. Averaged field values for the Kapton final samples 6:1, 8:1 and 10:1. Bottom figure shows averaged pulse length.

HISTOGRAM OF SAMPLE 6:1 SPECIAL TEST
KAPTON FINAL SAMPLES

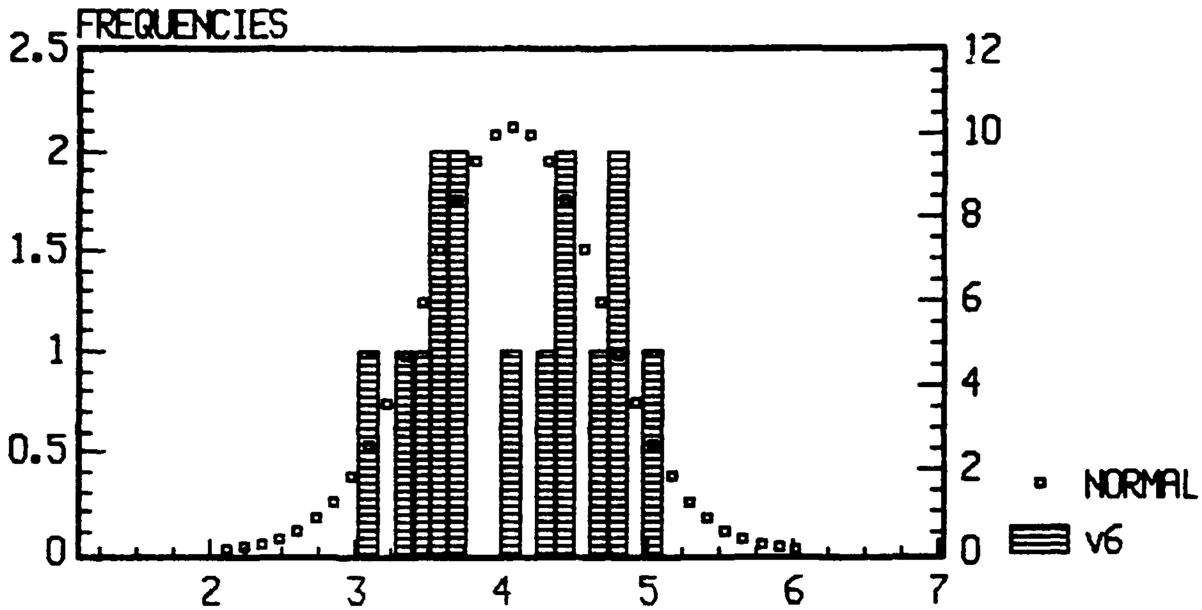

FIELD VALUES kV/cm
CALIBRATION FACTOR = X 90

Figure 52. Kapton 6:1 sample histogram showing the normal distribution around the mean value. As shown before, this sample achieved 450 kV peak values with a mean value at 360 kV/cm.

The bottom figure shows the sample configuration.

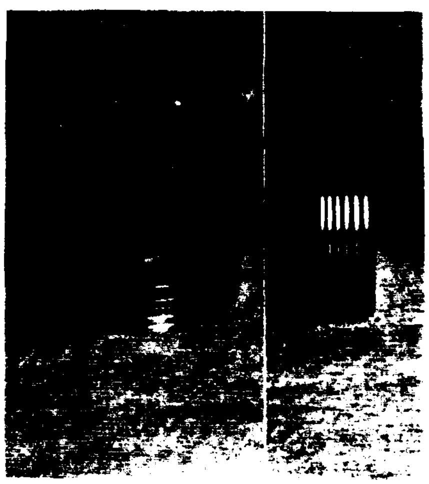

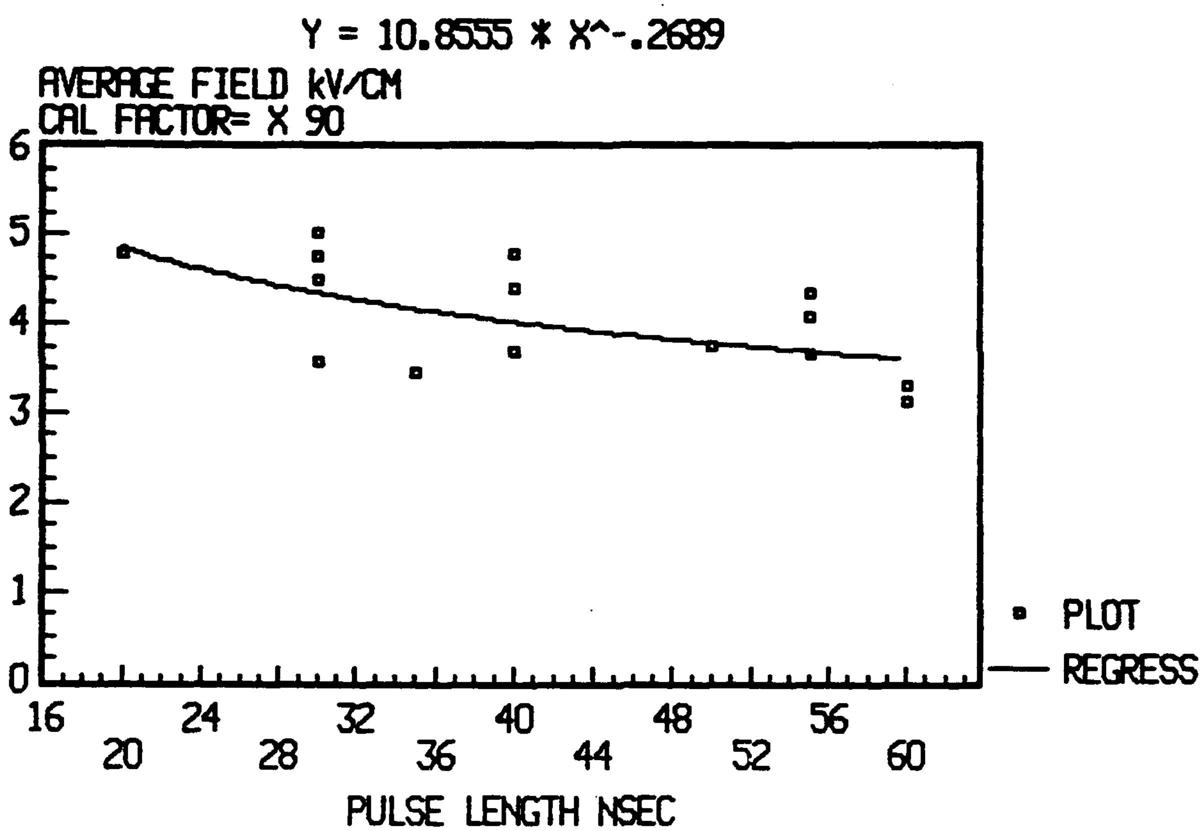

Figure 53. Power fit of data from Kapton sample 6:1. The predicted trend of higher fields at shorter pulse lengths is evident.

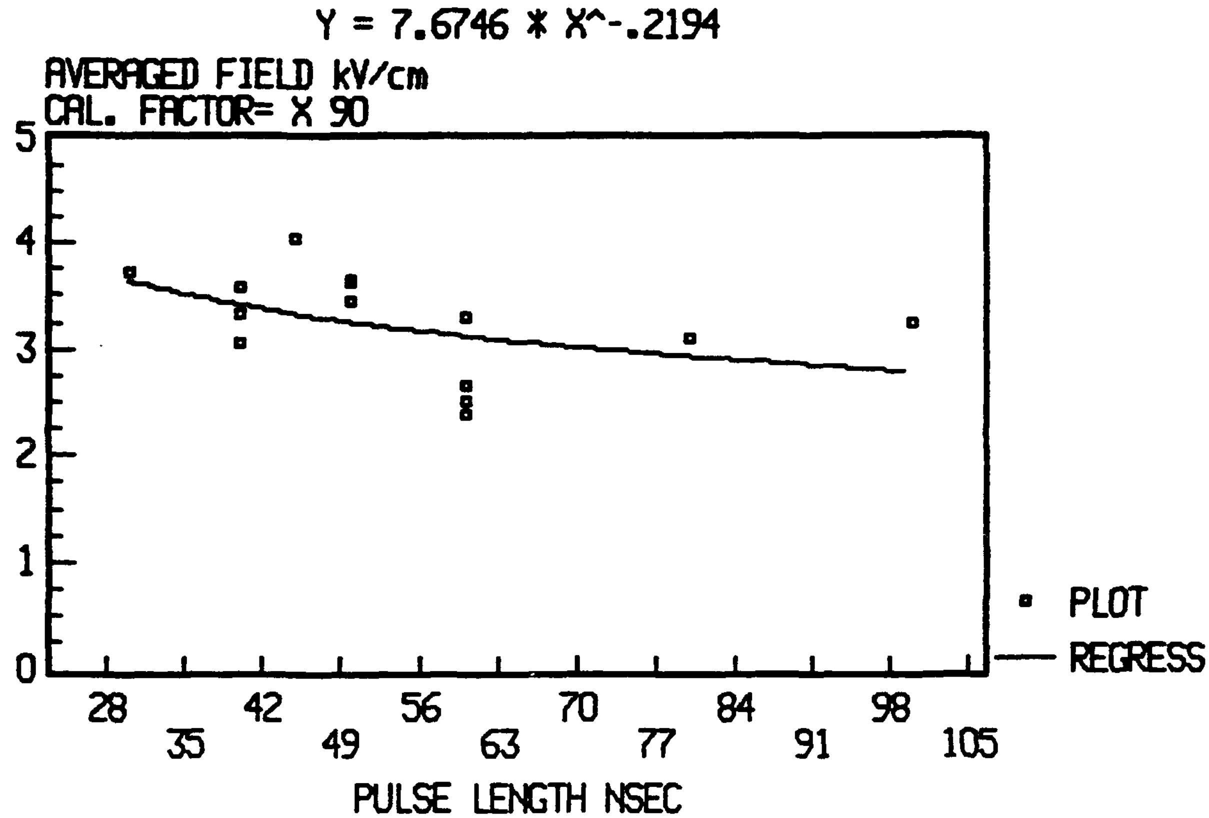

Figure 54. Power fit of data from Kapton sample 10:1. The predicted trend of higher fields at shorter pulse length is evident.

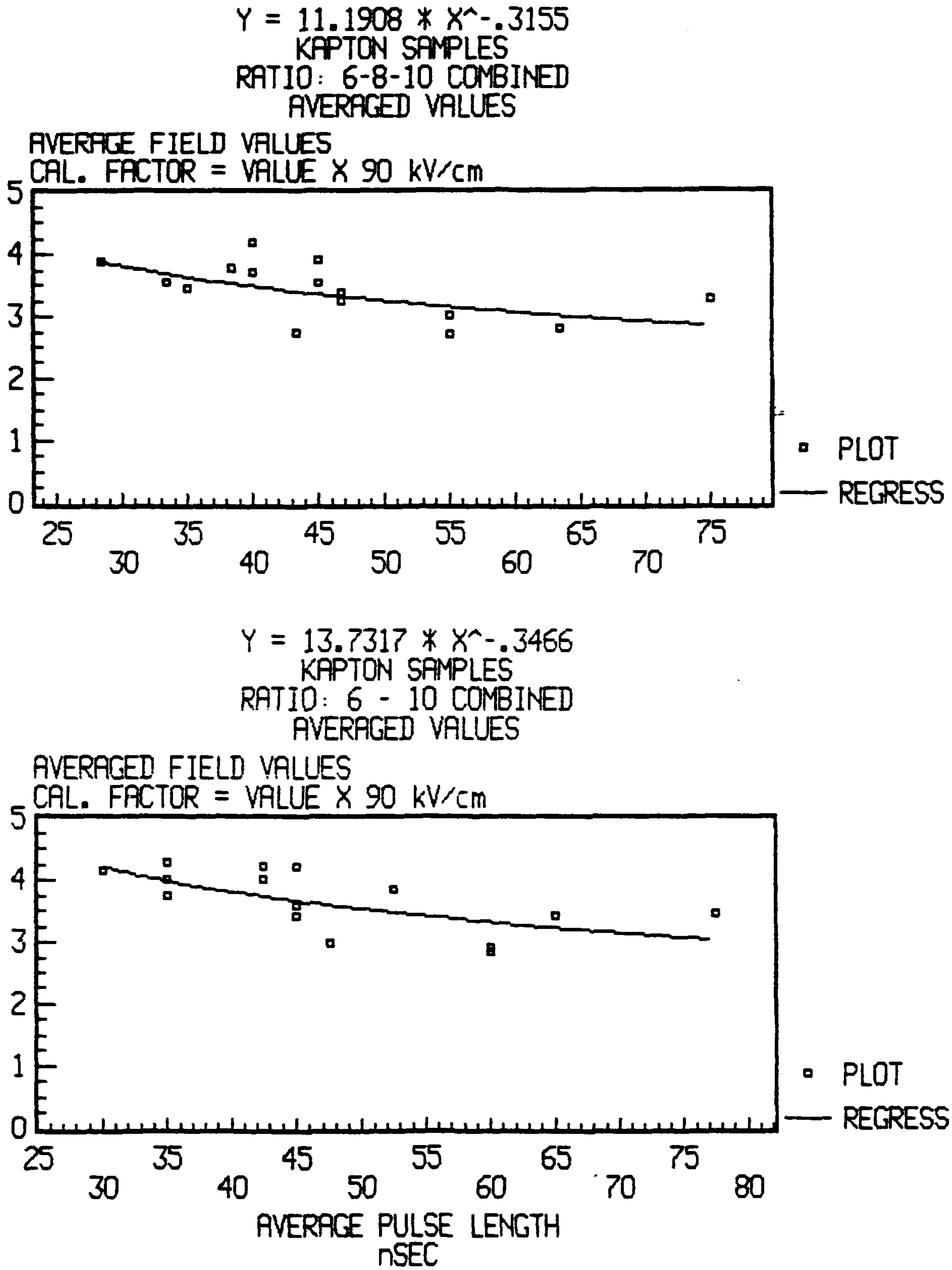

Figure 55. Power fit for the three Kapton sample series combined (top), and power fit for the 6 and 10 samples only (bottom).

SECTION 7
CONCLUSIONS AND RECOMMENDATIONS

The program achieved results that represent a breakthrough in vacuum surface flashover insulation. The samples designed as the optimum configuration failed through the dielectric bulk before surface flashover was observed. In fact the ultimate limitation is the vacuum breakdown of the anode–cathode electrode system. We determined that for 100 nsec long pulses the vacuum breakdown voltage of the electrode system was above 350 kV/cm, with some pulses as high as 450 kV/cm. Typical microstacks will sustain voltages above 280 kV/cm, with optimized samples failing typically at average fields above 400 kV/cm and not because of surface flashover but by a failure through the bulk of the sample.

The empirical fit formula for each section of the insulator does not differ much from Martin's equation. Martin's empirical formula may not apply for pulses below 100 nsec or even under 500 nsec long. The time correction found during this program seems to fit very consistently. Particular attention was paid to keep the surface area as constant as possible to allow for a power fit. Weibull statistics were carried out, but since the area is kept constant, the power fit was considered more reliable.

It should also be noted that the power fit equation was arrived at using averaged data which resulted in a conservative estimate on the calculated field. This introduces a safety factor in the probability of failure. The probability of failure is 1 in 15 which is 40% better than using Martin's approach.

The microstack opens the possibility of a new kind of compact linear accelerator. Linear accelerator cavities with dielectric walls have the disadvantage of low gradients, due to surface flashovers. Gradients of 20 MV/M can be obtained with the microstack, with a 50% safety margin as shown at the end of Chapter 6. Such a change in scale size can be compared to the replacement of vacuum tubes by integrated circuits. Typical accelerating gradients of existing induction accelerators range from 0.2 to 0.8 MV/M. This new induction technology promises accelerating gradients of a least 20 times the present levels which open a large array of applications. These gradients are competitive with those of the best RF accelerators. However, the usable beam currents available with induction technology greatly surpass those of RF accelerators.

High voltage multi–megampere beam simulation machines could benefit from lower inductance in the implosion chamber. The present penalty of 20 KJ of X–ray extraction per Nano Henry is an example of how critical an efficient bushing is. The microstack may double the voltage capacity of the bushing with an added economy of being able to sustain multiple flashovers before effecting the performance of the bushing.

The use of this technology in microwave windows promises to at least double the power output. Figure 56 shows conceptually a Klystron cavity fed by two (maybe 8) dielectric wall accelerator injectors. Power extraction in the 10^9 Watts or 10^3 Joule energies are possible in such compact arrangement. Research in these areas will fully develop the technology and open the applications to accelerators and microwave hardware.

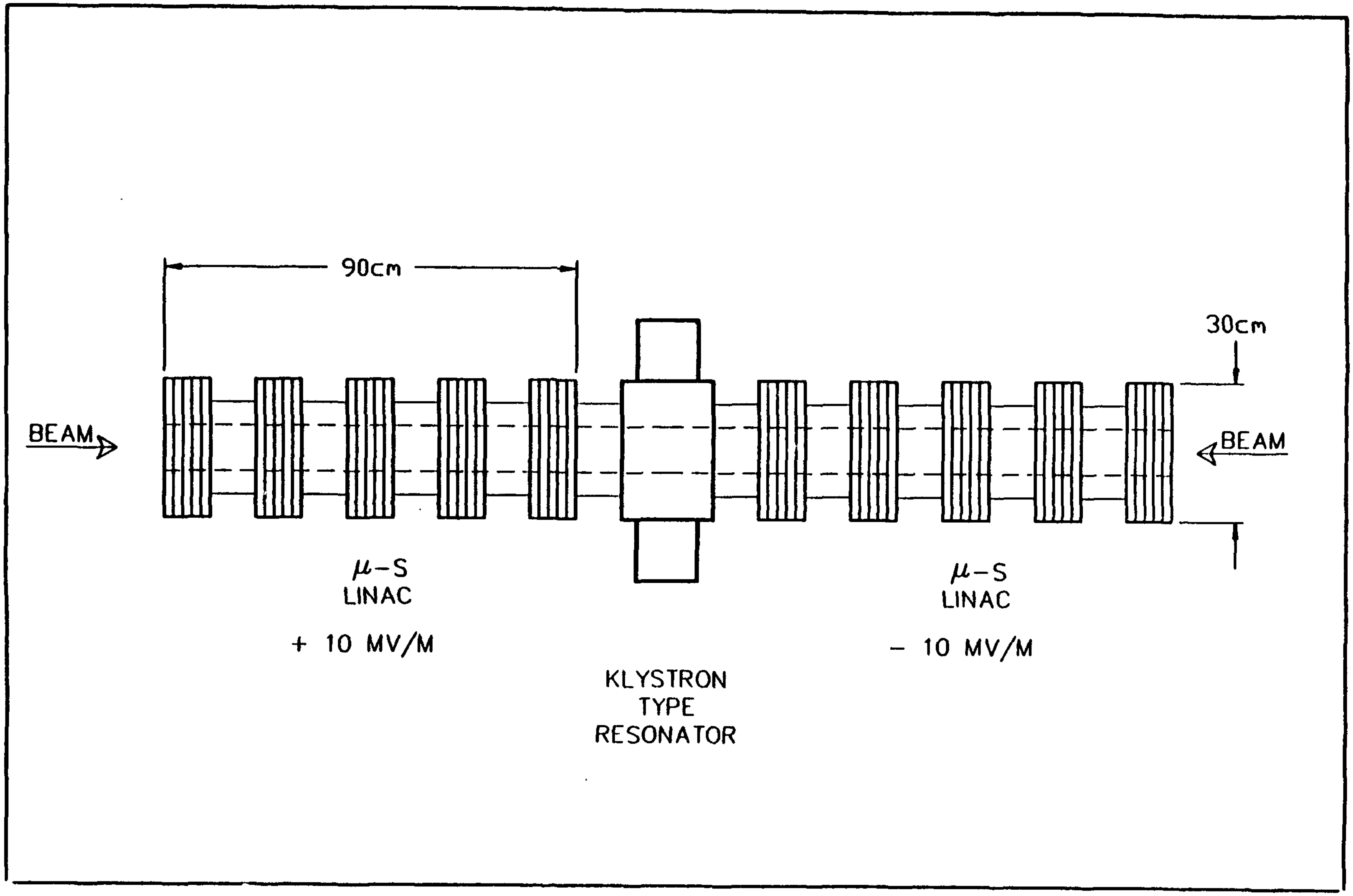

Figure 56. **Compact electron injection system for a high power Klystron microwave source.**

SECTION 8
LIST OF REFERENCES

1. Watson, Alan, "Pulsed Flashover in Vacuum", J. Appl. Physics, Vol. 38, No. 5, pp. 2019 – 2023, December 1966.
2. Anderson, R.A., and Tucker, W., J. Appl. Physics, Vol 58, pp. 3346, 1986.
3. Anderson, R.A., Brainard, J.P., "Mechanisms of Pulsed Surface Flashover Involving Electron Stimulated Desorption", J. Appl. Physics, Vol. 51, pp. 1414 – 1421, May 1980.
4. Anderson, R.A., "1978 Annual Report of the Conference on Electrical Insulator and Dielectric Phenomena", (CEIDP), National Academy of Science, 173, 1979.
5. Vigouroux, J.P., Lee–Deacon, O., LeGressus, C., Juret, C. and Boizaux, C., IEEE Transactions Elect. Insulator, EI18, 287, 1983.
6. Tourreil, C.H., Srivastava, K.D., Woelke, U.J., "Experimental Observation of Surface Charging of High–Voltage Insulators for Vacuum Apparatus", IEEE Transactions of Electrical Insulation, Vol. EI–7, December 1972, 176 – 179.
7. Avdienko, A.A., & Malev, M.D., "Surface Breakdown of Solid Dielectrics in Vacuum II Mechanism for Surface Breakdown", Soviet Physics Technical Physics, Vol. 22, August 1977, pp. 986 – 991.
8. Bugaev, S.P., Iskol'dskii, A.M., & Mesyats, G.A., "Investigation of the Pulsed Breakdown Mechanism at the Surface of a Dielectric Vacuum I Uniform Field", Soviet Physics – Technical Physics, Vol. 12, April 1968, 1358 – 1362.
9. Meek, J.M., and Craggs, J.D., "Electrical Breakdown of Gases", New York: John Wiley and Sons, p. 140.
10. Anderson, R.A., & Brainard, J.P., "Insulator Surface Charging During Fast Pulsed Surface Flashover in Vacuum", 1977 Annual Report of the Conferences on Electrical Insulation and Dielectric Phenomena, pp. 128 – 135. 1979.
11. Jensen, D., & Brainard, J. P., "Initiation of Electron Avalanches on an Alumina Insulator by an Electron Beam", IEEE Conference on Electrical Insulation and Dielectric Phenomena, pp. 250 – 257, 1973.
12. Gray, Eoin W., "Vacuum Surface Flashover: A High Pressure Phenomenon", J. Appl. Physics, Vol. 58, p. 3346, 1985.

13. Rodríguez, A.E., Morgan, W.L., Touryan, K.J., Moeny, W.M., & Martin, T.H., "An Air Breakdown Kinetic Model", submitted to JAP, 1991.
14. "PYROLUX" free standing acrylic adhesive from the DuPont Company.
15. Smith, I.D., "Pulse Breakdown of Insulator Surfaces in Poor Vacuum", Proceedings of the International Symposium on Insulation and High Voltages in Vacuum, pp. 261 – 280, 1964.
16. Langmuir, I., and Bloodgett, K.B., "Currents Limited by Space Charge Between 'Concentric Spheres'", Phys. Rev., Vol, 24, Ser. 2, p. 49, July – Dec., 1924.
17. Pillai, A.S. and Hackam, R., "Surface Flashover of Solid Dielectric in Vacuum", J. Appl. Physics, Vol. 53, Ser. 4, p. 2983 – 2984, April 1982.
18. Sudarshan, T.S., Cross, J.D., and Srivastava, K.D., "Prebreakdown Processes Associated with Surface Flashover of Solid Insulators in Vacuum", IEEE Transactions on Electrical Insulation, Vol. EI–12, pp. 200 – 208, 1976.

APPENDIX A
MICROSTACK PARAMETERS

Derivations of the dielectric susceptibility X, polarization field Ep, net electric field F_{net}, total surface charge σ_T, interaction surface area S and the capacitance C for the microstack.

General Case

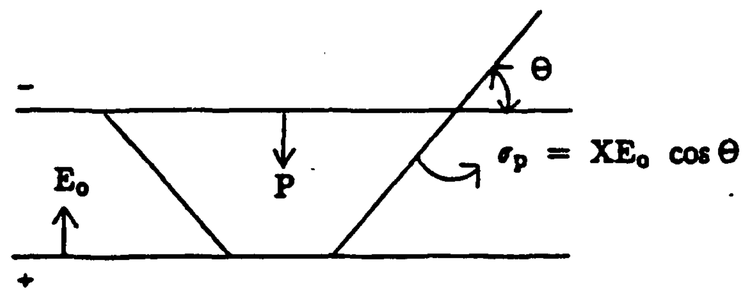

1. Problem: We want to derive the sum of the E–field due to the externally produced E_o as shown above, and the field due to the dielectric polarization, E_p.

Derivation:

Given: $K = 1 + \dfrac{X}{\epsilon_o} \equiv$ dielectric constant

$X \equiv$ dielectric susceptibility

$\epsilon_o \equiv$ free space permittivity.

Step 1. Express X and $X(\epsilon_o)$:

$$K = 1 + \frac{X}{\epsilon_o}$$

$$= \frac{\epsilon_o + X}{\epsilon_o}$$

$$\epsilon_o(k-1) = X$$

or $X = \epsilon_o(K-1)$

Step 2. Derivation of E_p:

The dielectric permittivity of medium $= \epsilon_p = K\epsilon_o$

The flux density $= D_p = K\epsilon_o E_p$

But charge/unit area $= D_p = \sigma_p$

$\Rightarrow \quad K\epsilon_o E_p = \sigma_p$

$\Rightarrow \quad E_p = \dfrac{\sigma_p}{K\epsilon_o}$

Also $\sigma_p = XE_o \cos\Theta = \epsilon_o(K-1)E_o \cos\Theta$

and $E_p = \dfrac{\sigma_p}{K\epsilon_o} = \dfrac{XE_o \cos\Theta}{K\epsilon_o}$

$$= \frac{\epsilon_0 (K-1) E_0 \cos\Theta}{K \epsilon_0}$$

$$\Rightarrow \quad E_p = \left[\frac{K-1}{K}\right] E_0 \cos\Theta$$

Therefore $\quad \vec{E}_0 + \vec{E}_p = \vec{E}_0 - \left[\frac{K-1}{K}\right]\vec{E}_0 \cos\Theta = \vec{E}_{net}$

$$\Rightarrow \quad E_{net} = E_0\left[1-\left[\frac{K-1}{K}\right] \cos\Theta\right]$$

2. Problem: Derivation of $\sigma_T \equiv$ total charge density

Derivation:

$\sigma_T = \sigma_P + \sigma_E$

$\sigma_P \equiv$ polarization charge density or bound charge density

$\sigma_E \equiv$ charge density due to E_0 or free charge density,

But $\sigma_E = \frac{Q_e}{A}$; $\quad A \equiv$ area; $\quad Q_E \equiv$ charge on A

$$= \frac{\epsilon_0 E_0 \int da}{A} = \epsilon_0 E_0$$

and $\sigma_P = X E_0 \cos\Theta = \epsilon_0 (K-1) E_0 \cos\Theta$

$\Rightarrow \quad \sigma_T = \sigma_P + \sigma_E = -\epsilon_0 E_0 (K-1) E_0 \cos\Theta$

or $\sigma_T = \epsilon_0 E_0 [1-(K-1) \cos\Theta]$

Note that σ_P is conventionally negative because the induced polarization $\vec{p}$ act in opposition to the inducing E–field E_0, which is assumed to be in the positive direction.

3. Problem: Derivation of interaction area S. The electron cloud interacting surface used in the derivation is an approximation of the total surface. The approximation consists of assuming a spherically shaped electron cloud evolving and being deposited entirely on the dielectric. The true interacting geometry is one spherical surface overlapping a cylindrical surface. The boundary conditions are determined by the location of the spherical surface origin and the cylinder's diameter. The boundary conditions for ϕ in the approximation are set in symmetric $\pm 45°$, the elevation angle Θ boundary is determined by the thickness of the dielectric and is carried as a variable throughout the derivation.

Derivation:

$$S = r^2 \int\int d\phi \ \sin\Theta \ d\Theta.$$

Boundary conditions: Assume $-\frac{\pi}{4} \leq \phi \leq \frac{\pi}{4}$

$$\Rightarrow \quad S = r^2 \int_0^{\Theta} \sin\Theta d\Theta \int_{-\frac{\pi}{4}}^{\frac{\pi}{4}} d\phi$$

$$= r^2 \cos\Theta \int_{-\frac{\pi}{4}}^{\frac{\pi}{4}} d\phi$$

Therefore $\quad S = \frac{\pi r^2}{2} \cos\Theta$

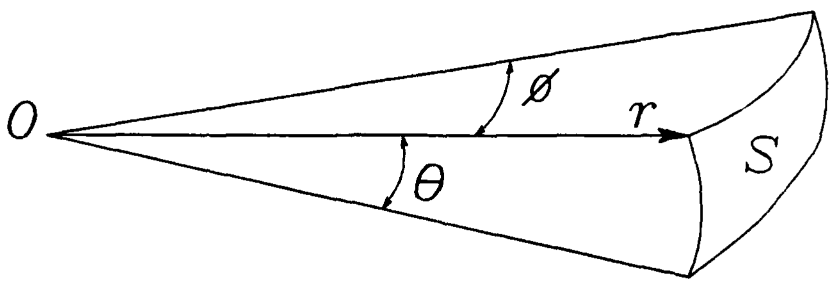

4. Problem: In the microstack below we are required to find S, the interaction area (see Problem 3) as a function of Θ and h. With the derived expression of S, we then derive the total charge Q_T on S = charge on dielectric surface. Finally, with S, Q_T, we derive the capacitance C, of the stack or any of its constituent number.

Derivation: The section of microstack taken as a unit, for analysis, consists of one dielectric layer of thickness t and one metal layer of thickness d. This assures that only one pair is counted and added to the next one.

Given: h, Θ_i; h = t+d, θ_i; i = 1, 2, 3, ..., n.

$$\text{But } \sin\Theta = \frac{h}{r}$$

$$\Rightarrow \quad r = \frac{h}{\sin\Theta} = h\csc\Theta \Rightarrow r^2 = h^2\csc^2\Theta$$

But from problem #3, p. A–3, we have $S = \frac{\pi r^2}{2} \cos\Theta$

$$\Rightarrow \quad S = \frac{\pi}{2} h^2\csc^2\Theta\cos\Theta$$

Also from problem #2, p. A–2, we have shown that

$$\sigma_T = \epsilon_0 E_0[1-(K-1) \cos\Theta]$$

$$\Rightarrow \quad Q_T = \sigma_T S = \epsilon_0 E_0[1-(K-1)\cos\Theta] \frac{\pi}{2} h^2\csc^2\Theta\cos\Theta$$

Therefore: Capacitance

$$C = \frac{Q_T}{V} = \frac{\epsilon_0 E_0}{V}\left[1-(K-1)\cos\Theta\right]\left[\frac{\pi}{2} h^2\csc^2\Theta\right]\cos\Theta$$

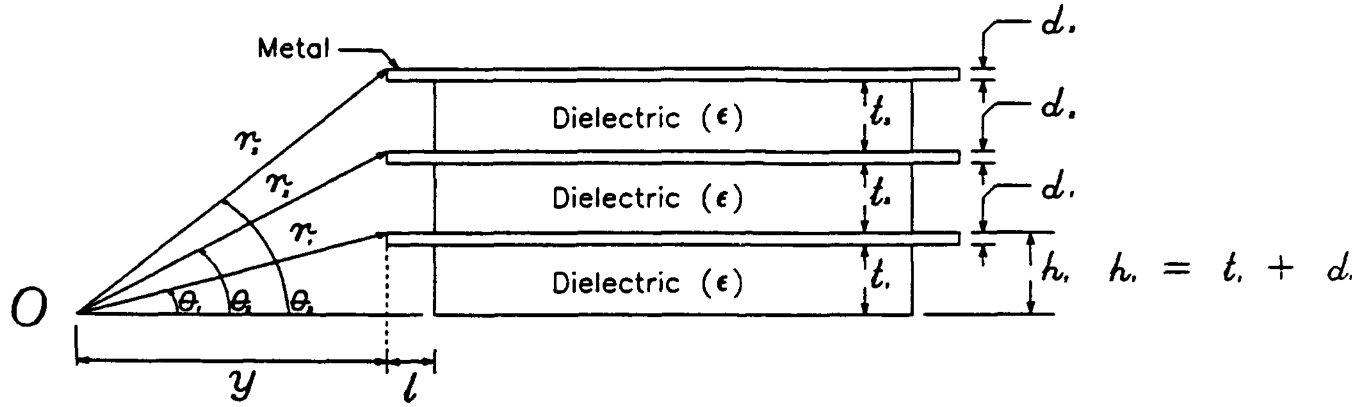

5. Problem: In the derivations of S = S(Θ) and C = C(Θ) that is, the interaction surface and capacitance respectively, the relevant angle Θ was referenced from the horizontal as shown in the diagram above. Now we intend to derive S = S(Θ) and C = C(Θ) with Θ referenced from the vertical.

Derivation:

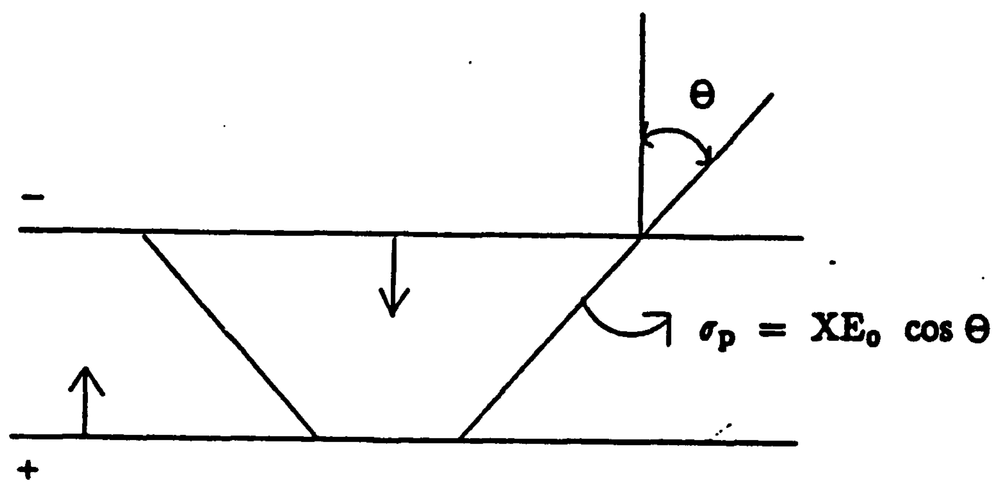

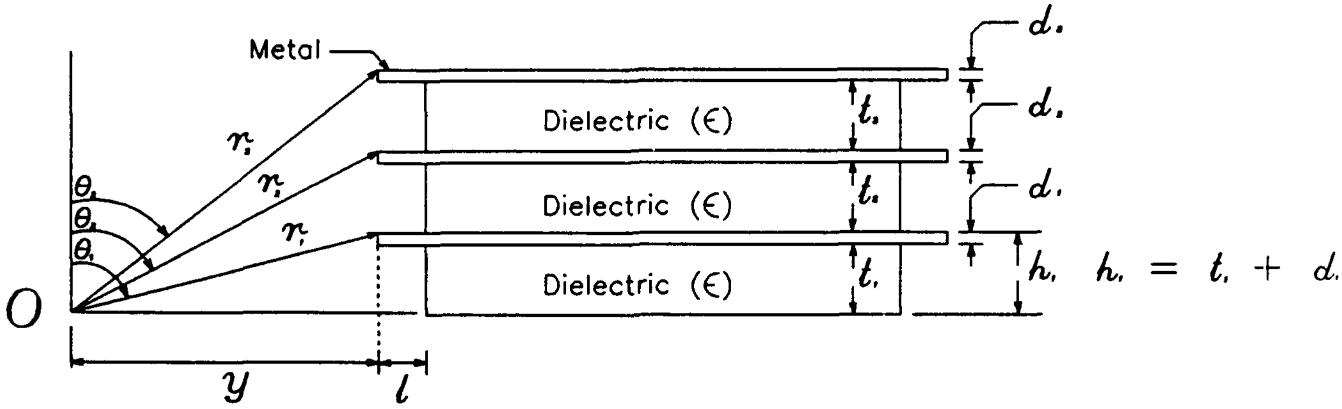

Given $\quad h = t+d, \ \Theta_i; \ i = 1, 2, 3, \ldots, n.$

$\Rightarrow \quad nh = h, 2h, 3h, \ldots, nh; \quad n \equiv$ # of stacks with each stack = h in height.

$\Rightarrow \quad r_i = r_1, r_2, r_3, \ldots, r_n.$

$$\Rightarrow \quad \frac{nh}{r_n} = \cos\Theta_n$$

Let n = 1 and i = 1 for the purpose of clarity or illustration

$$\Rightarrow \quad r_1 = \frac{h}{\cos\Theta_1} = h\sec\Theta_1.$$

Therefore as a general case then we have

$$r_n = \frac{nh}{\cos\Theta_n} = nh\sec\Theta_n$$

But from Problem #3, p. A–3, we have $S = \frac{\pi r^2}{2} \cos\Theta$

$$\Rightarrow \quad S = \frac{\pi}{2} n^2h^2\sec^2\Theta_n\cos\Theta_n$$

Also from problem #2, p. A–2, we derived that

$$\sigma_T = \epsilon_0 E_0[1-(K-1)\cos\Theta_n]$$

$$\Rightarrow \quad Q_T = \sigma_T S = \epsilon_0 E_0[1-(K-1)\cos\Theta_n]\left[\frac{\pi}{2} n^2h^2\sec^2\Theta_n\right]\cos\Theta_n$$

The previous results are used to correlate test results and test the preliminary criteria used for sample fabrication.

Also from problem #2, p. A–2, we derived that

$$\sigma_T = \epsilon_0 E_0[1-(K-1)\cos\Theta]$$

$$\Rightarrow \quad Q_T = \sigma_T S = \epsilon_0 E_0[1+(K-1)\cos\Theta] \frac{\pi}{2} h^2 \csc^2\Theta \cos\Theta$$

Therefore: Capacitance

$$C = \frac{Q_T}{V} = \frac{\epsilon_0 E_0}{V} \left[1-(K-1)\cos\Theta\right]\left[\frac{\pi}{2} h^2 \csc^2\Theta\right]\cos\Theta$$

APPENDIX B
BALLISTIC ELECTRON TRAJECTORIES

The most effective thickness of the layers can be estimated by calculating the typical distance an electron will travel before striking the surface. By using the notation as indicated in Figure 57, if emission takes place at an angle ϕ, measured from the normal to the insulator surface, and at energies W_0 the distance h is given by:

$$h = \frac{W_0 \cos\phi}{qE_n} \tag{B.1}$$

The normal acceleration, a_n is given by:

$$a_n = \frac{qE_n}{m_e} \text{ or } F = qE_n = ma_n \tag{B.2}$$

and the acceleration parallel to the surface a_p, is given by:

$$a_p = \frac{qE_0}{m_e} \tag{B.3}$$

The range of the trajectory r, which measures the distance traveled by the electron parallel to the insulator surface is given by:

$$r = \tfrac{1}{2}\, a_p(2t)^2 = \frac{4W_0E_0\cos\phi}{qE_n{}^2} \tag{B.4}$$

where t is the electron time of flight (assuming no collisions) given by:

$$t = \frac{2m_eW_0\cos\phi^{\frac{1}{2}}}{q\,E_n} \tag{B.5}$$

The electron gains some kinetic energy by means of the potential energy before restricking the surface. The final kinetic energy W_0 can be expressed as:

$$W_1 = W_0 + rqW_0 = W_0 \left[1 + 2\left[\frac{E_0}{E_n}\right]^2\right] \tag{B.6}$$

Typical values of r for energies between 25 KeV and 1.4 KeV, corresponding to angles of 16° to 40°, range from 1 μm to about 1 mm. The normal field E_n is reduced drastically once the metal plates are inserted. This is because the surface charge is now distributed by the capacitor formed between the metal plates and the resulting parallel potential surfaces. The change in the normal field value will effectively increase the electron hopping distance.

The field produced by the positive charge in the plane geometry is:

$$E_n = \frac{\sigma^+}{2E_0} \tag{B.7}$$

where E_0: Permittivity of free space

σ^+: Charge density in C/cm^2

When the electrons drift towards the anode, the value of σ_- diminishes, but at the same time, the positive surface charge at the insulator–cathode junction enhances the field at the cathode triple point. This increased emission maintains σ_- equal to σ^+. The surface current carried by secondary emission avalanche per cm can be written as:

$$I_{11} = \sigma_- v_e \tag{B.8}$$

where I_{11}: Current per unit length (A/cm)

v_e: Average drift velocity

with W_1 as the final energy and the averaged drift velocity:

$$W_1 = \tfrac{1}{2} m v_e^2 \tag{B.9}$$

The velocity:

$$<v_e> = \left[\frac{2\,W_1}{m\ e}\right]^{\frac{1}{2}} \tag{B.10}$$

The surface current is then:

$$I_{11} = \sigma_{-} \left[\frac{2W_1}{m_e}\right]^{\frac{1}{2}} \tag{B.11}$$

From this equation surface charge calculations can be made from pre–breakdown current data. The electrons are returned to the surface after traveling a distance given by equation B1, the normal field is estimated from estimating σ_{-} from equation B11 and assuming that at equilibrium $\sigma_{-} = \sigma^{+}$ then:

$$h = \frac{W_0 \cos\phi (2E_0)}{q \; I_{11}} \left[\frac{2W_1}{m_e}\right]^{\frac{1}{2}}$$

this yields:

$$h = \frac{2W_0 \; [2W_1]^{\frac{1}{2}} \; E_0 \cos\phi}{q (m_e)^{\frac{1}{2}} \; I_{11}} \tag{B.12}$$

W_1 and W_0 are given by the material $\cos\phi$ is inferred as a maximum from the electrode size and I_{11} is the pre–breakdown current.

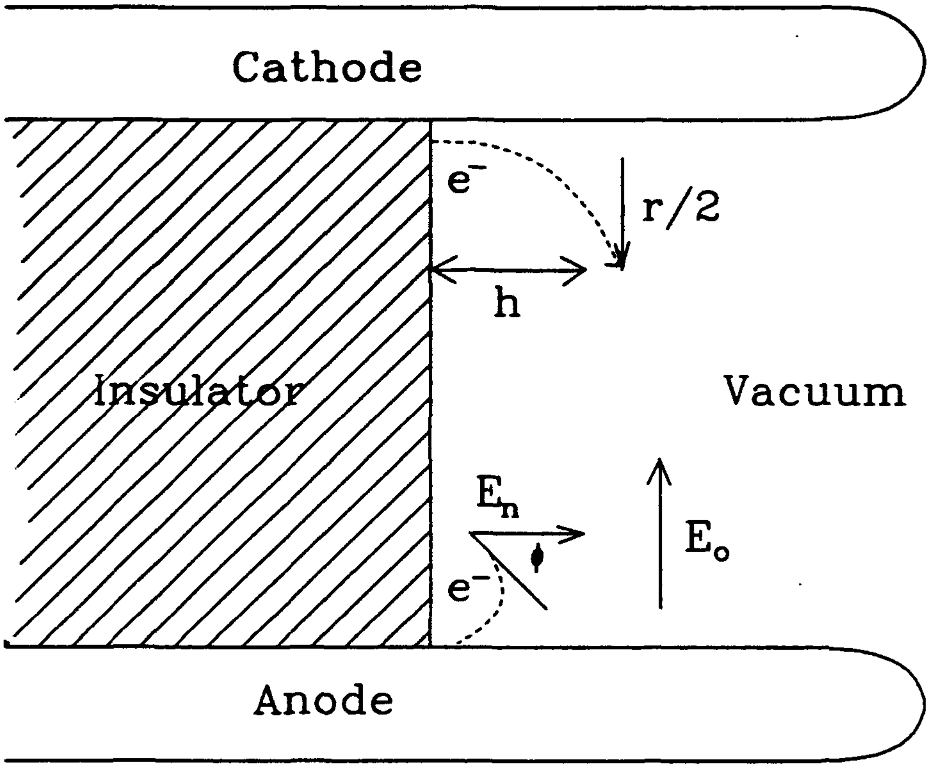

Figure 57. **Trajectory of an electron emitted from an insulator. E_n is the field due to surface charging.**

APPENDIX C

GRAPHIC REPRESENTATION OF THE FLASHOVER PHENOMENA

The program plan for the microstack did not call for a computer modeling of the surface flashover phenomena. After testing the hypothesis that the microstack improves the surface flashover value of the system, the physics relevant to the process is basically as follows:

a) Charge deposition in the dielectric surface is fragmented and reduced as much as 80% depending on the electron emission point. As shown in Chapter 2 this is a strong function of the angle and in consequence to the electrode dimensions.

b) Electron avalanche processes are controlled. The initiation of electronic flow on the dielectric surface from the triple point is controlled by the interruption that the metallic shield imposes on the surface space charge. The shield also acts as a storage capacitor, typical values range from a few picofarads to a few nanofarads.

c) Desorbed material from the surface in one section makes no contribution to an adjacent surface section.

d) Emission from one shielded section may not start until it completely saturates, if the pulse length is short (few nsec) no opportunity is present for flashover.

To understand the significance of the breakthrough that the microstack technology represents, a review of surface flashover phenomena is in order. The representation that follows is not from equation–driven computer modeling but more of computer animation using first principles. It is intended for a better understanding on the technology and to stress the need for a computer based model now that the concept and the technology has been experimentally proven.

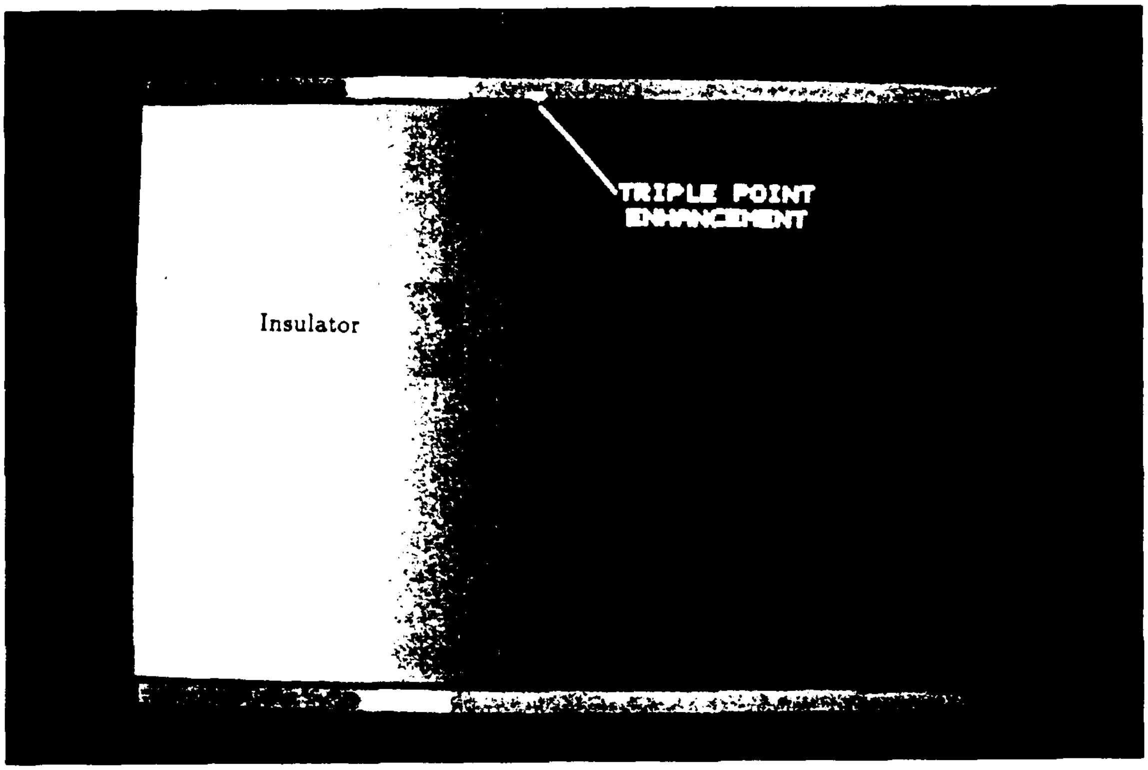

Figure 58 Initial electron with energy W_0 hits the surface of the Dielectric. The red spot on the cathode surface represents the point of enhancement or triple point. It is assumed that a number of electrons with a given angular distribution will acquire enough energy that when they hit the surface secondary electron emission is induced. The angular distribution in the electron emission can usually be approximated by a cosine law with respect to an axis perpendicular to the emitting surface (Ref. 17).

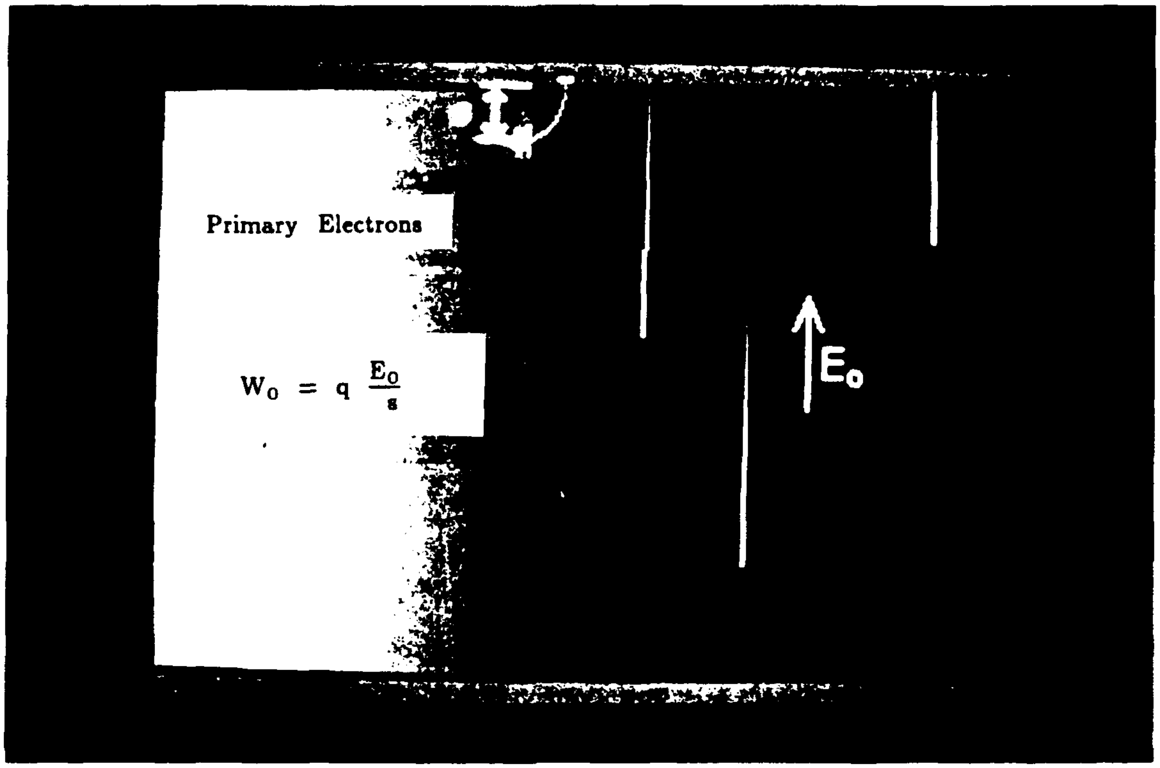

Figure 59. For sake of simplicity a secondary electron emission $\delta = 2$ is assumed with two electrons ejected out from the dielectric surface. At this point a positive surface charge is left behind at the dielectric surface. The field generated by the positive charge affects the exterior field, bending some of the electric line towards the dielectric surface.

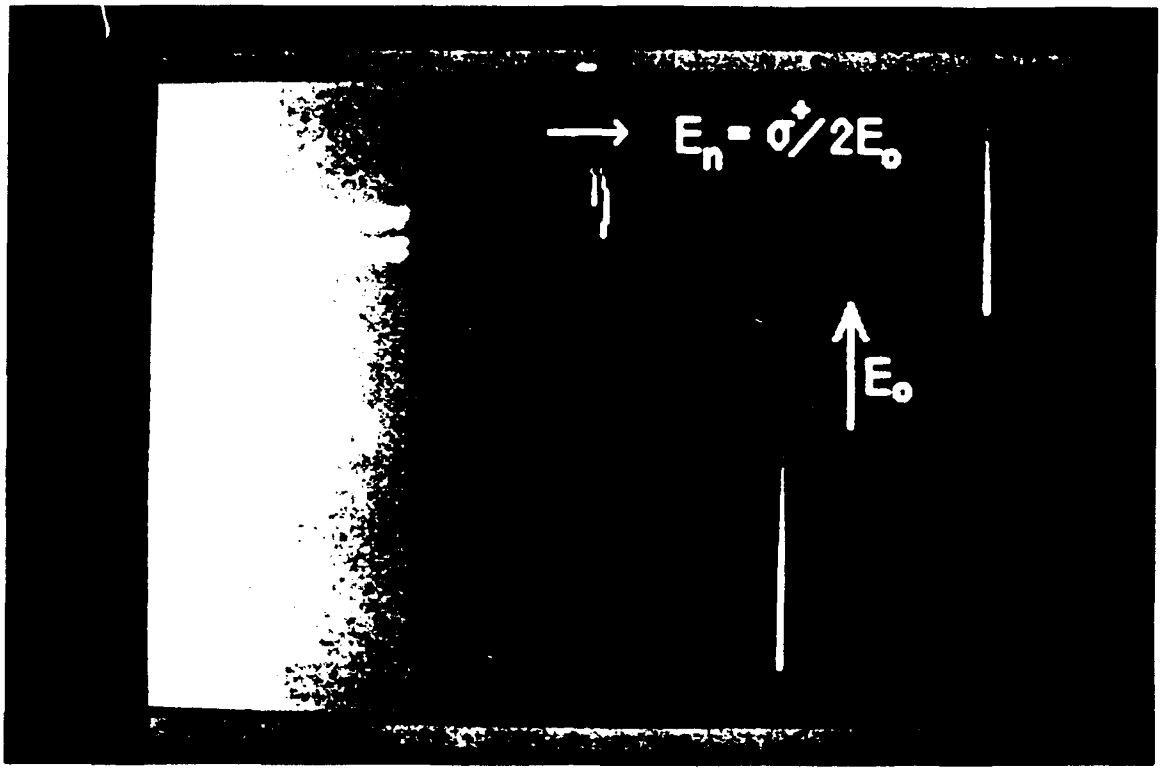

Figure 6c The first group of secondary electrons hits the surface as a result of the field changes due to positive surface charge. The trajectory or range of the electrons emitted from the insulator surface will decrease as the surface charge density increases. The energy at impact will therefore decrease (Ref. 18).

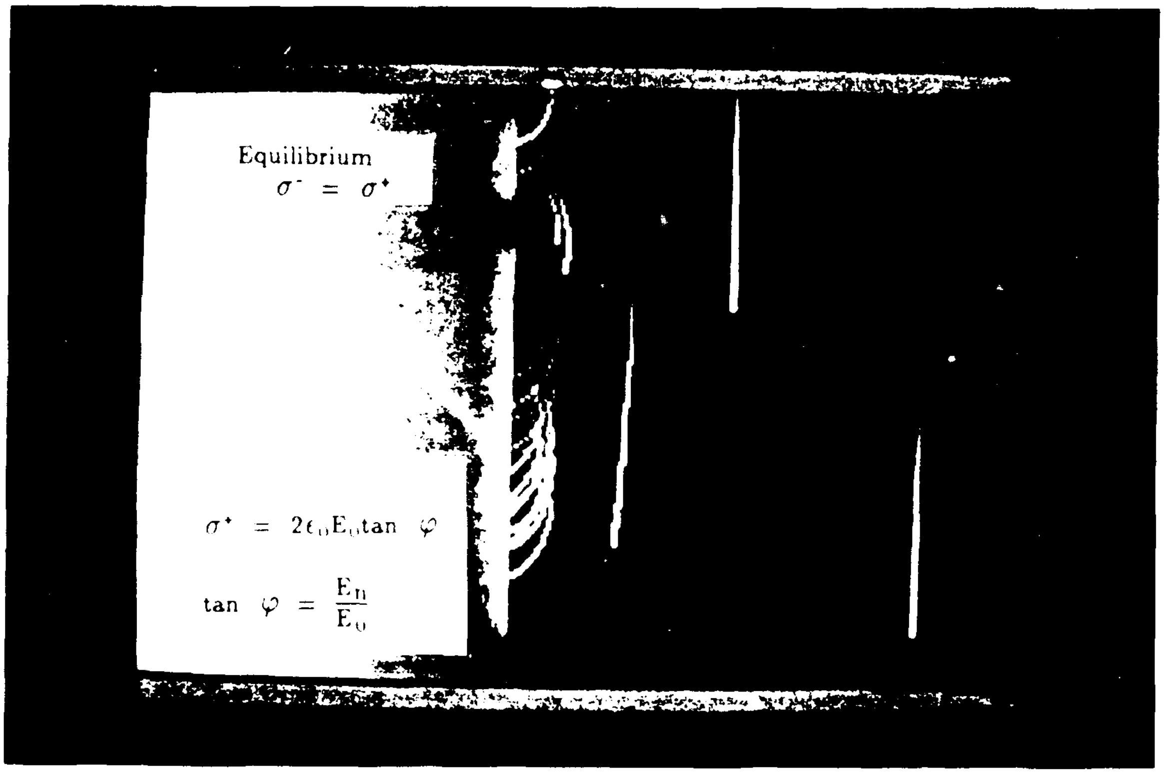

Figure 61 As more positive surface charge is accumulated the process becomes self aggravated and a full streamer propagates. Notice that a "space—charge" is formed between the flying electrons and the surface charge, they self support and develop as the process continues.

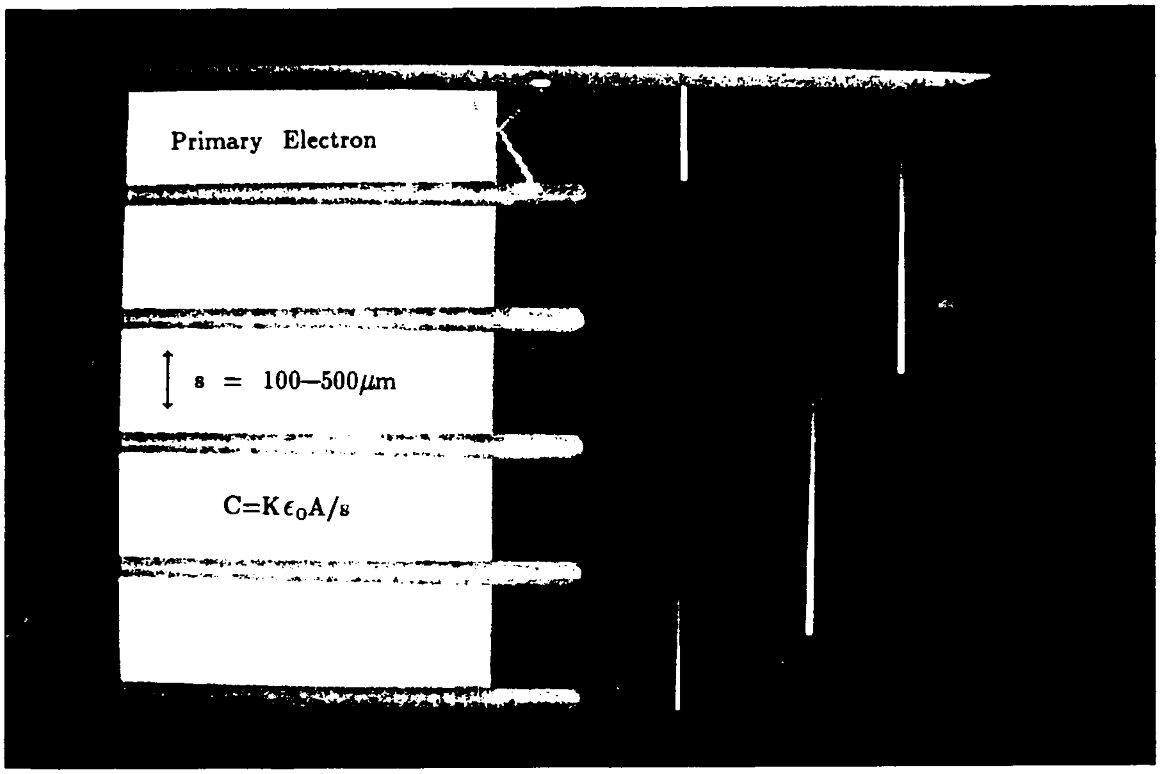

Figure 62. With the microstack and the metal shielding the anode–cathode structure is not disturbed. The metal wafers help the equipotential lines to cross the insulator structure thus causing a minimum field perturbation.

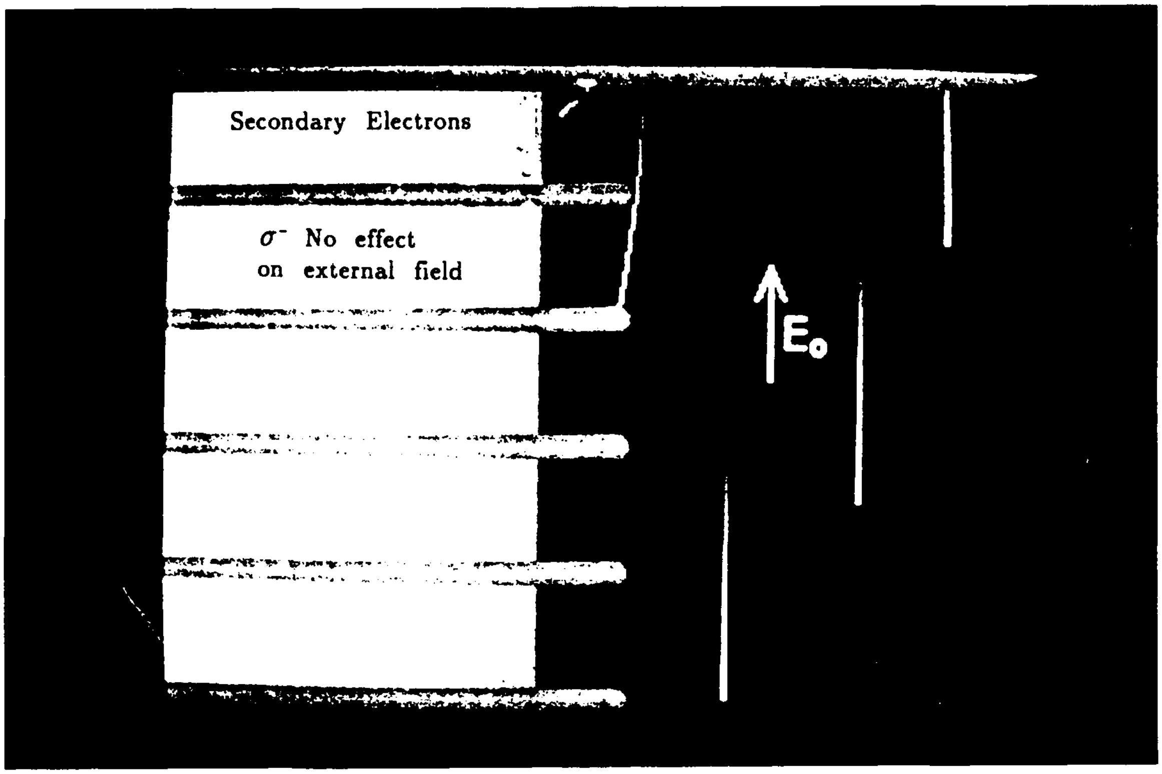

Figure 63. As electrons start hitting the surface, they may generate secondary electron emission but the metal wafer now will stop them. All the charge trapped by the wafer shield is then distributed in the capacitor formed by the wafer and dielectric with the cathode of subsequent wafers.

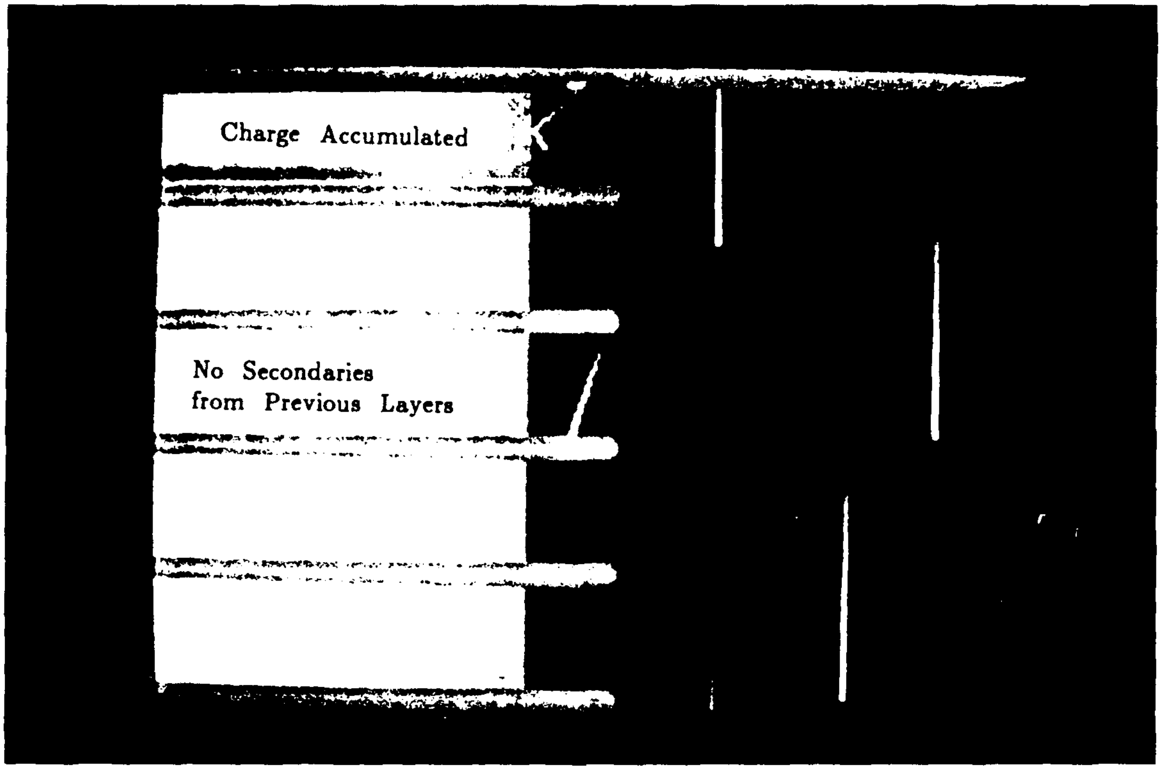

Figure 64. As charge accumulates in the first layers, the subsequent layers may start participating on emitting electrons The failure process for microstack may be one of sequential saturation of the layers.

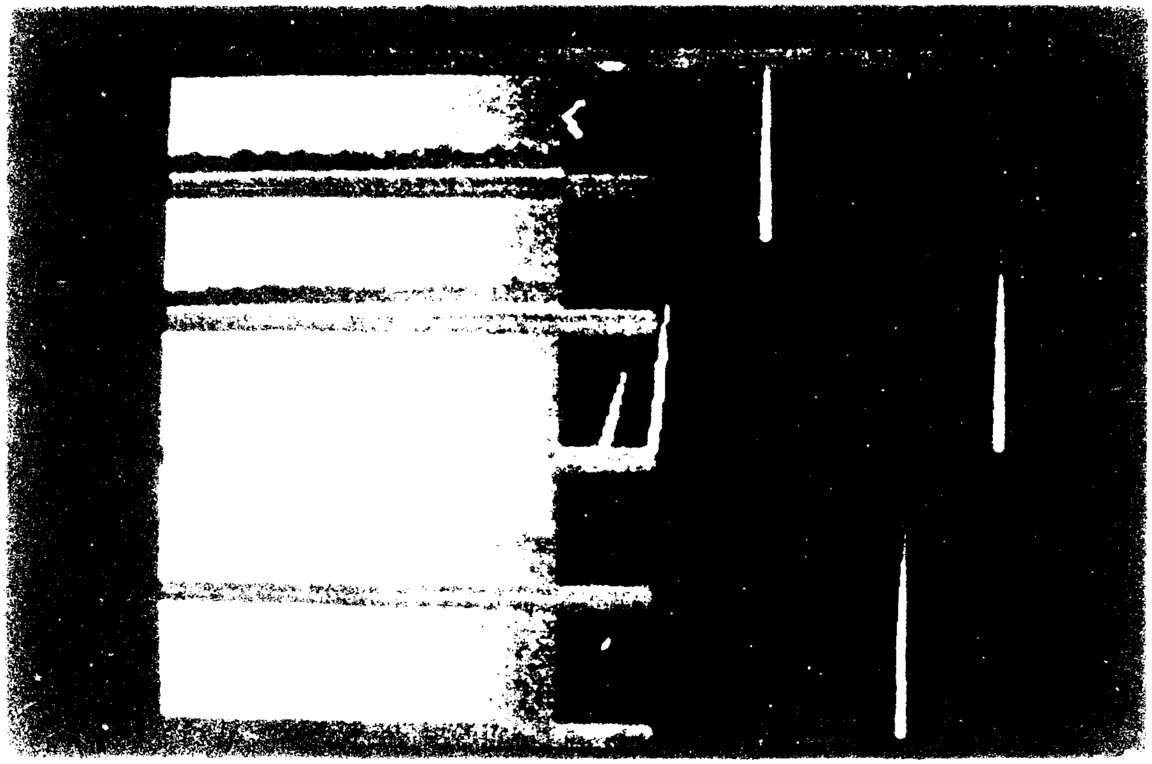

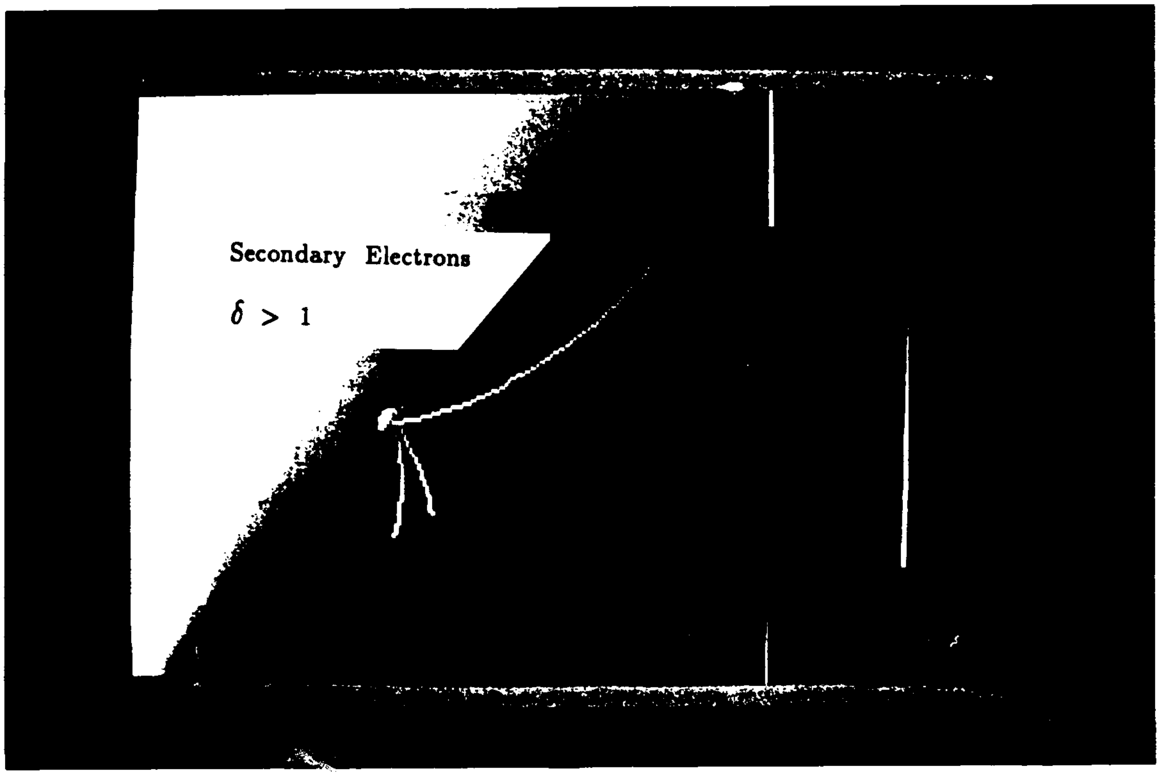

Figure 66. A typical conventional insulator cut at 45°, shows in a very simple way, the primary electrons with a very shallow emission angle, or right from the triple point, are the ones affecting the surface.

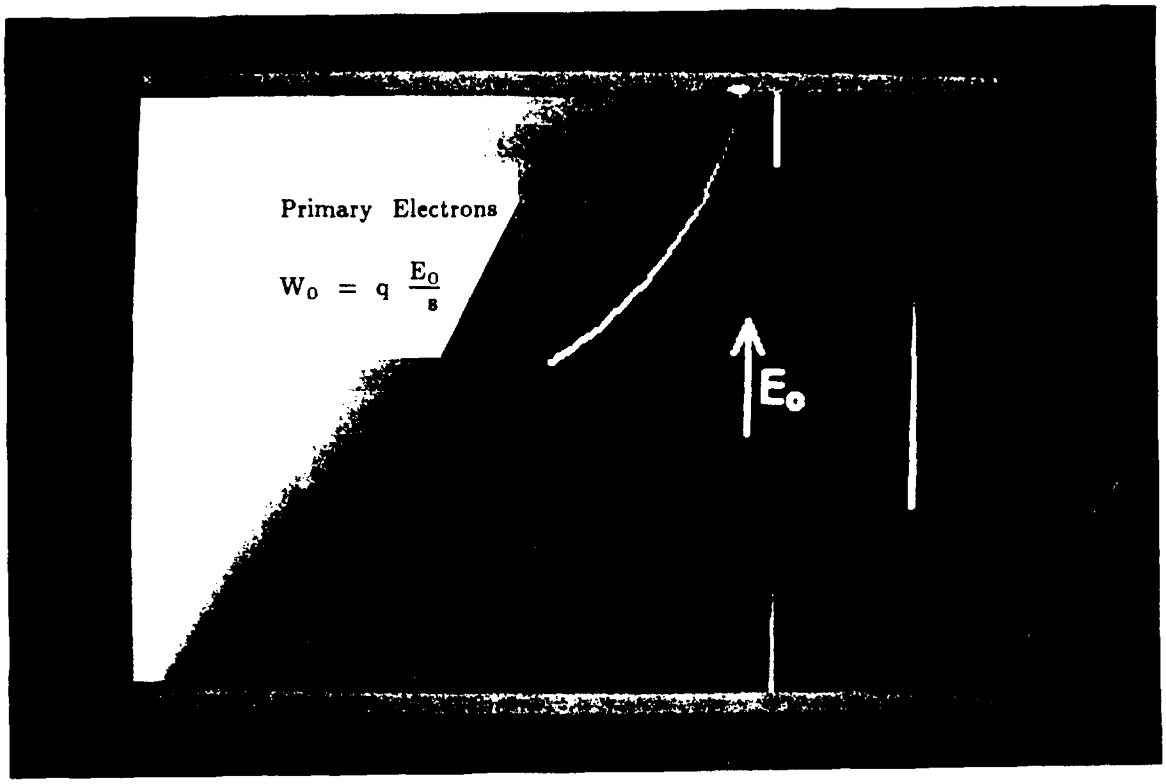

Figure 67. If primary electron hits the surface, any secondaries emitted will follow a path that is away from the surface, and driven by the external field. This way the best results were obtained by combining the microstack shielding and the 45° inclination.

APPENDIX D
1MV TRIGATRON DESIGN

The crowbar for the MSI2 pulse power system was designed to have the following capabilities:

Operating Voltage Range	200kV – 1.2MV
Pressure Range	1Atm – 100psig
Gas	SF_6 – SF_6, Air Mix
Size Limitations	~14" cube
Switching Jitter	$\leq$ 10ns

The design of this switch is based on the experience gained on a separate program crowbar but with added improvements. Critical parameters in optimum operation are the Gap vs Voltage ratios between the main electrode and the trigger electrode.

$$\frac{V_{trig}}{V_{sw} - V_{trig}} \quad \frac{s}{d}$$

For the LWT2 crowbar a successful s/d ratio has been ~ 0.12 (others have reported s/d = 0.15). In this case we want a trigger voltage range of:

$$V_{trig} = \left[\frac{s/d}{1 + s/d}\right] V_{sw} \qquad 200\text{kV} \leq V_{sw} \leq 1.2\text{MV}$$

$$20\text{kV} \leq V_{trig} \leq 130\text{kV}$$

The MSI trigger voltage V_{trig} was set between 50 to 100 kV. To set the gap spacing we conducted ELF calculations for the field enhancement factor (FEF) using an available electrode contour (see Figure 68) at gaps between 2.5 to 6 cm. The results are shown in Figure 69. A gap spacing of 3.5 cm seems to be the optimum. The FEF calculated at 1.24 should keep in the $\leq$ 100 psig range for SF_6 at 3.5 cm gap. To confirm this, we used Charlie Martin's uniform field equation for breakdown in Air, and modified it for SF_6 using a conversion relationship given by I. M. Bortnic and B. A. Gorjunov (Ref. D1). Then folding in the FEF for the electrode contour at 315 cm, we get the following equation for breakdown:

$$V_{BD} = [(24.5p + 6.7\ (p/d)^{1/2}]\ [2.93 - 0.05p/d]\ /\mathrm{FEF}\ \text{in Atm., in cm}$$

The results are plotted in Figure 70 along with the curves for + second trigatron design breakdown and operational levels at 3cm gap and 1.57 FEF. The optimum polarity for a trigatron should be negative on the main electrode and positive on the trigger electrode relative to the ground or base electrode. If the vacuum insulator in the test cell can be fabricated for this configuration, then the switching jitter will be minimized and we should be able to meet the 10 ns jitter spec. Figures 71 through 82 show the final design and the overall piece parts, for a 500 kV AND A 1MV trigatron system.

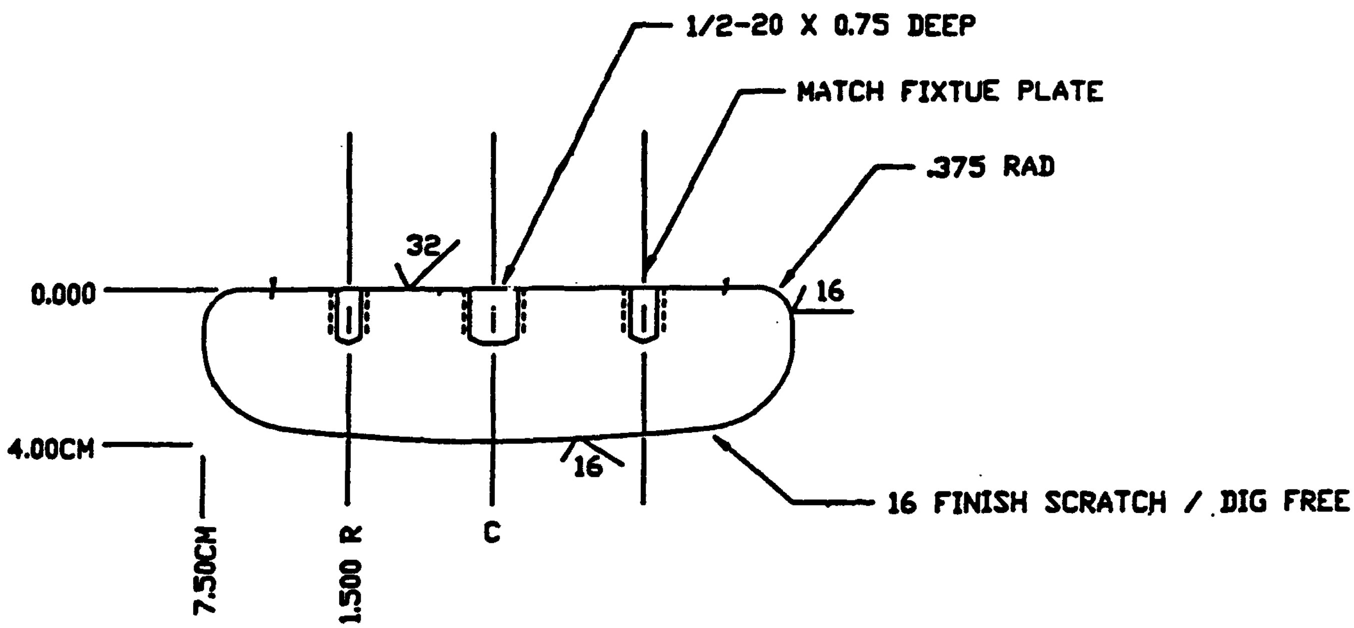

Figure 68. Electrode 6061–T6 aluminum.

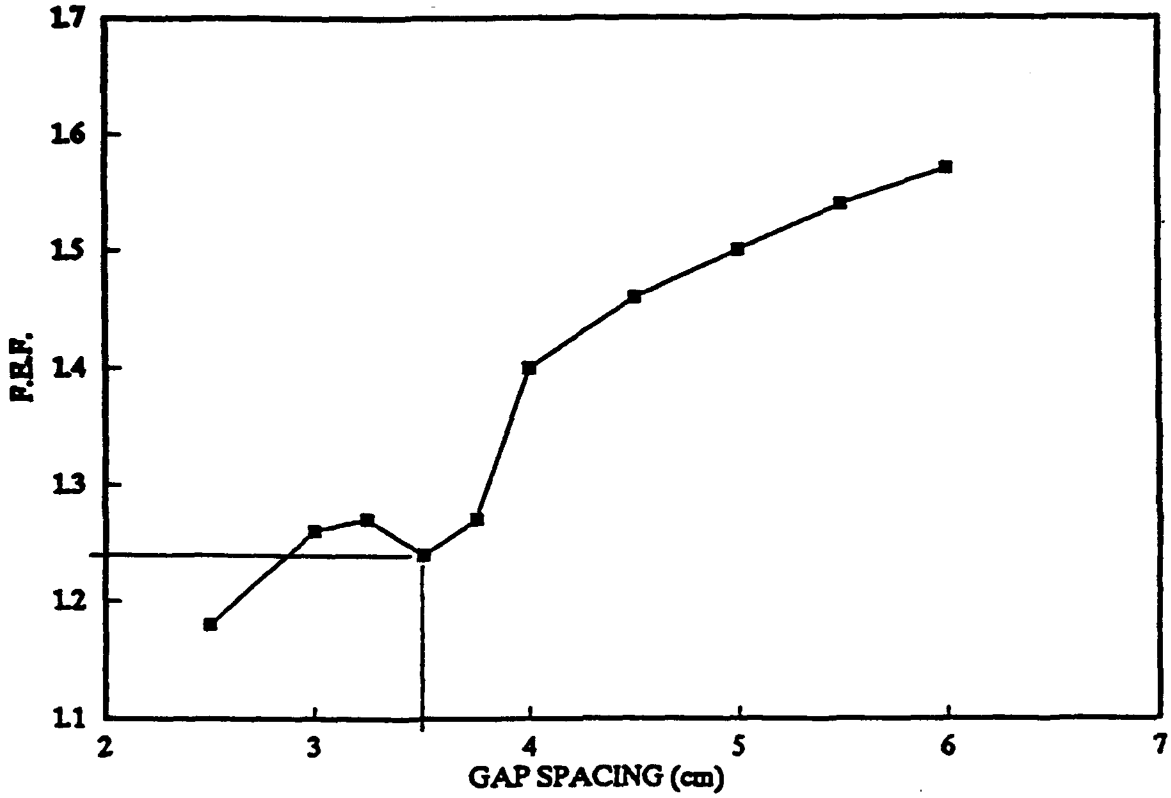

SANDIA ELECTRODE CONTOUR

GAP (cm)	FEF
2.5	1.18
3	1.26
3.25	1.27
3.5	1.24
3.75	1.27
4	1.4
4.5	1.46
5	1.5
5.5	1.54
6	1.57

Figure 69. Sandia electrode contour.

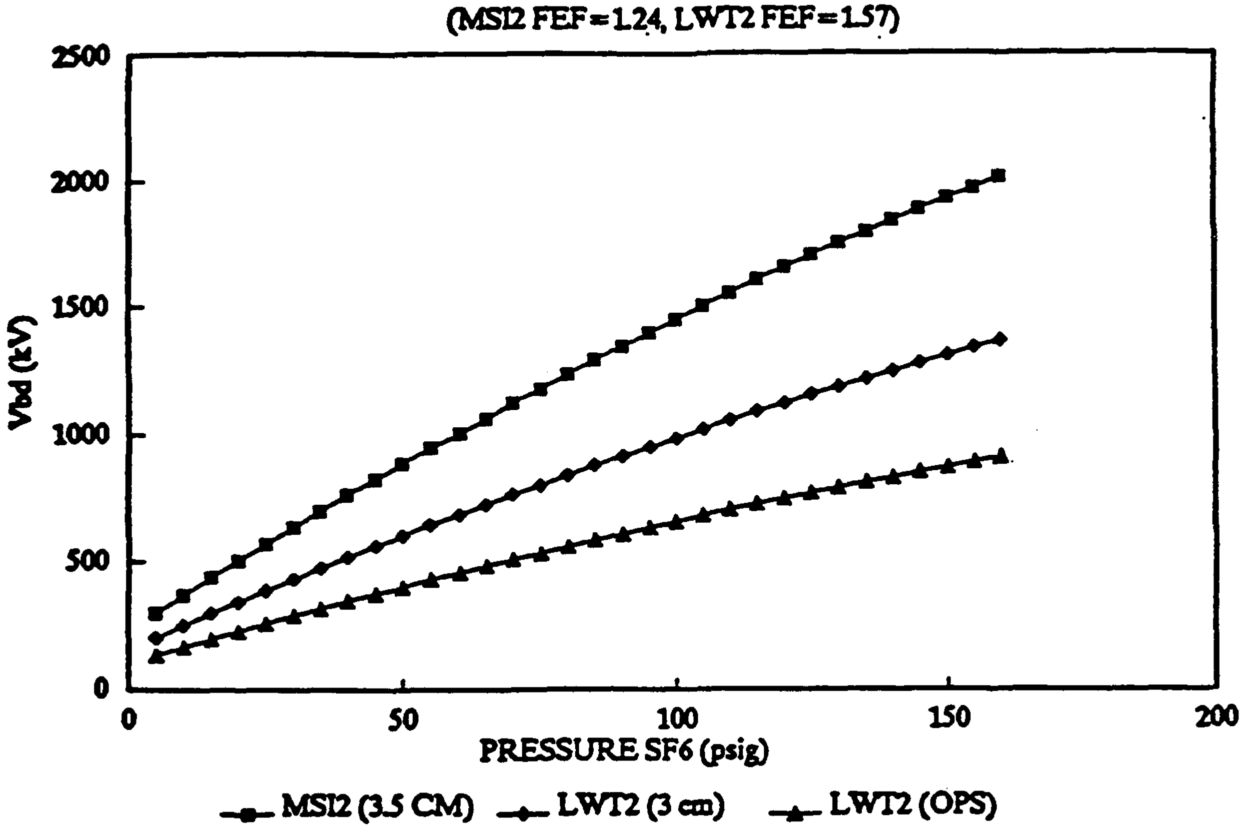

Figure 70. Trigatron breakdown curve.

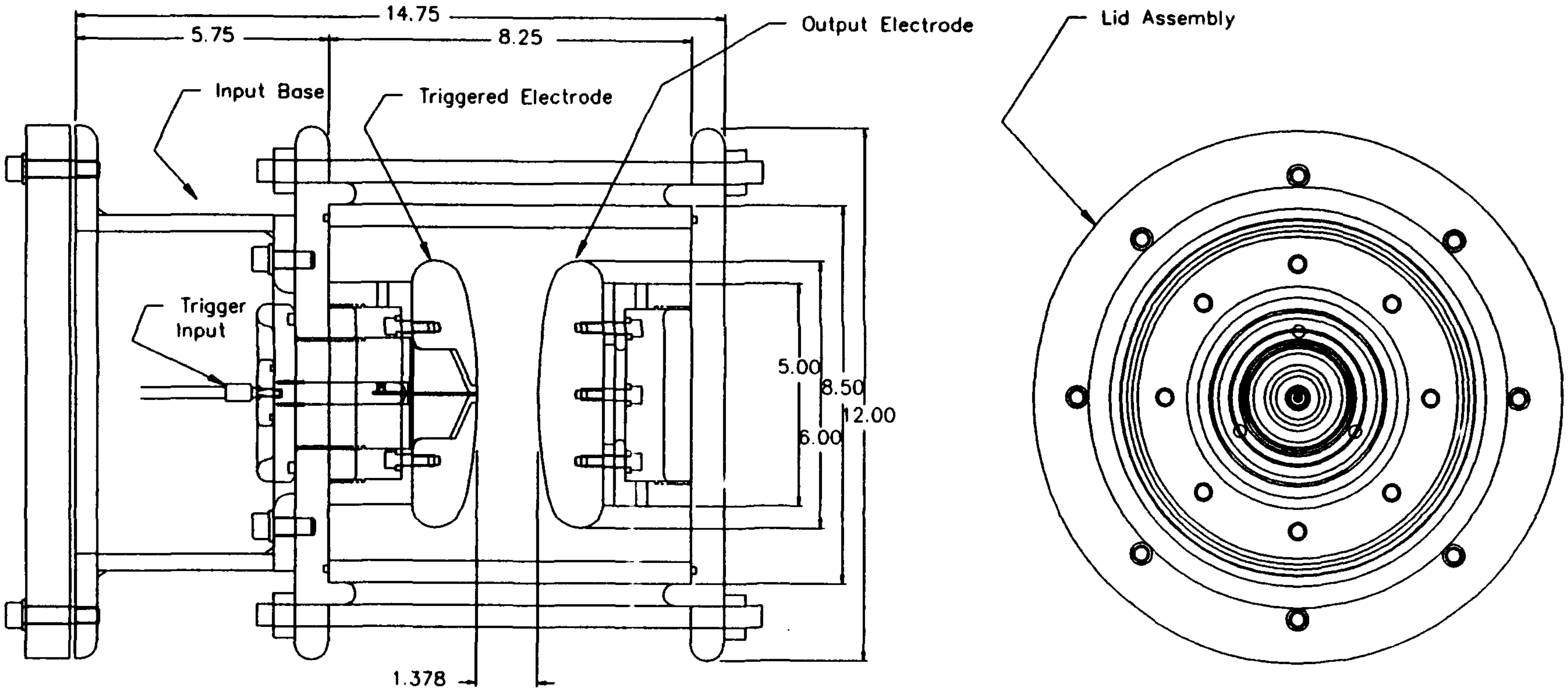

Figure 71. Trigatron general assembly.

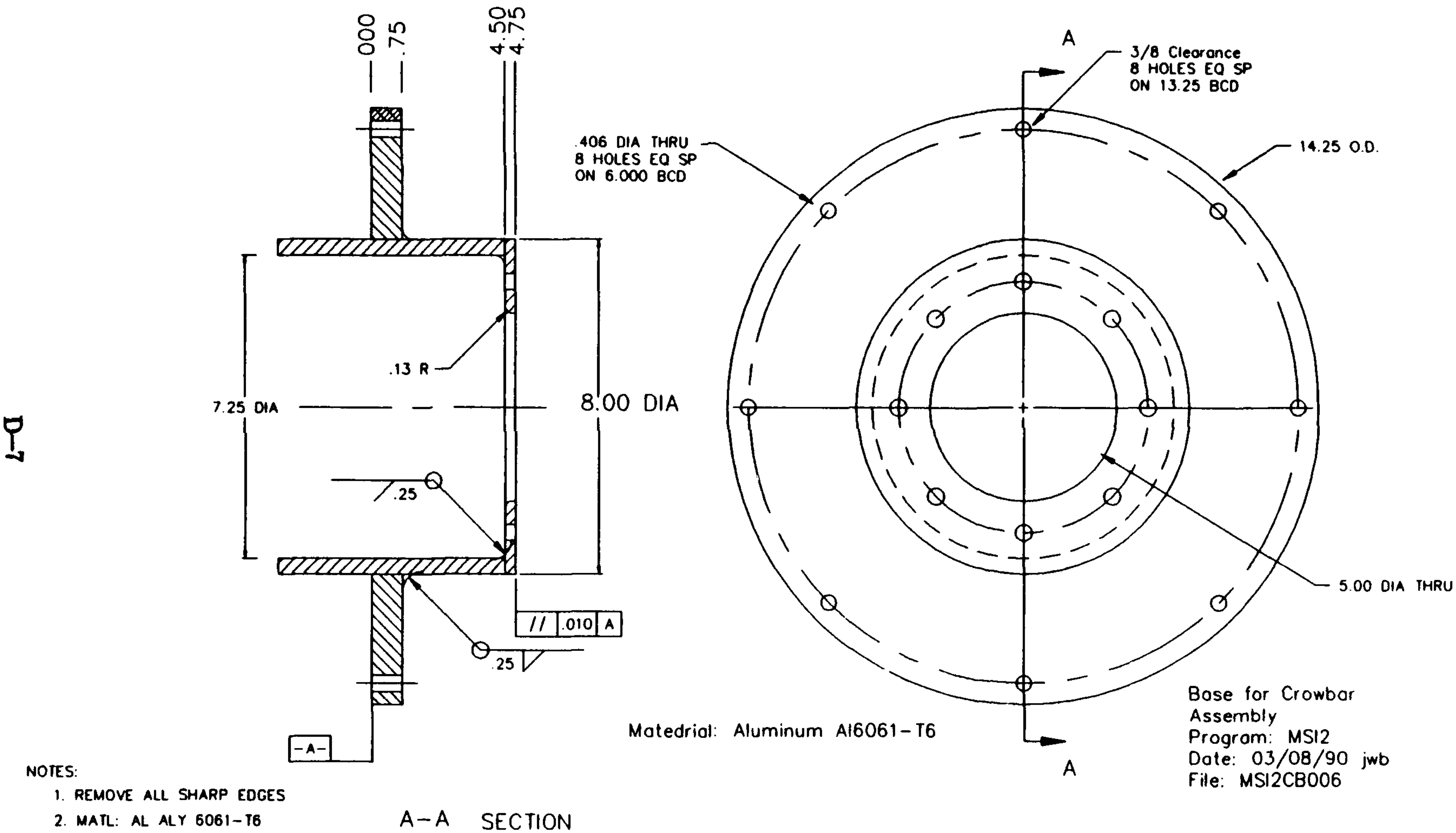

Figure 72. Trigatron input base point.

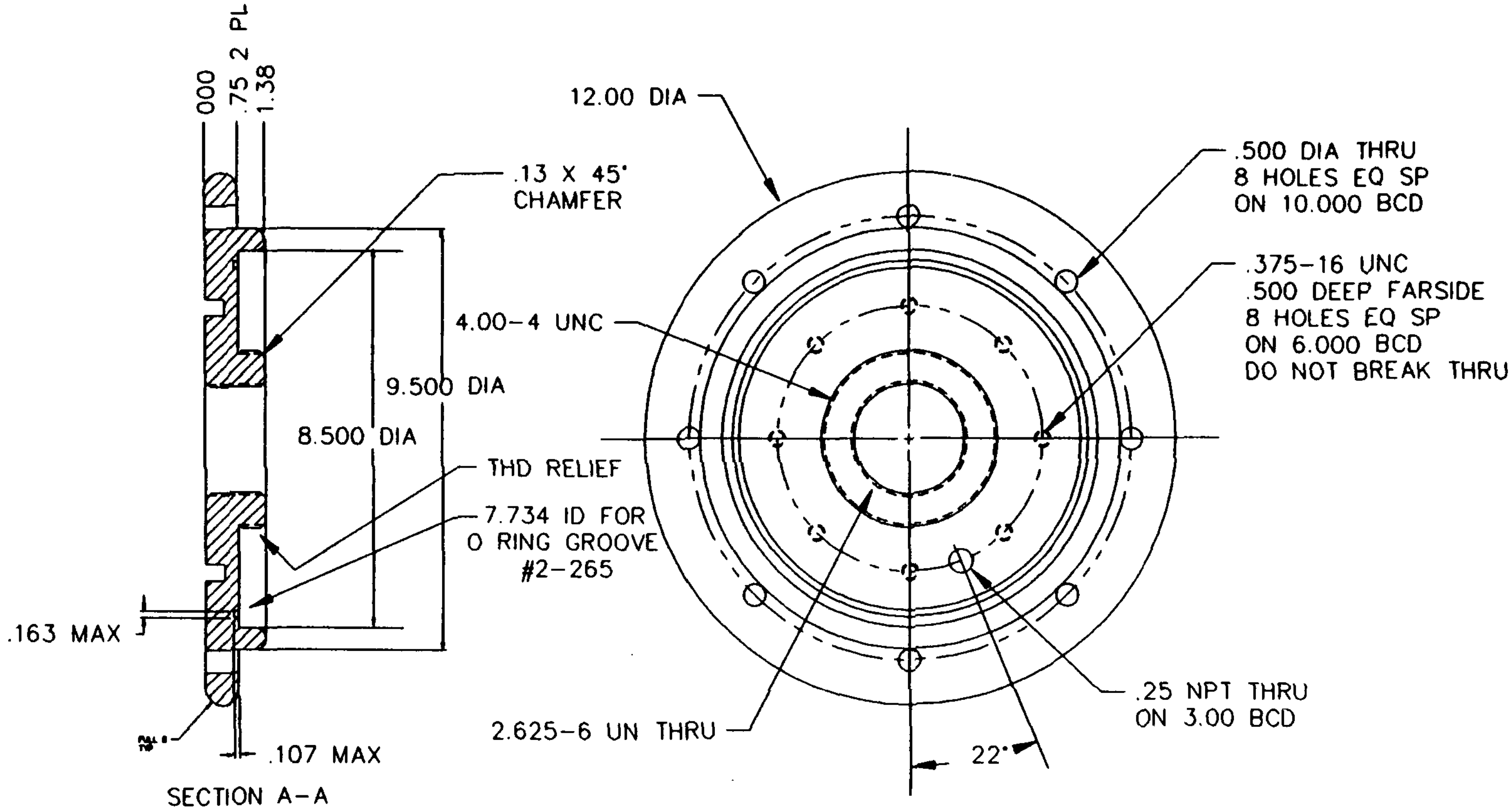

NOTES:

1. REMOVE ALL SHARP EDGES
2. MATL: AL ALY 6061-T6

BASE1
SCALE: 1=1

Figure 73. Trigatron input electrode base.

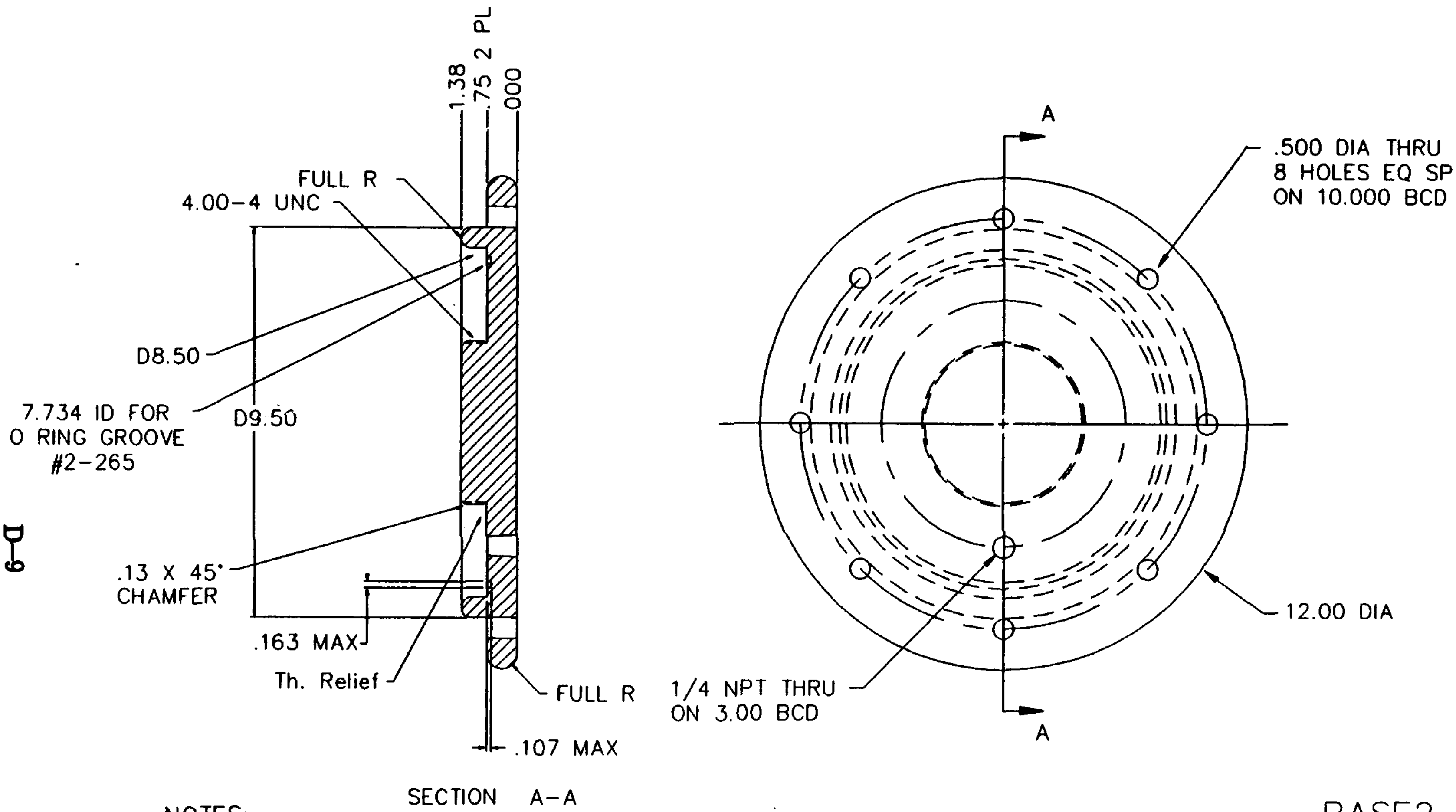

NOTES:

1. REMOVE ALL SHARP EDGES
2. MATL: AL ALY 6061-T6

BASE2
SCALE: 1=1

Figure 74. Trigatron output base.

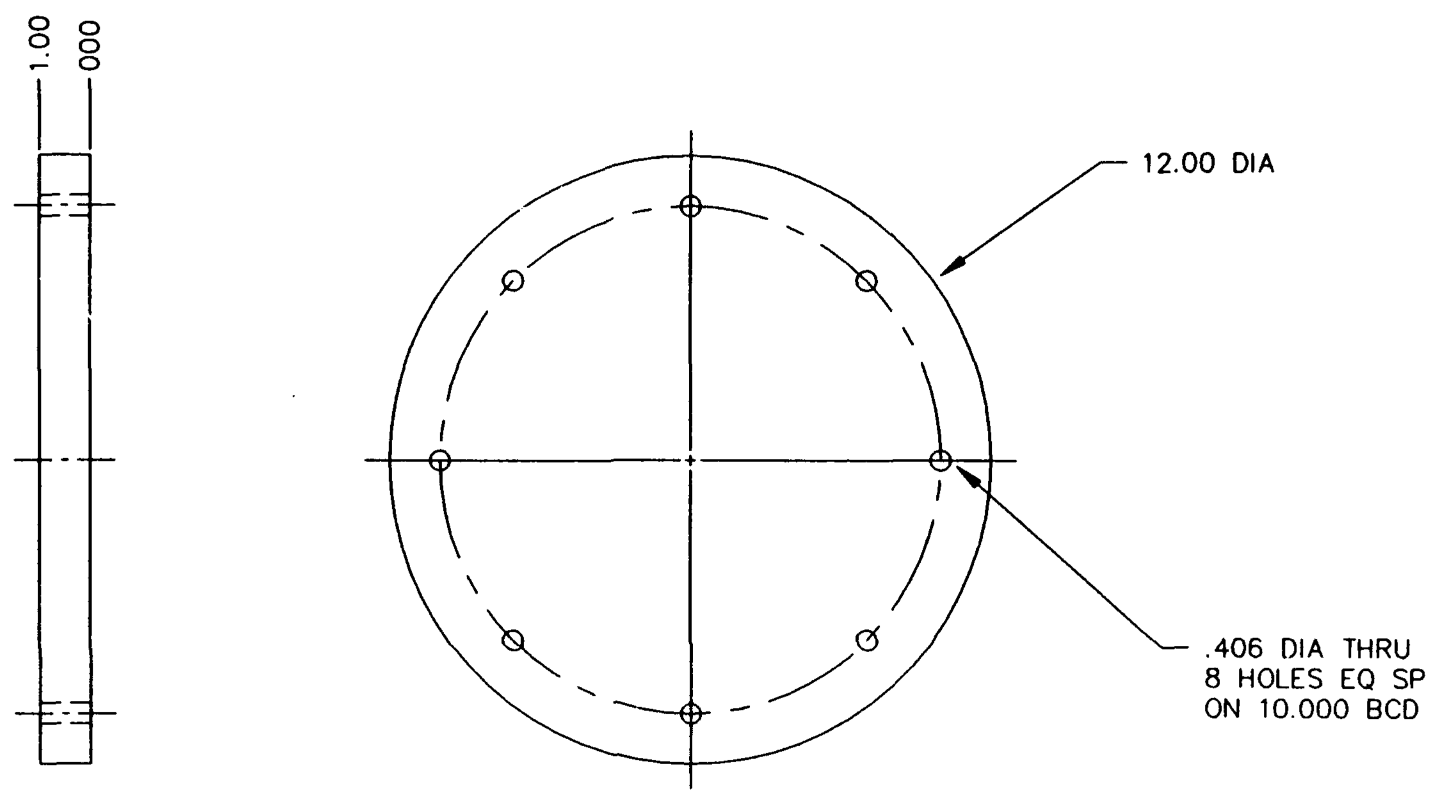

NOTES:

1. REMOVE ALL SHARP EDGES
2. MATL: MILD STEEL

Figure 75. Flange Spacer.

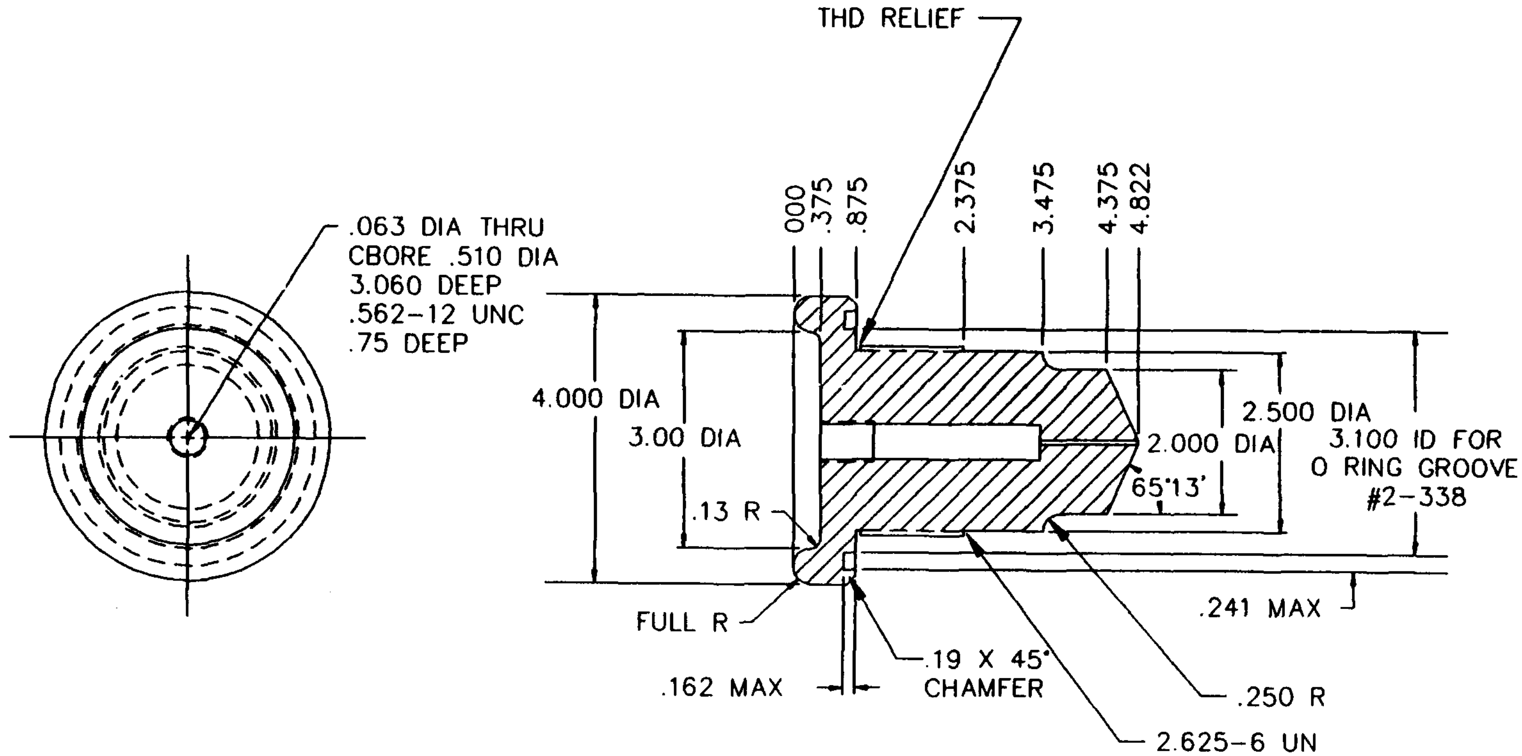

NOTES:

1. REMOVE ALL SHARP EDGES
2. MATL: LEXAN

SECTION A-A
POLY
SCALE: 1=1

Figure 76. Trigger pin insulator.

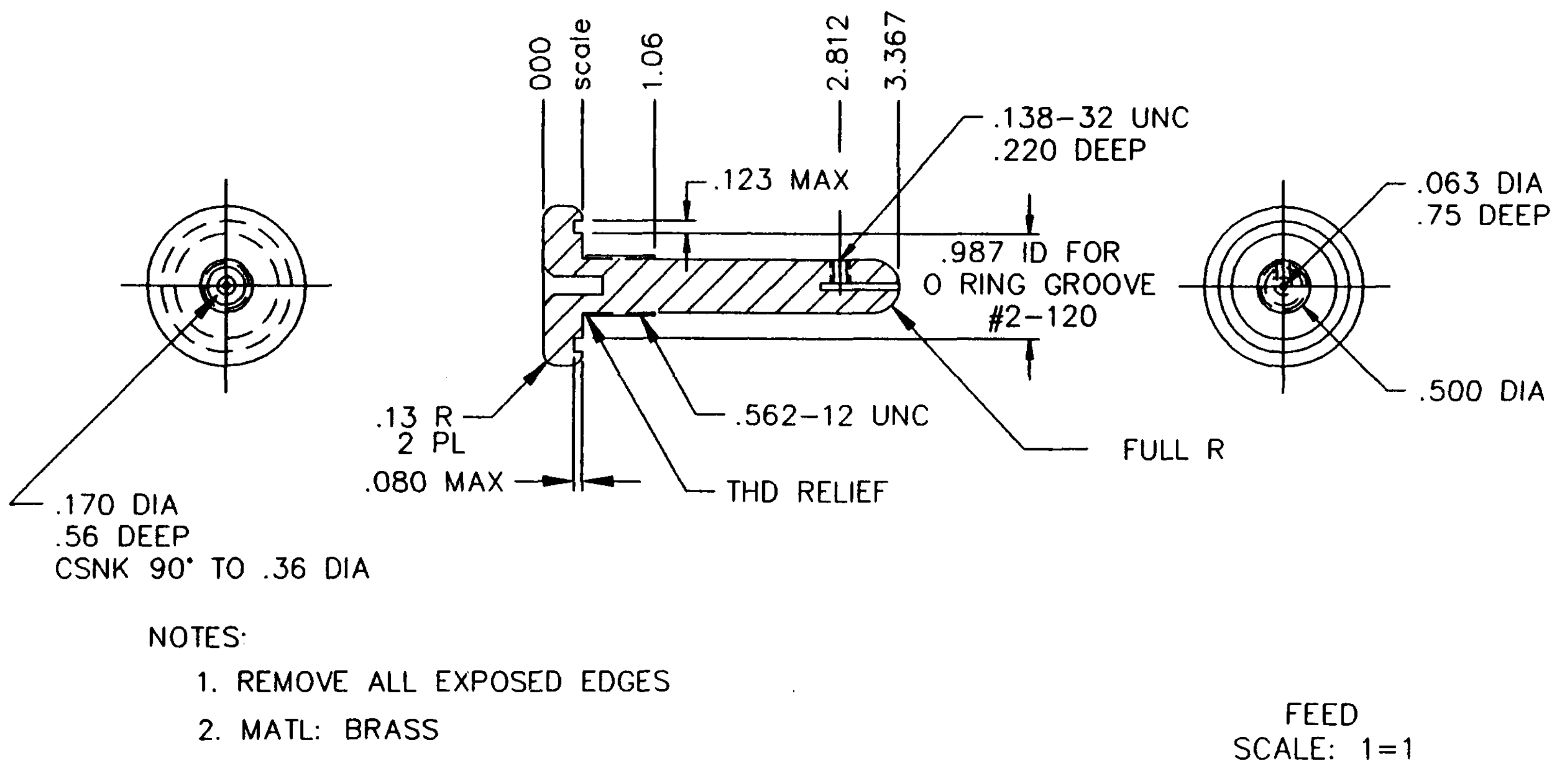

Figure 77. Trigger pin feed cnd holder.

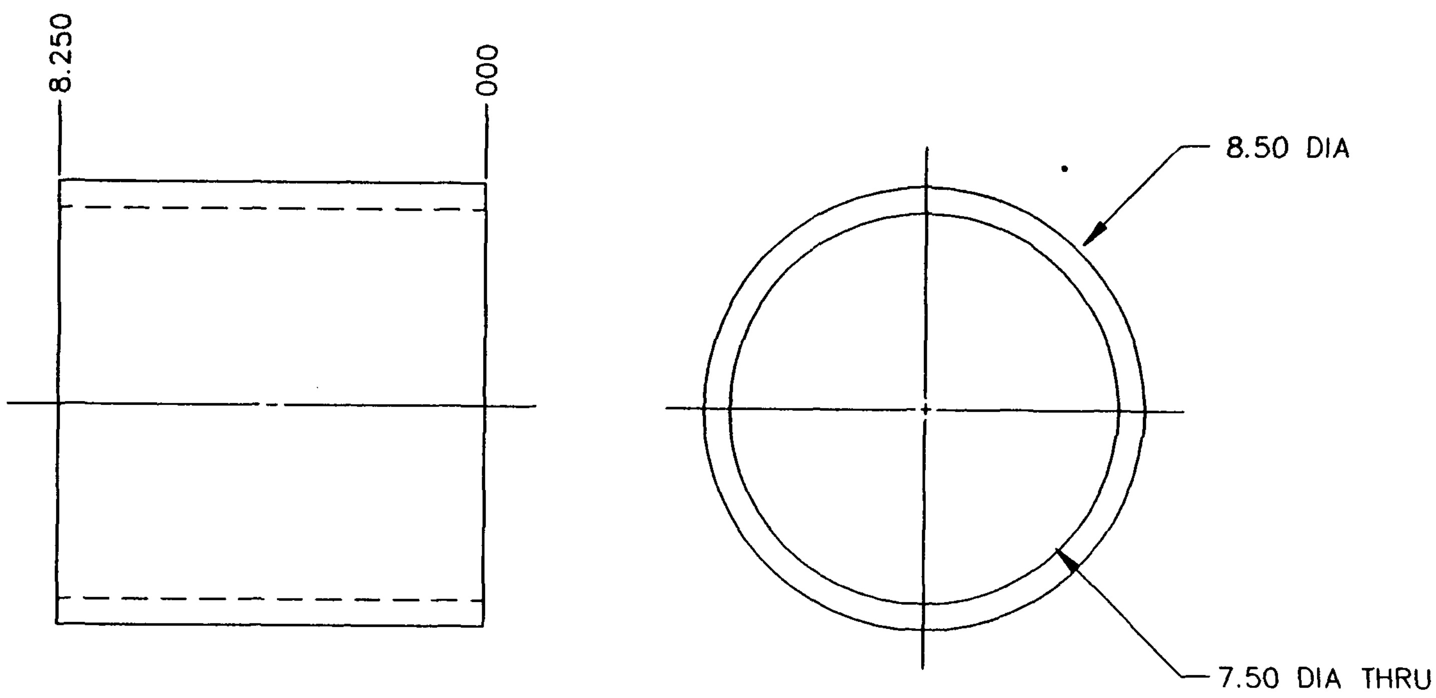

NOTES:

1. REMOVE ALL SHARP EDGES
2. MATL: PMMA

Plexiglass Wall
SCALE: 1=1

Figure 78. Trigatron electrode spacer and wall.

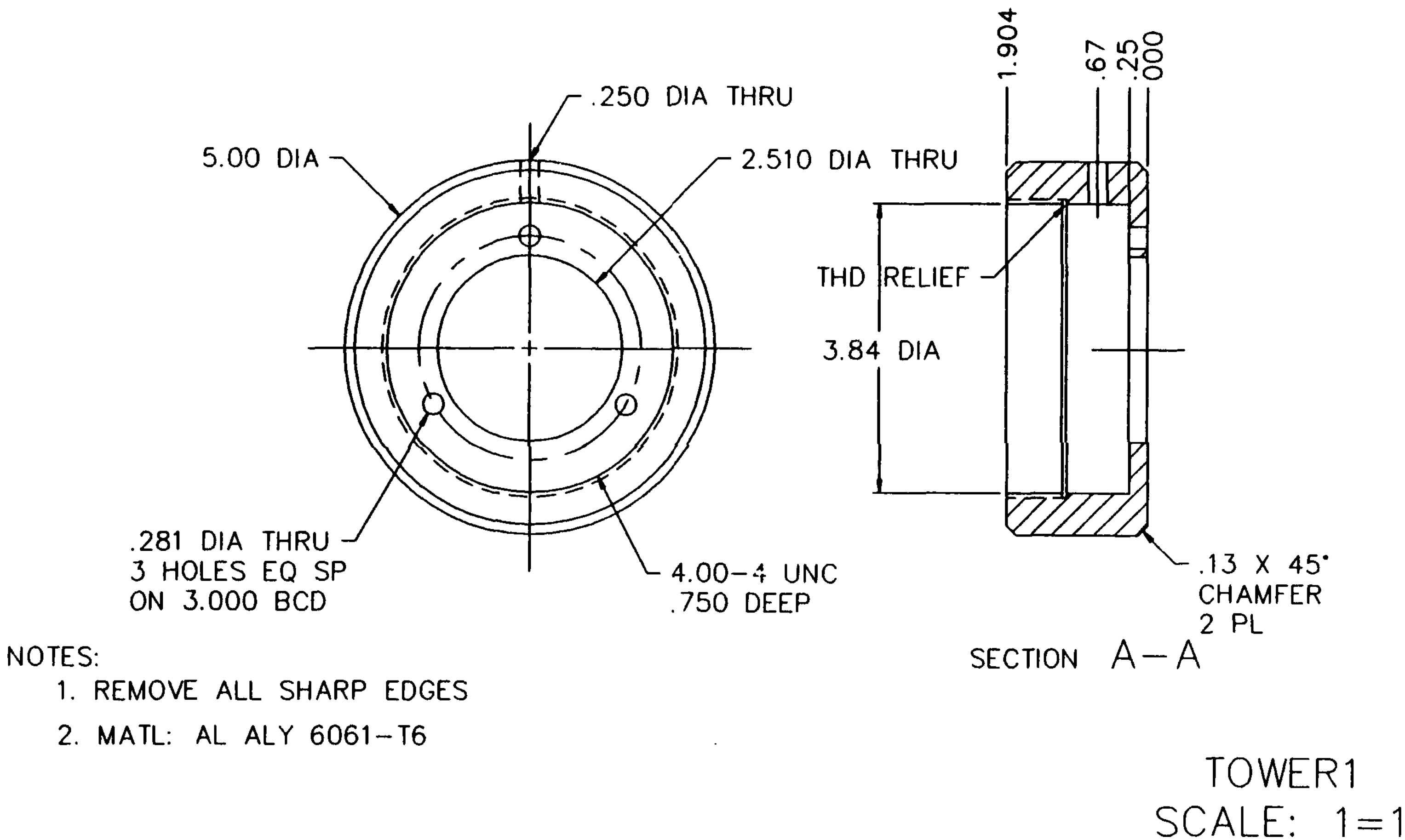

Figure 79. Electrode holder.

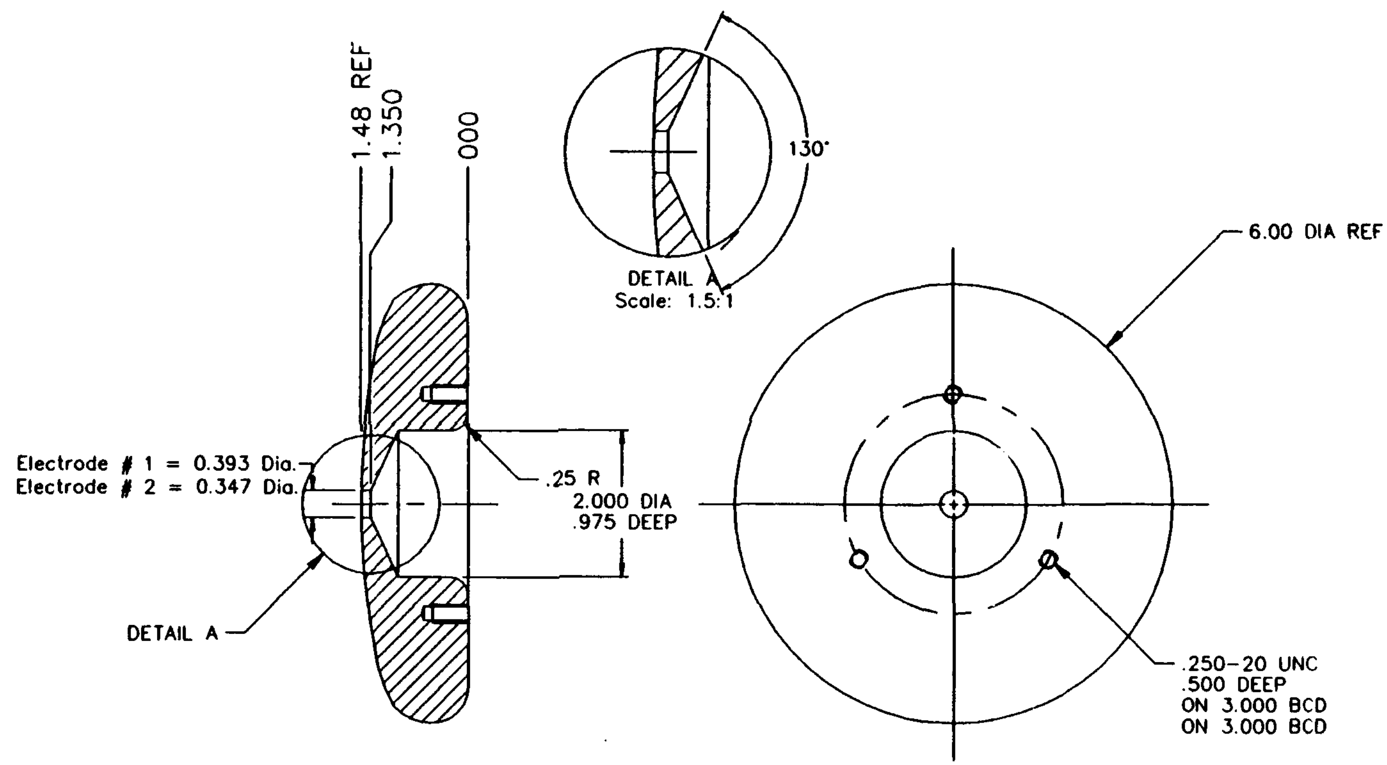

NOTES:

1. REMOVE ALL SHARP EDGES

Figure 80. Trigatron triggered electrode.

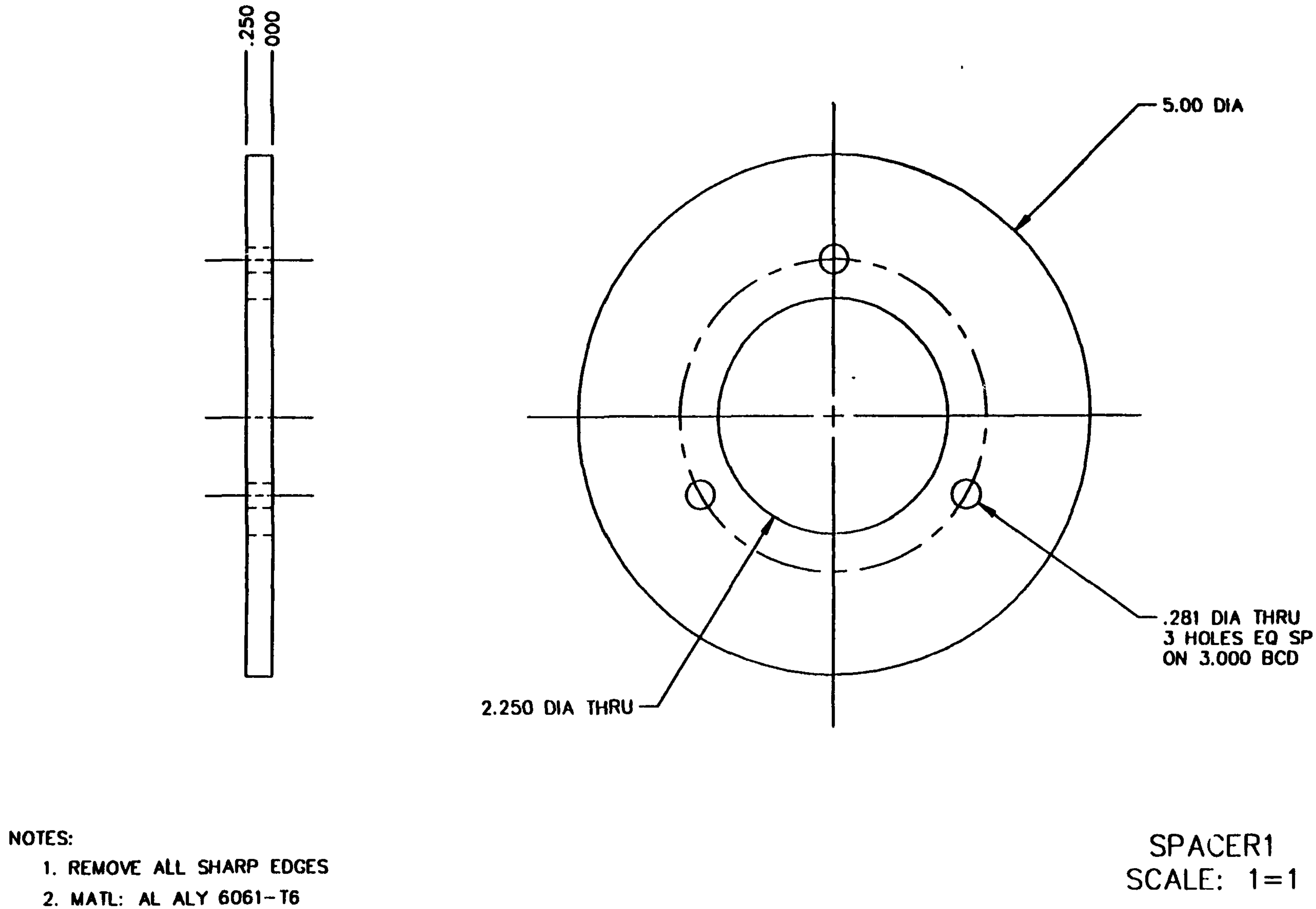

Figure 81. Electrode spacer (1 MV).

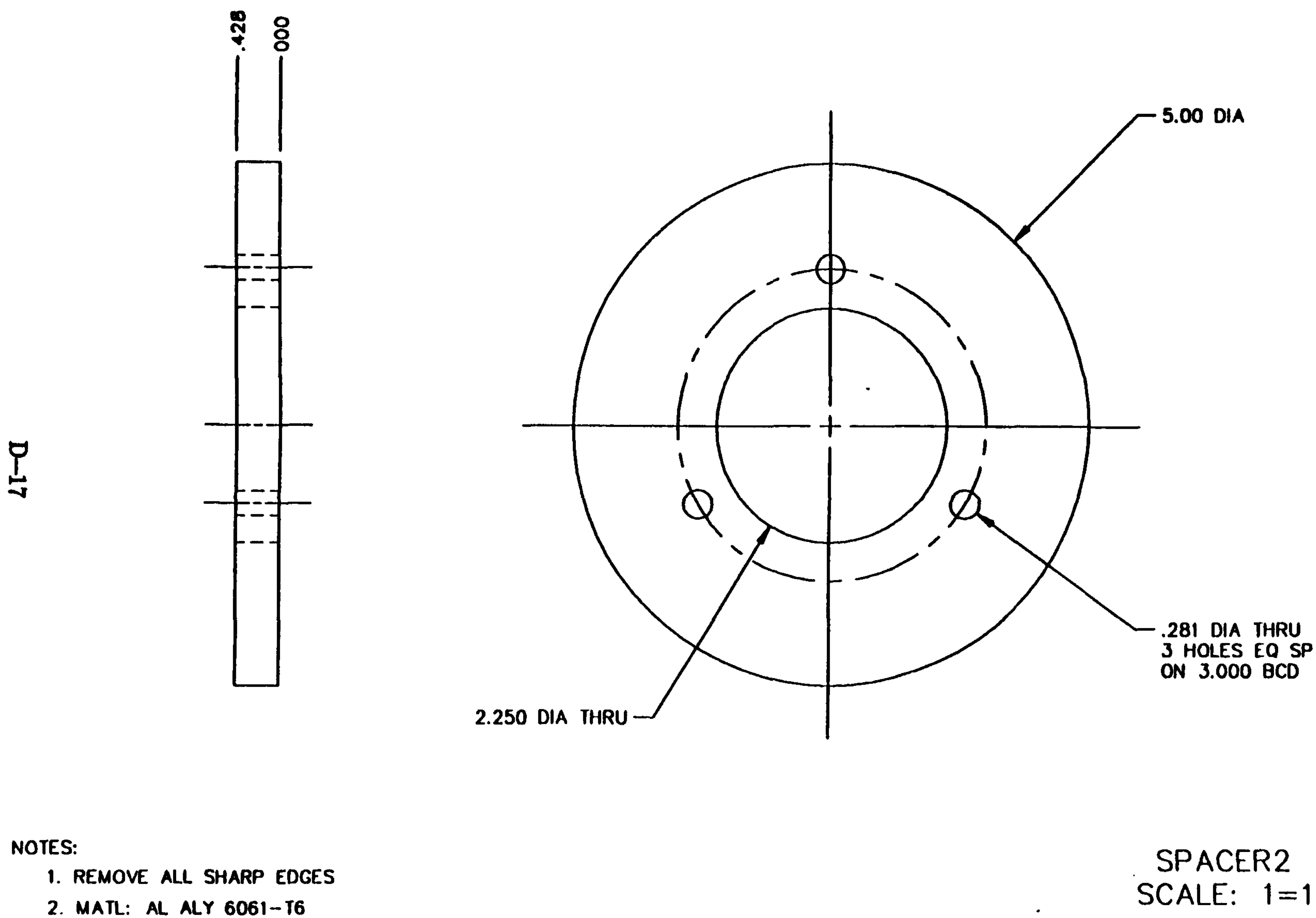

Figure 82. Electrode spacer (500 kV).

DISTRIBUTION LIST

DNA-TR-91-86

DEPARTMENT OF DEFENSE

ASSISTANT TO THE SECRETARY OF DEFENSE
ATTN: EXECUTIVE ASSISTANT

DEFENSE INTELLIGENCE AGENCY
ATTN: DIW-4

DEFENSE NUCLEAR AGENCY
ATTN: RAAE K SCHWARTZ
ATTN: RAEE
2 CYS ATTN: RAEV
2 CYS ATTN: TITL

DEFENSE TECHNICAL INFORMATION CENTER
2 CYS ATTN: DTIC/FDAB

FIELD COMMAND DEFENSE NUCLEAR AGENCY
ATTN: FCTT

DEPARTMENT OF THE ARMY

HARRY DIAMOND LABORATORIES
ATTN: SLCHD-NW-RS G KERRIS
ATTN: SLCHD-NW-TN
ATTN: SLCIS-IM-TL

U S ARMY NUCLEAR & CHEMICAL AGENCY
ATTN: MONA-NU DR D BASH

USA SURVIVABILITY MANAGMENT OFFICE
ATTN: SLCSM-SE J BRAND

DEPARTMENT OF THE NAVY

NAVAL RESEARCH LABORATORY
ATTN: CODE 4750 J SETHIAN
ATTN: CODE 4770 G COOPERSTEIN

NAVAL SURFACE WARFARE CENTER
ATTN: CODE H23 V KENYON
ATTN: CODE R41

NAVAL SURFACE WARFARE CENTER
ATTN: CODE H-21

DEPARTMENT OF ENERGY

LAWRENCE LIVERMORE NATIONAL LAB
ATTN: L-545 J NUCKOLLS
ATTN: M F BLAND L-153

LOS ALAMOS NATIONAL LABORATORY
ATTN: J BROWNELL

SANDIA NATIONAL LABORATORIES
ATTN: ORG 9300 J E POWELL
ATTN: TECH LIB 3141

OTHER GOVERNMENT

CENTRAL INTELLIGENCE AGENCY
ATTN: OSWR J PINA

DEPARTMENT OF DEFENSE CONTRACTORS

ADVANCED RESEARCH & APPLICATIONS CORP
ATTN: R ARMISTEAD

AEROSPACE CORP
ATTN: LIBRARY ACQUISITION

JAYCOR
ATTN: E WENAAS

KAMAN SCIENCES CORP
ATTN: D CALDWELL

KAMAN SCIENCES CORP
ATTN: DASIAC

KAMAN SCIENCES CORPORATION
ATTN: DASIAC

LOGICON R & D ASSOCIATES
ATTN: I VITKOVITSKY

PHYSICS INTERNATIONAL CO
ATTN: C STALLINGS

PULSE SCIENCES, INC
ATTN: I D SMITH
ATTN: P W SPENCE

S-CUBED
ATTN: J M WILKENFELD
ATTN: WAISMAN

SCIENCE APPLICATIONS INTL CORP
ATTN: W CHADSEY

TETRA CORP
2 CYS ATTN: J M ELIZONDO
2 CYS ATTN: W M MOENY

TEXAS TECH UNIVERSITY
ATTN: M KRISTIANSEN